



Fracture of skin-stiffener intersections in composite wind turbine blade structures
by Darrin John Haugen

A thesis submitted in partial fulfillment of the requirements for the degree of Master of Science . in
Mechanical Engineering
Montana State University
© Copyright by Darrin John Haugen (1998)

Abstract:

Most wind turbine blades have a stiffening spar running the length of the blade to add rigidity to the airfoil skins. This spar is usually an I-beam or C-channel. The interface between the spar flange and skin surface is often the site of fracture and delamination growth in composite wind turbine blades. Fracture initiates here due to high out-of-plane stresses and stress concentration areas, combined with the low transverse and out-of-plane strength of composite materials. Areas such as the stiffener flange tip may develop stress singularities due to the geometric mismatch between the flange and skin that cannot be analyzed with standard strength-based criteria. These factors make skin-stiffener detail regions a critical design component in wind turbine blade structures.

The goals for this study were to combine experimental testing with finite element analysis (FEA) to establish design guidelines and develop an accurate FEA method for predicting skin-stiffener fracture loads and locations.

Experimental fracture toughness tests showed that delamination growth resistance was higher for cracks propagating at a (+45/-45) degree ply interface than for cracks between two (0) degree plies. Increasing the skin bending stiffness and matrix material toughness produced large increases in pull-off loads. Increasing the flange thickness and the adhesive bond-line thickness caused the damage location to change from the web/flange bend region to the flange tip. This was due to the increasing geometric discontinuity at the flange tip, which created high interlaminar stresses.

A strength-based failure prediction with FEA results was adequate to predict damage onset in the stiffener specimens in regions without high stress gradients. However, a fracture mechanics approach was necessary to analyze the flange tip region. Good agreement with experimental damage onset loads was obtained by using the one-step virtual crack closure technique (VCCT-1) to calculate strain energy release rate values, which were used with the linear interaction criterion for crack growth to predict propagation loads. An initial crack length of less than 0.2 mm and a crack length to crack extension ratio (a/da) of greater than 20 provided good results for the modeling of damage onset at the flange tip.

FRACTURE OF SKIN-STIFFENER INTERSECTIONS
IN COMPOSITE WIND TURBINE BLADE STRUCTURES

by

Darrin John Haugen

A thesis submitted in partial fulfillment
of the requirements for the degree

of

Master of Science

in

Mechanical Engineering

MONTANA STATE UNIVERSITY-BOZEMAN
Bozeman, Montana

August 1998

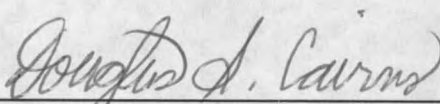
N378
H2919

APPROVAL

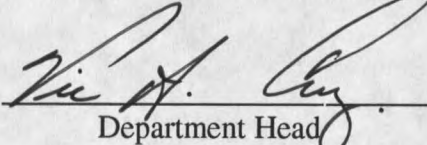
of a thesis submitted by

Darrin John Haugen

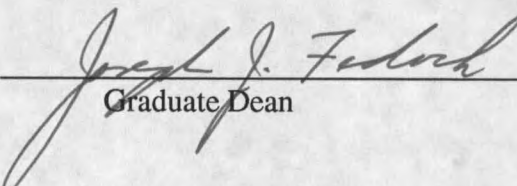
This thesis has been read by each member of the thesis committee and has been found to be satisfactory regarding content, English usage, format, citations, bibliographic style, and consistency, and is ready for submission to the College of Graduate Studies.

Dr. Douglas Cairns  7/7/98
Chairperson, Graduate Committee Date

Approved for the Department of Mechanical Engineering

Dr. Vic Cundy  7/7/98
Department Head Date

Approved for the College of Graduate Studies

Dr. Joseph Fedock  7/10/98
Graduate Dean Date

STATEMENT OF PERMISSION TO USE

In presenting this thesis in partial fulfillment of the requirements for a master's degree at Montana State University-Bozeman, I agree that the Library shall make it available to borrowers under rules of the Library.

If I have indicated my intention to copyright this thesis by including a copyright notice page, copying is allowable only for scholarly purposes, consistent with "fair use" as prescribed in the U.S. Copyright Law. Requests for permission for extended quotation from or reproduction of this thesis in whole or in parts may be granted only by the copyright holder.

Signature Dan Hump
Date 7/7/98

ACKNOWLEDGMENTS

I gratefully acknowledge the guidance of Dr. Douglas Cairns and Dr. John Mandell in this research effort. Their support throughout my graduate career has made this project possible. Thanks are directed to Dr. Jay Conant for serving as a graduate committee member. Daniel Samborsky deserves special recognition for all of the assistance with experimental testing, manufacturing, data analysis, and preparing figures and photographs for this report. Thanks to the other graduate students in the composite materials group for your smiles and friendships over the past few years. Finally, thanks to my family, and most of all, Melissa, my wife. Your never ending support and love have helped me to attain my goals and strive to always do my best.

This work was supported by the U.S. Department of Energy and the State of Montana through the Montana DOE EPSCoR Program (Contract # DEFC02-91ER75681) and Sandia National Laboratories (Subcontract ANO412).

TABLE OF CONTENTS

LIST OF TABLES	vii
LIST OF FIGURES	viii
ABSTRACT.....	xi
1. INTRODUCTION	1
2. BACKGROUND	4
Problems with Stiffener Detail Regions	4
Stiffener Design Considerations	5
Flange Taper Angle.....	5
Skin and Flange Bending Stiffness	7
Delamination Interface Ply Angles	9
Matrix Material	10
Through-thickness Reinforcement.....	11
Design for Manufacturing.....	13
Fracture Mechanics	14
Strain Energy Release Rate.....	15
Experimental Determination of Strain Energy Release Rate.....	16
Analytical Prediction of Strain Energy Release Rate	19
Mode Interaction and Failure Criteria.....	23
3. EXPERIMENTAL METHODS.....	27
Materials and Manufacturing.....	27
DCB and ENF Specimens.....	28
Substructure Testing	30
4. NUMERICAL METHODS	38
Model Generation	39
DCB Models	40
Substructure Models	44
5. EXPERIMENTAL RESULTS AND DISCUSSION	50
DCB Specimens	50
(+45/-45) Interface	50
(0/0) Interface.....	55
ENF Specimens.....	58
(+45/-45) Interface	59
(0/0) Interface.....	60
Thin-Flanged Stiffeners	60

Tensile Static Loading	60
Co-Cured vs. Secondarily Bonded.....	60
Matrix Materials.....	67
Compressive Static Loading	70
Thick-Flanged Stiffeners	73
Tensile Static Loading	73
6. NUMERICAL RESULTS AND DISCUSSION	77
DCB Modeling.....	78
$[(+45/-45)]_{10}$ DCB Models.....	79
$[(0)]_{10}$ DCB Models	83
Thin-Flanged Stiffeners	90
Co-Cured Specimens	90
Tensile Loading	90
Compressive Loading	97
Thick-Flanged Stiffeners	99
Thick Skin with (0/0) Interface.....	99
Thin Skin with (+45/-45) Interface	105
7. SUMMARY AND RECOMMENDATIONS.....	111
Experimental Summary	111
DCB and ENF Testing.....	111
Stiffener Testing.....	112
Stiffener Design Recommendations	112
Numerical Modeling Summary.....	113
Numerical Modeling Recommendations	114
Future Work.....	115
REFERENCES CITED.....	116
APPENDIX A	
Mixed-Mode Failure Calculation.....	120
APPENDIX B	
Test Results	123

LIST OF TABLES

Table	Page
1. Longitudinal and transverse properties for unidirectional polyester/E-glass composite.....	2
2. Ply orientations and laminate identification codes for substructure tests	31
3. T specimen substructure test matrix	32
4. Elastic Constants and Strengths for Unidirectional Material D155 at a $V_F = 36\%$	42
5. Static longitudinal, transverse, and simulated shear properties for D155 and DB120 unidirectional materials.....	43
6. DCB test results summary.....	52
7. ENF test results summary.....	59
8. Test results for bonded and co-cured thin-flanged stiffeners.	64
9. Thin-flanged stiffener pull-off tests with different matrix materials.....	68
10. Initial damage loads for thick-flanged stiffener tests.....	74
11. Failure prediction in the bend region for thin-flanged stiffener specimens.	94
12. Damage load predictions for thin-flanged stiffener specimens.....	98
13. Experimental vs. FEA results at average experimental damage onset load.....	99
14. Initial damage load predictions at flange tip using VCCT-1 method	101
15. Initial damage load predictions at flange tip using VCCT-2 method	103

LIST OF FIGURES

Figure	Page
1. Wind turbine blade cross section	3
2. Structural discontinuities producing high stress gradients.....	6
3. Skin-stiffener global-local structures and flange tip region.....	6
4. Delamination onset stress vs. flange lay-up and flange/skin thickness ratio	8
5. Onset of delamination for skin and flange under shear	9
6. The three modes of crack loading	14
7. DCB geometry and loading	16
8. Typical loading-unloading curve for DCB test.....	17
9. ENF geometry and loading	18
10. VCCT-1 schematic with 8-node quadrilateral elements.....	20
11. VCCT-2 schematic for Mode I closure.....	21
12. Generalized graphical representation of the linear and bilinear failure criteria.....	24
13. Design flowchart for global-local analysis with FEA.....	26
14. Typical load-displacement curve for ENF test.....	30
15. Geometry and loading for thin-flanged stiffener tests	33
16. Geometry and loading for thick-flanged stiffener tests	34
17. Simply supported test fixture for tensile and compressive stiffener tests.....	35
18. Typical load-displacement curve for thin-flanged stiffener pull-off test.....	36

19. Typical load-displacement curve for compressive thin-flanged stiffener test.....	37
20. Deformed finite element mesh of DCB specimen with a delamination	41
21. Finite element mesh for thin-flanged stiffener tests	45
22. Finite element mesh for thick-flanged stiffener tests.....	46
23. R-curve for (+45/-45) and (0/0) specimens calculated with the MBT method.....	51
24. R-curve for (+45/-45) specimens calculated with the Area and MBT methods.....	52
25. Fracture surface for [(+45/-45)] ₁₀ DCB specimen	53
26. R-curve for (0/0) DCB specimens, calculated with the Area and MBT methods	56
27. Mode I and II fracture surfaces for [(0)] ₁₀ DCB and ENF specimens.....	57
28. Initial damage at web/flange fillet area in thin-flanged stiffener specimens	61
29. Formation of delaminations at bend region in thin-flanged stiffeners.....	63
30. Cross-section of a thick bond-line on a commercial wind turbine blade.....	65
31. Pull-off strength vs. bond-line thickness for thin-flanged specimens.....	66
32. Typical load-displacement curve for polyester/PET stiffener specimen	69
33. Photograph of polyester/PET stiffener with delaminations	70
34. Typical load-displacement curve for polyurethane stiffener specimen	71
35. Photograph of thin-flanged stiffener after failure by compressive loading	72
36. Photograph of flange tip delamination for thick-flanged stiffener specimens.....	75
37. FEA G_{Ic} predictions vs. experimental data for [(+45/-45)] ₁₀ DCB specimen.....	81
38. FEA G_{Ic} predictions vs. experimental data for [(0)] ₁₀ DCB specimen.....	84
39. Mesh refinement at crack tip for DCB 503 b.....	85

40. Mesh sensitivity for VCCT-1 and VCCT-2 corner node methods	86
41. Percent change in FEA G_I prediction vs. ratio (a/da)	87
42. Mesh sensitivity analysis for VCCT-1 and VCCT-2 mid-side node methods at low (a/da) ratios	88
43. Percent reduction in FEA G_I predictions vs. ratio (a/Ew).....	89
44. Radial strain plot in the bend region for thin-flanged stiffener model	92
45. Tangential strain plot in the bend region for thin-flanged stiffener model.....	93
46. G_I and G_{II} at flange tip vs. ratio (a/da).....	101
47. Experimental and predicted load-displacement curves to damage onset for T 5200 specimens	102
48. Predicted propagation load vs. delamination length for T 5200 specimens	104
49. Experimental and predicted load-displacement curves to damage onset for T 5000 specimens	106
50. Predicted propagation load vs. delamination length for T 5000 specimens	108
51. Flange tip peel stress curve fit for use in Whitney-Nuismer failure criterion	109

ABSTRACT

Most wind turbine blades have a stiffening spar running the length of the blade to add rigidity to the airfoil skins. This spar is usually an I-beam or C-channel. The interface between the spar flange and skin surface is often the site of fracture and delamination growth in composite wind turbine blades. Fracture initiates here due to high out-of-plane stresses and stress concentration areas, combined with the low transverse and out-of-plane strength of composite materials. Areas such as the stiffener flange tip may develop stress singularities due to the geometric mismatch between the flange and skin that cannot be analyzed with standard strength-based criteria. These factors make skin-stiffener detail regions a critical design component in wind turbine blade structures.

The goals for this study were to combine experimental testing with finite element analysis (FEA) to establish design guidelines and develop an accurate FEA method for predicting skin-stiffener fracture loads and locations.

Experimental fracture toughness tests showed that delamination growth resistance was higher for cracks propagating at a (+45/-45) degree ply interface than for cracks between two (0) degree plies. Increasing the skin bending stiffness and matrix material toughness produced large increases in pull-off loads. Increasing the flange thickness and the adhesive bond-line thickness caused the damage location to change from the web/flange bend region to the flange tip. This was due to the increasing geometric discontinuity at the flange tip, which created high interlaminar stresses.

A strength-based failure prediction with FEA results was adequate to predict damage onset in the stiffener specimens in regions without high stress gradients. However, a fracture mechanics approach was necessary to analyze the flange tip region. Good agreement with experimental damage onset loads was obtained by using the one-step virtual crack closure technique (VCCT-1) to calculate strain energy release rate values, which were used with the linear interaction criterion for crack growth to predict propagation loads. An initial crack length of less than 0.2 mm and a crack length to crack extension ratio (a/da) of greater than 20 provided good results for the modeling of damage onset at the flange tip.

CHAPTER 1

INTRODUCTION

Improvements in wind turbine blade structures and design methods are essential for continued advancement in the utilization of wind power as a viable energy resource. Blades must sustain complicated fatigue loading, extreme event static loading, and be damage tolerant to meet their projected lifetime goals. In addition, there is a trade off among increasing blade strength and lifetime, while decreasing blade efficiency due to added weight.

To meet these performance requirements, most wind turbine blades now use composite materials. Composite materials consist of a reinforcing phase, such as glass or carbon fibers, and a binder phase, usually a thermoset or thermoplastic polymer. Composites are the preferred material due to their combination of high in-plane strength in the fiber direction, good fatigue resistance, and high stiffness to weight ratio. However, they are quite weak in the transverse and out-of-plane (through-thickness) directions. Longitudinal and transverse properties for a unidirectional E-glass fabric/polyester composite are listed in Table 1. Note the much lower values for strengths and moduli in the transverse (UTS_T , E_T) and through thickness (UTS_Z , E_Z) directions compared to the longitudinal fiber direction (UTS_L , E_L). As a result, transverse

Table 1. Longitudinal and transverse properties for unidirectional polyester/E-glass composite (D155 fabric at a V_F of 36%) [1].

Property	Test Values	Average	Std. Dev.
E_L (GPa)	28.1, 27.0, 29.8	28.3	1.4
E_T (GPa)	8.00, 7.31, 7.93	7.75	0.38
E_Z (GPa)	7.10, 7.65, 7.38	7.38	0.28
UTS_L (MPa)	891, 814, 883, 838	856.0	37.0
UTS_T (MPa)	26.6, 36.0, 30.4, 32.9, 29.0	31.0	3.6
UTS_Z (MPa)	21.7, 18.7, 20.4, 18.1	19.7	1.6

cracking and peeling apart of the ply layers are common failure modes.

Most wind turbine blades use a span-wise stiffening spar (Fig. 1) that is bonded to the inner skin surfaces to stiffen the blade, prevent skin bucking, resist transverse shear loading, and provide the proper natural frequency of vibration for the blade. It has been observed that failure is often the result of skin-stiffener separation in composite skin-stiffened structures [2, 3]. The geometric changes in these areas lead to high stress gradients, complex stress variations, and significant interlaminar stresses, which cause delamination failure.

Kedward et al. [4] reported that many composite structure failures have been the result of "detail design oversights", especially at curved regions, and that designers have

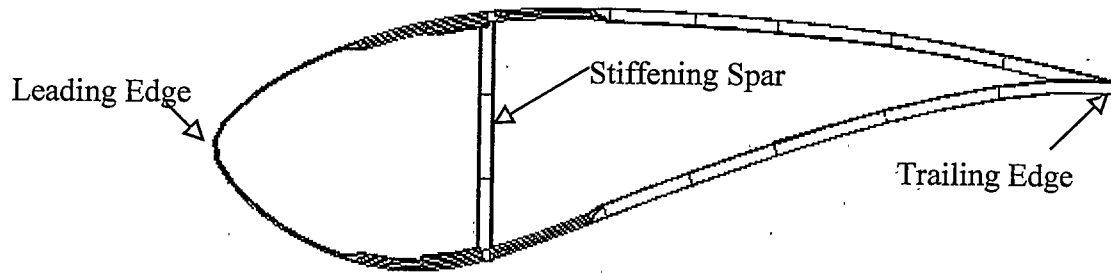


Figure 1. Wind turbine blade cross section.

a “general lack of appreciation” for the low through-thickness strengths of composites. According to Martin [3], global analysis approaches “fail to identify those areas, such as structural or material discontinuities, where failure will initiate from interlaminar stresses.” In addition, design details are subject to processing variability and are difficult to inspect once inserted in a blade. Consequently, these detail regions have limited the performance and lifetimes of blades.

In order to investigate the mechanisms of fracture in these detail regions, an approach combining experimental testing of blade detail regions with finite element analysis (FEA) was used. The goals were to establish design guidelines for composite skin-stiffener detail regions and to formulate an accurate predictive capability and design methodology with FEA, especially at geometric discontinuities such as the flange tip. Once better predictive ability is established it should reduce the dependence on expensive structural testing [3], helping the design engineer to optimize detail region performance.

CHAPTER 2

BACKGROUND

Problems with Stiffener Detail Regions

Stiffened composite skins are a widely used engineering structure. Besides the current application in wind turbine blades, skin-stiffener structures are utilized in nearly all aircraft fuselage designs. A primary failure mode for these detail regions is delamination. This is due to a number of factors relating to material properties, design methodology, and load transfer paths.

Skin-stiffener intersections are inherently difficult to design due to the combination of multiple loading conditions and stress concentration areas. Some of these stress concentration areas, such as the flange tip, produce interlaminar stresses that act in the weakest plane of the composite material. It has been found that a stress singularity can exist at the flange terminus [5, 6, 7] implying that a stress component grows unbounded in this region. Analysis of these stress zone singularities can be difficult, requiring techniques that are not common practice for most designers. However, they are not impractical and have been implemented in the study of composite structures [3, 7-13] by previous investigators. A standard design method is to use a strength-based approach for calculating initial damage in areas where no stress singularity is present. This is

followed by a fracture mechanics analysis to predict delamination growth. If a singular stress field is present special design approaches are required from the outset. These techniques are discussed in detail in Chapter 4.

Stiffener Design Considerations

Some of the major problems and design concerns relating to composite stiffener designs have been addressed in the literature and are summarized in the remainder of this section. The topics of interest are as follows: flange tip taper angle, skin/flange bending stiffness and bending stiffness ratio, delamination interface ply orientations and bonding, matrix material selection, through-thickness reinforcements, manufacturing issues, and bend radii in curved composite parts.

Flange Taper Angle

Many composite structures contain geometric discontinuities that produce through-thickness (peeling) stresses even when the loading is entirely in-plane. Some common features that display this behavior are shown in Figure 2. In stiffener detail regions, this singular stress zone occurs at the flange tip (Fig. 3) and has been noted by Hyer and Cohen [5, 6, 7] and Kassapoglou [11]. Tapering the flange tip (Fig. 3) has been shown to dramatically increase the pull-off strength of composite stiffeners. This happens because the interlaminar peel and shear stresses and stress gradients are reduced at the flange tip area by minimizing the geometric and stiffness discontinuity,

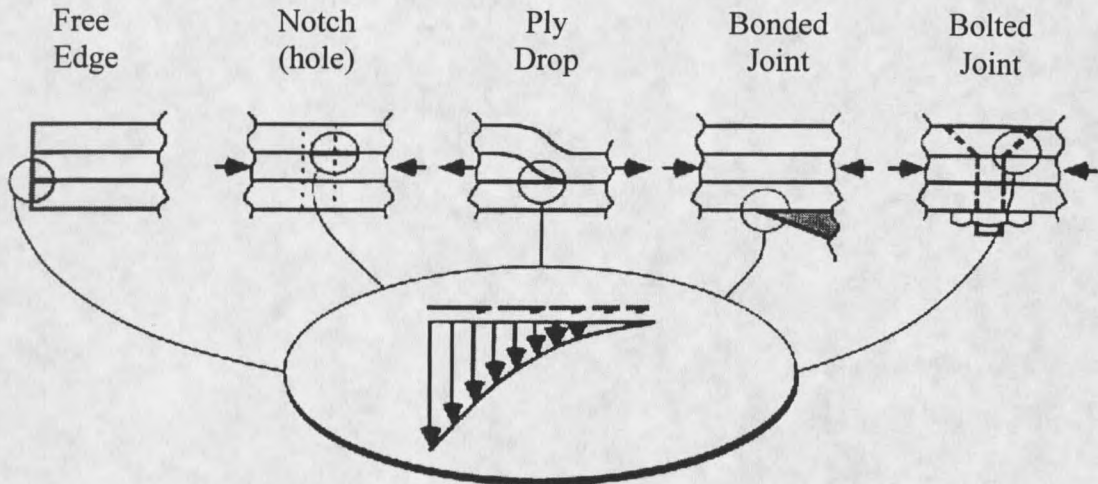


Figure 2. Structural discontinuities producing high stress gradients [14].

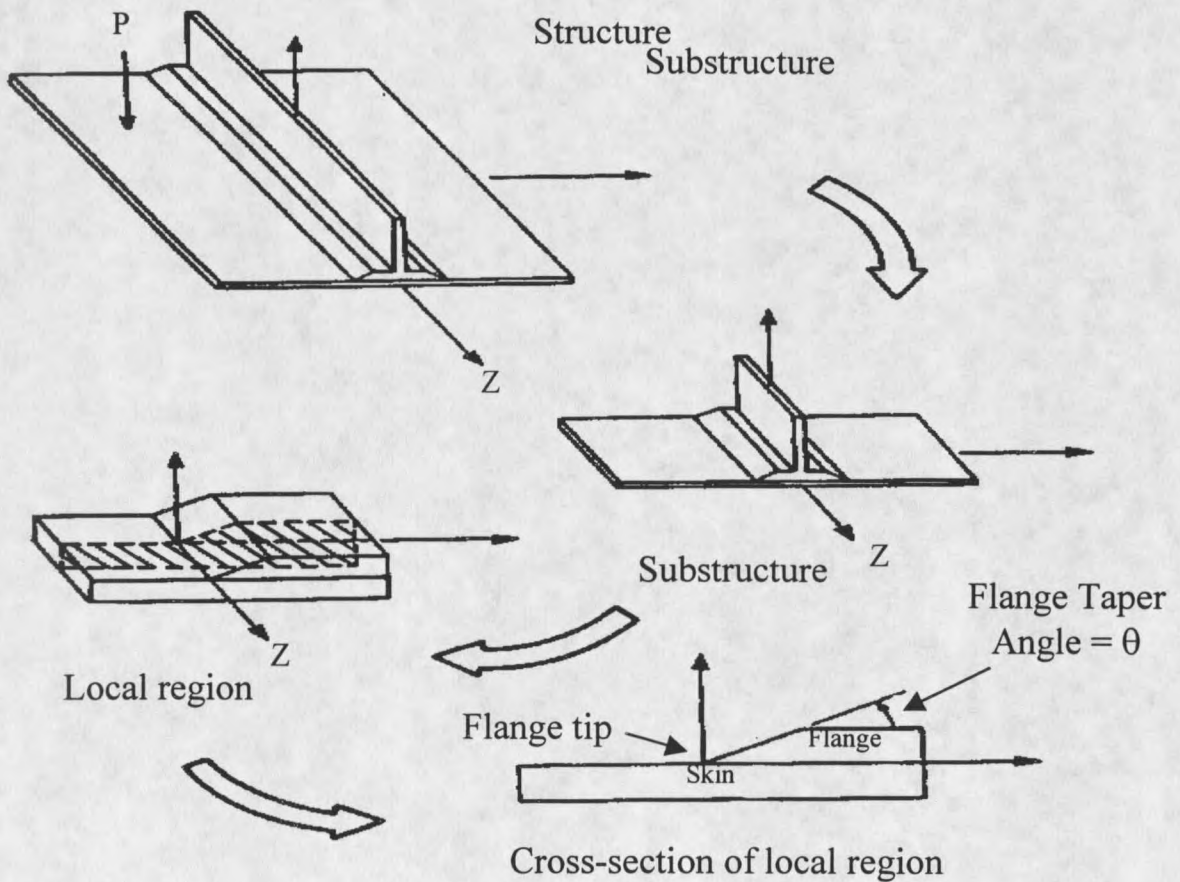


Figure 3. Skin-stiffener global-local structures and flange tip region [7].

effectively reducing the stresses [5, 6]. Minguet et al. [15] noted this increased performance of samples with tapered flange tips in stiffener pull-off tests. A 32% higher initial damage onset load for a 20° taper, compared with a 45° taper was observed. Minguet and O'Brien [9] noted a 35% increase in damage initiation load for samples with a 20° taper angle versus a 90° flange tip in 3-point bending tests. Furthermore, a detailed finite element solution at the flange tip confirmed that the tapered configuration reduced the peel stress by 76%, thus explaining the load increase at fracture onset. Tapering the flange tip clearly mitigates one of the main causes of delamination onset in composite stiffeners.

Skin and Flange Bending Stiffness

Another design aspect that has received attention is the bending stiffness in the skin and flange and the relative stiffness ratio between these components. Much of this work has been in response to the "pressure pillowing" effect seen in aircraft fuselage structures. Pressure pillowing occurs in fuselage structure during the cabin pressurization procedure when the internal cabin pressure makes the skin bulge outward in between the rows of stiffeners attached to the skin. This condition leads to bending in the skin transverse to the stiffener longitudinal axis. As a result, peeling and transverse shear stresses develop at the interface between the skin and stiffener. This same loading may be encountered in wind turbine blades if there is localized skin buckling producing chord-wise bending near the stiffener. Minguet et al. [15] reported a significant increase in strength with an increase in skin flexural stiffness in skin/stringer pull-off tests. Their data showed a 95% increase in maximum load with a 30% increase in skin thickness and

initial damage moment values increased approximately 66% with the 30% increase in skin thickness. Kassapoglou [11] utilized elasticity solutions to evaluate the parameter of flange to skin bending stiffness (thickness) ratio with all 0^0 unidirectional material in both the skin and flange. For the case of in-plane skin tensile stress applied perpendicular to the stiffer longitudinal axis, thin flanges performed better. As flange/skin thickness ratio (t_f/t_s) increased the damage onset load went through a minimum, and then began to increase (Fig. 4). According to this data, t_f/t_s ratios of 0.5 to 1.5 should be avoided since they had the lowest predicted failure onset loads for flange tip failure. For skin in-plane

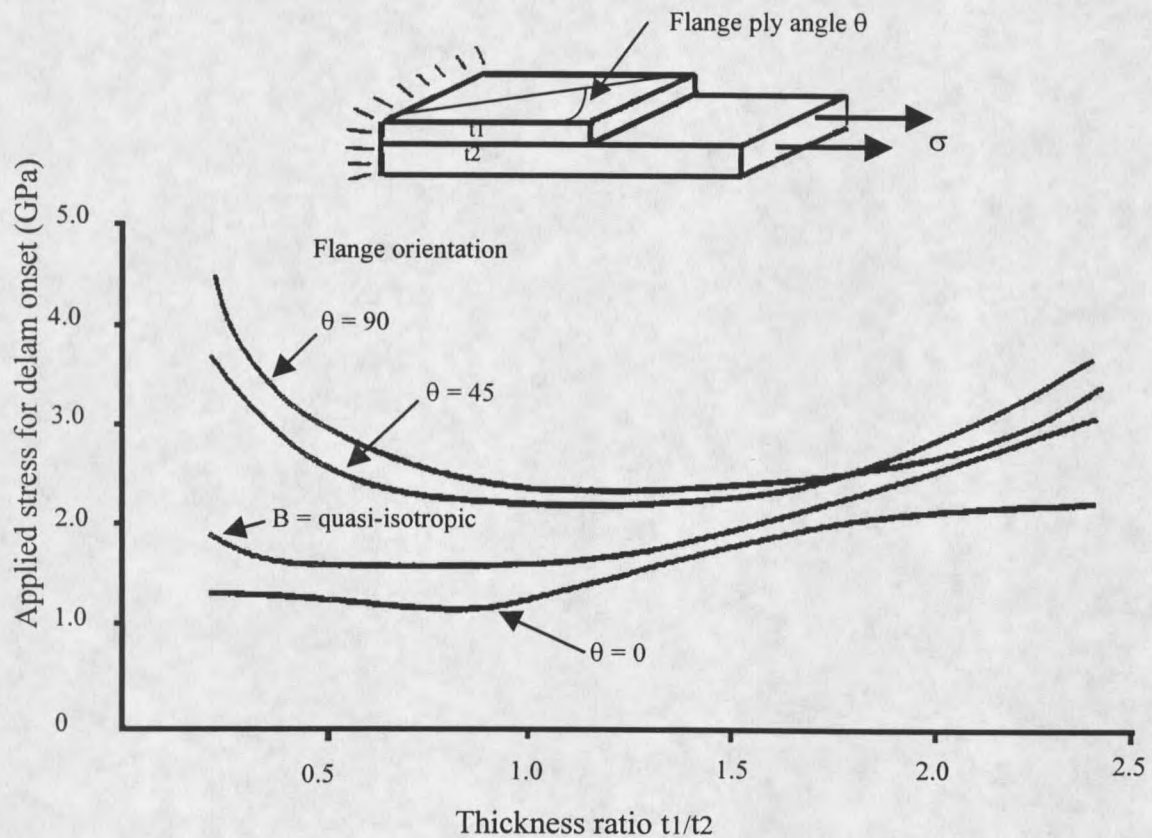


Figure 4. Delamination onset stress vs. flange lay-up and flange/skin thickness ratio [11].

shear loading the highest delamination onset loads occurred below a ratio of 0.5, with lower ratios performing better (Fig. 5).

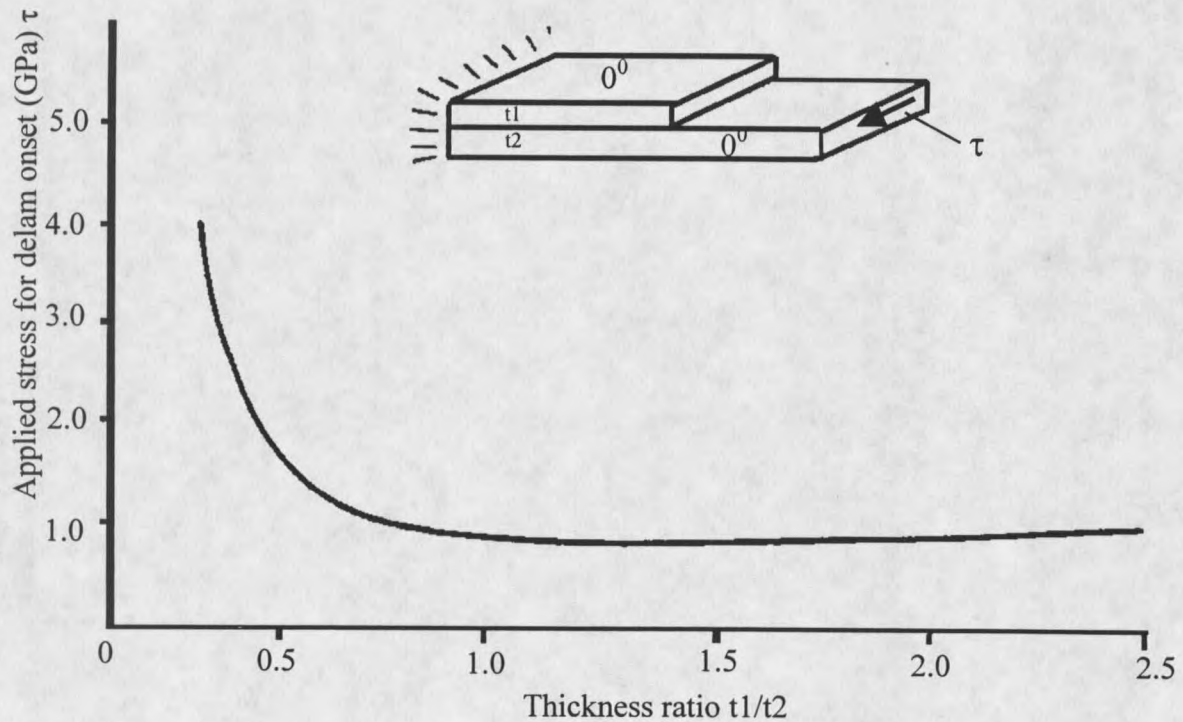


Figure 5. Onset of delamination for skin and flange under shear [11].

Delamination Interface Ply Angles

The relative angle of the composite plies at the delamination interface has also received some attention. Minguet and O'Brien investigated failure onset for the case of skin bending simulating pressure pillowing effects [8]. Results indicate that 90° plies at the bondline are the worst case, due to the propensity to form transverse cracks that initiate delaminations. Kassapoglou [11] used elasticity solutions to predict behavior of a flange/skin strip (Fig. 4) loaded with a tensile stress in the skin applied perpendicular to

the stiffener longitudinal axis. For the case of a unidirectional skin aligned with the tension loading and $t_f/t_s < 1.0$, higher in-plane flange stiffness (in the load direction) produced lower delamination onset loads (Fig. 4). Kassapoglou explained this behavior by noting that increasing the flange stiffness (or thickness) increased the load carried by the flange. This creates moments between the skin and flange that must be balanced by a moment at the flange tip. That moment is generated by development of high interlaminar stresses in that area.

Variations in delamination resistance with varying ply angle and fabric architecture have also been noted for stitched and woven fabrics typical of those used by the wind turbine industry. Scott [16] found that in double cantilever beam (DCB) tests for a polyester/E-glass fabric system, G_{Ic} increased from 490 J/m² for a [(0)]₁₀ sample to 780 J/m² for a crack at a (0/+45) interface. He also found increases in G_{IIc} with ply interface lay-up. For five-harness satin orthogonal woven carbon/epoxy DCB samples with 12K tow bundles, Alif et al. [17] found that G_{Ic} increased when compared with a unidirectional sample. This was attributed to the crack path following the weave topology since no fiber bridging was observed in the woven fabric samples. As a result, this woven architecture requires more energy input to grow a crack than for self-similar planar crack growth observed at unidirectional interfaces. Based upon the previous references, it appears that designers can build delamination resistance into stiffener intersections through proper lay-up selection for a particular loading case.

Matrix Material

It is widely known that delamination is highly dependent on matrix material

properties [18, 19]. When composite plies are peeled apart, the behavior is influenced by the fracture toughness of the matrix. Bradley [19] reported that composite G_{Ic} was actually greater than neat resin G_{Ic} for resin toughness values below 500 J/m^2 . As resin toughness was increased, composite toughness increased. However, once resin toughness was at or above 2000 J/m^2 he found very little increase in overall composite toughness. This was attributed to the resin fracture process zone size being constrained by the adjoining fiber layers, with the zone size being on the order of the inter-ply spacing. Minguet et al. [15] observed that delaminations in bonded skin-stiffener pull-off tests never propagated within the adhesive layer itself, but grew within the top-most skin ply. In this case, the adhesive was tougher than the base resin system and therefore, had a higher resistance to crack growth. The delamination preferentially found the easiest path for advancement. If the resin formulation were toughened, this weak link could be reduced or eliminated from stiffener designs.

Through-thickness Reinforcement

Another method used in composite manufacturing to prevent delamination growth is through-thickness reinforcements. These are usually in the form of stitching or 3-D fiber weaves. This is done to strengthen the composite laminate in its out-of-plane direction, which can have a strength value of as little as 3% of its in-plane tensile strength [4]. Stitching and riveting have proven effective at improving delamination resistance, but when used at greater areal percentages, reduce in-plane tensile strength due to net-section loss [20, 21]. Mignery et al. [21] studied stitching as a means to deal with free edge delamination problems in tensile coupons. They discovered that one row of

stitching at each free edge had mixed effects on in-plane tensile strength, but effectively arrested delamination growth as the crack approached the stitch line. In addition, they performed FEA to investigate the strain energy release rate (SERR) and interlaminar normal stress distribution. The interlaminar normal stress was relatively unchanged by adding stitching, however, as the crack approached the stitch line, the SERR decreased, explaining the delamination arrest. This is due to the stitching restraining through-thickness displacement at the crack tip, which is referred to as fiber bridging.

A commercially available through-thickness reinforcement called Z-fiber™ has shown promise at increasing fracture toughness in composites. Z-fiber™ consists of short sections of either carbon fiber or 0.5 mm diameter titanium pins contained in a foam sheet in a “bed of nails” configuration. The foam is crushed on top of a fabric preform, pushing the pins into the fabric through the thickness. Typical reinforcing percentages are from 1 to 5% by area. Freitas and Fusco [20] report that Mode I fracture toughness for composites may increase by up to 50 times when compared with an unreinforced sample. Small decreases in ultimate in-plane tensile strain values were observed for AS4/3501-6 woven carbon fabric samples. When 5% areal density 0.5 mm titanium Z-fiber™ was used to reinforce skin-stringer pull-off sample, maximum pull-off loads were 2.5 times higher than the co-cured baseline sample. Improvements to Mode II shear delamination resistance are still under investigation. The main drawback to this technology appears to be cost. It is marketed toward the aerospace industry, and may not be feasible for low-cost wind turbine applications, or other large structures.

Design for Manufacturing

In order to meet the low-cost manufacturing goals for wind turbine blades, a number of manufacturing methods have been investigated. A primary method under consideration at MSU-Bozeman is resin transfer molding (RTM). In RTM resin is pumped through a closed mold cavity filled with dry fabric preform and allowed to cure.

A common design issue with RTM'd stiffeners has been web/flange transition fillet radius [4, 22]. Holmberg and Berglund found that the inner radius of RTM U-beams (C-channels) was an area of high fiber volume, reduced local permeability during resin flow, increased voids, and highly variable strength [22]. This was due to the fabric pulling tight around the fillet radius in the mold cavity. They also reported that literature values for recommended radii were between 3-12 mm for the RTM process. From U-beam strength testing they observed better performance for larger fillet radius beams. Beams with a 5.0 mm radius displayed average initial fracture loads (per unit width) in the bend region of 13.1 N/mm and 20.3 N/mm for vacuum bag and press forming methods, respectively. Beams with a 0.8 mm radius had an average initial damage load of approximately 10.3 N/mm for both manufacturing methods. The strength differences were due to a higher radial tensile stress in the bend of the 0.8 mm radius beams compared with the 5.0 mm radius beams at equal loading. Based upon these results, it appears that increasing the web fillet radius lowers the stress concentration in this area. This should increase the damage onset load at this detail region for stiffener geometries that are prone to delamination in the web-flange fillet radius area. However, there is a trade-off between lower stress concentrations through a larger fillet radius and added

material and weight in this region.

Fracture Mechanics

The field of fracture mechanics was developed to deal with the issues that are specific to materials containing cracks. Once a crack has formed in a material, standard stress-based analysis can no longer be accurately used to predict material yielding and crack advancement. Linear elastic fracture mechanics predicts that the elastic stress field perpendicular to the crack plane becomes unbounded at the crack front [23]. This is due to the existence of a $1/\sqrt{r}$ stress singularity at the crack tip [23], where r is the radial distance from of the crack tip.

Cracks may be loaded in the three distinct modes shown in Figure 6.

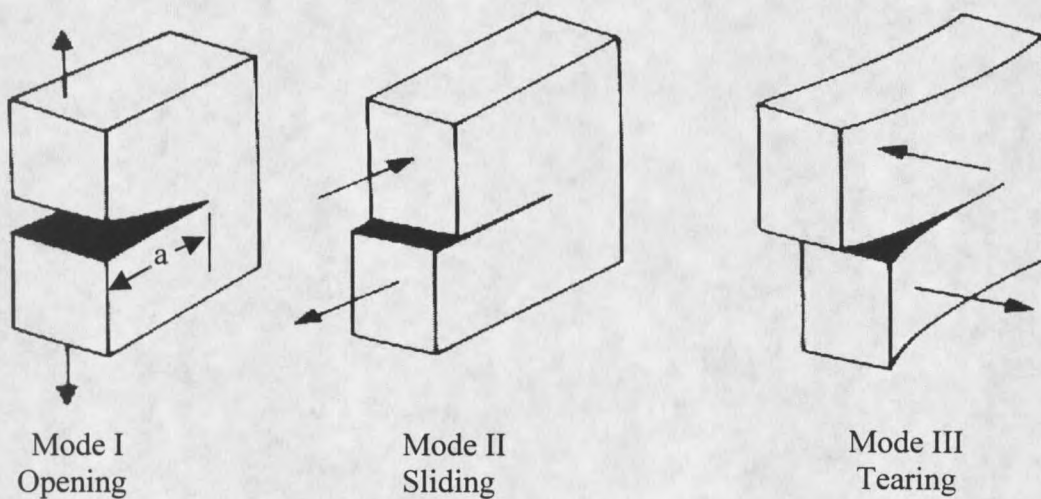


Figure 6. The three modes of crack loading [23].

Mode I is a pure opening mode, caused by stresses acting normal to the crack plane.

Mode II is an in-plane shear mode, and Mode III is an out-of-plane shearing mode.

Strain Energy Release Rate

One of the most common methods of analyzing and predicting crack behavior is the concept of strain energy release rate (SERR or G). The basis for the SERR lies in the Griffith criterion, which states, “crack propagation will occur if the energy released upon crack growth is sufficient to provide all the energy that is required for crack growth” [23].

The condition for crack growth is as follows:

$$dU/da = dW/da \quad (1)$$

where U = elastic strain energy

W = energy required for crack growth

a = crack length

G is also called the crack driving force and equals dU/da . The crack growth resistance is referred to as R and equals dW/da , which is the energy consumed in crack propagation per unit area of crack extension. The condition for growth in Equation (1) can also be read as $G = R$ at crack extension. At or above some critical value of G , the crack will propagate. This critical value must be experimentally determined for different material systems for each of the three crack extension modes. The critical value usually differs for each mode and is denoted with subscripts as G_{Ic} , G_{IIc} , G_{IIIc} , respectively. In practical terms, materials that are “tougher” have a higher value of G_c , requiring more energy to grow a crack in that material. A detailed discussion of fracture mechanics principles is

presented by Broek in Reference [23].

Experimental Determination of Strain Energy Release Rate

To obtain critical values for G in static loading conditions, a variety of tests are used for the various modes of crack extension. For Mode I fracture, the standard test specimen is the double cantilever beam (DCB) as described in ASTM standard D 5528 [24] and shown in Figure 7. A composite DCB sample is made by placing a thin film

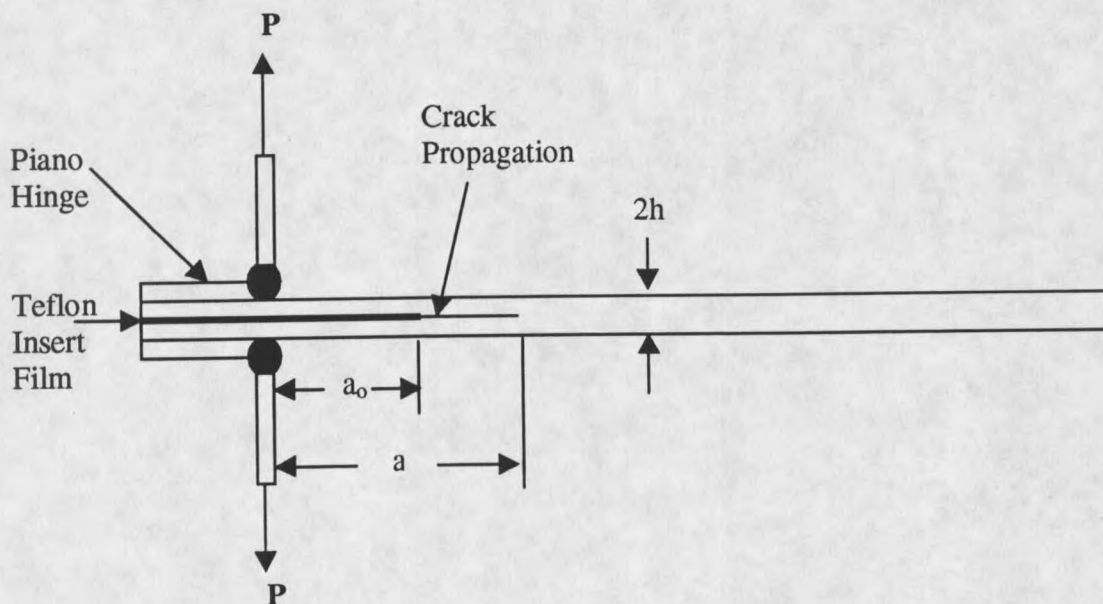


Figure 7. DCB geometry and loading.

of “release paper”, usually Teflon film, at the mid-plane of a laminate. This insert film serves as a delamination initiation site for the crack. The critical strain energy release rate to grow a crack in the material can be obtained by the use of the output load vs. displacement curve (Fig. 8) and the modified beam theory (MBT) method (Eq. 2).

$$G_{Ic} = 3P\delta / 2ba \quad (2)$$

Where: P = critical load at crack propagation

δ = displacement between DCB cantilever arms
at critical load

b = sample width

a = crack length

Another method, called the area method [18], needs a loading-unloading path plot (Fig. 8) for each G_{Ic} calculation. By calculating the area enclosed by the curve (strain energy released during the test) and dividing by the crack extension area, G_{Ic} may be calculated. This is shown as Equation (3). A drawback with the area method is that it

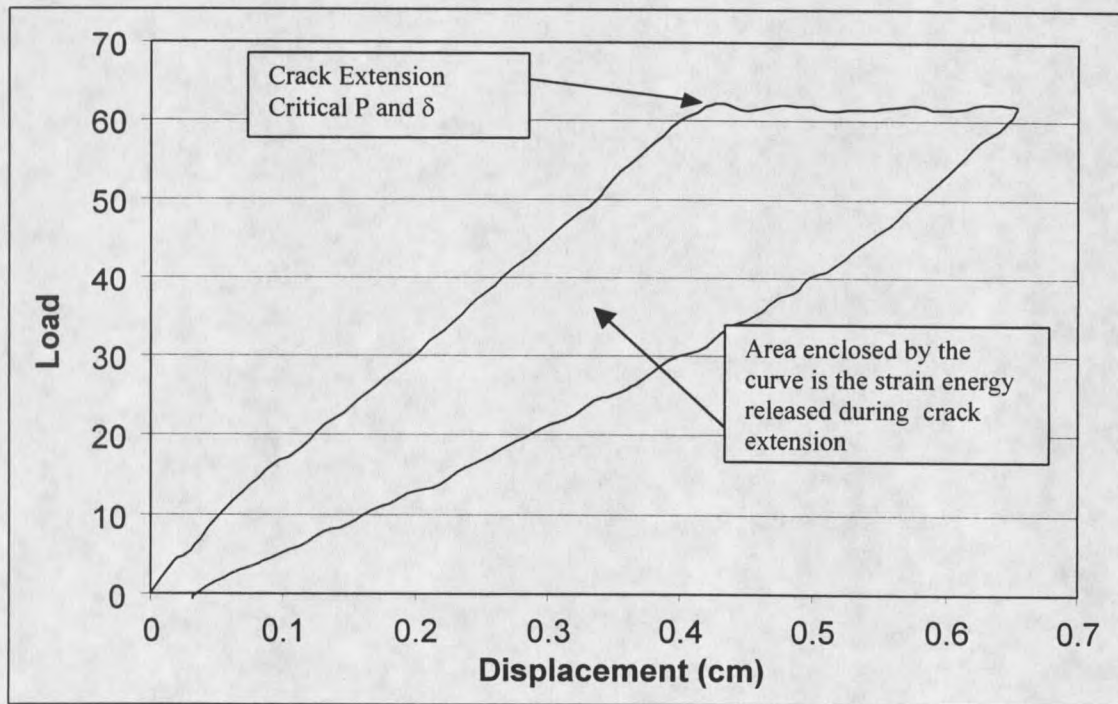


Figure 8. Typical loading-unloading curve for DCB test.

$$G_{Ic} = \text{Area} / b(a_2 - a_1) \quad (3)$$

Where: Area = area enclosed by loading/unloading curve

b = sample width

a_1 = initial crack length

a_2 = final crack length

will not give an initiation value for G_{Ic} from the Teflon insert film as recommended by ASTM D 5528.

The end-notched flexure (ENF) test has emerged as the standard test method for calculating critical SERR in Mode II type crack growth. Typical specimen geometry and loading for an ENF sample is shown in Figure 9. This sample produces shear at the

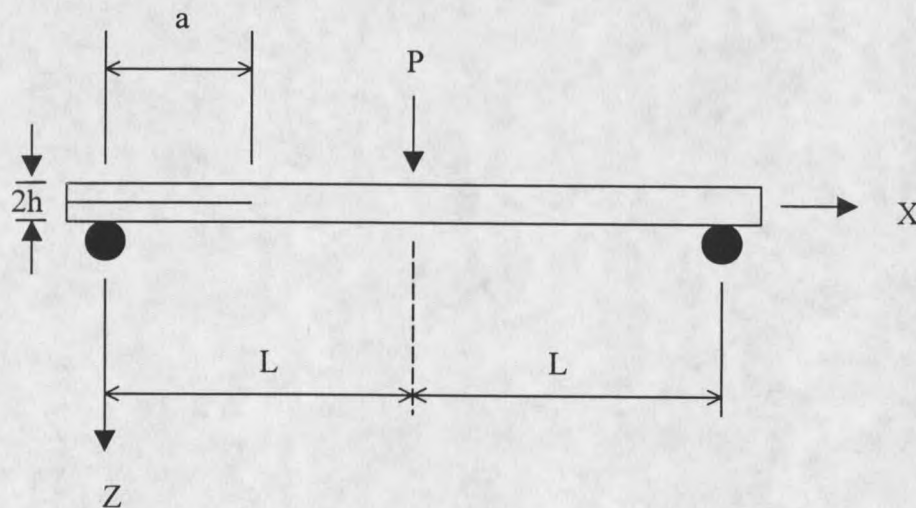


Figure 9. ENF geometry and loading.

mid-plane of a composite specimen loaded in three-point bending. When a critical load is reached, the crack advances, usually in an unstable manner [16]. A formula used to

calculate G_{IIc} based on beam theory [25, 26] is presented as Equation 4.

$$G_{IIc} = 9P^2 a^2 C / 2b(2L^3 + 3a^3) \quad (4)$$

Where: P = critical load at propagation

a = initial crack length

C = specimen compliance

b = sample width

L = one-half support spacing distance

Analytical Prediction of Strain Energy Release Rate

Many analytical methods have been developed for use with finite element analysis (FEA) to predict strain energy release rates in each mode of crack extension. Two popular ways to calculate G are by (1) calculating the change in strain energy in an FEA model with an associated crack extension (virtual crack extension – VCE) [25], and (2) calculating the energy required to close a crack front by a small increment (virtual crack closure technique – VCCT) [8, 10, 12, 13, 21, 28-30]. Both methods have gained acceptance, but the virtual crack closure technique has emerged as the preferred method. It has the benefit of allowing separate G calculations for each mode of crack extension.

The VCCT is based upon Irwin's hypothesis that the energy absorbed during crack extension (da) is equal to the work done to close that crack by the same incremental amount. This is the concept of the crack closure integral [23, 28]. Rybicki and Kanninen [28] applied this concept to the calculation of strain energy release rates with the finite element model. It has subsequently been expanded for use with most common element

types in FEA [29, 30].

The VCCT can be applied by two different methods. The one-step VCCT (VCCT-1) only requires one finite element run to calculate the SERR. This has obvious benefits in saving computing time for detailed analyses with long solution times. In this method, the forces at the crack tip are multiplied by the displacements behind the crack tip. Different formulas have been derived for the various finite elements [30]. A schematic of VCCT-1 for a 2-dimensional 8-node quadrilateral element formulation is presented in Figure 10. The formulas for G_I and G_{II} from reference [30] are presented as Equations (5) and (6) where u and v are the nodal displacements in the x and y directions.

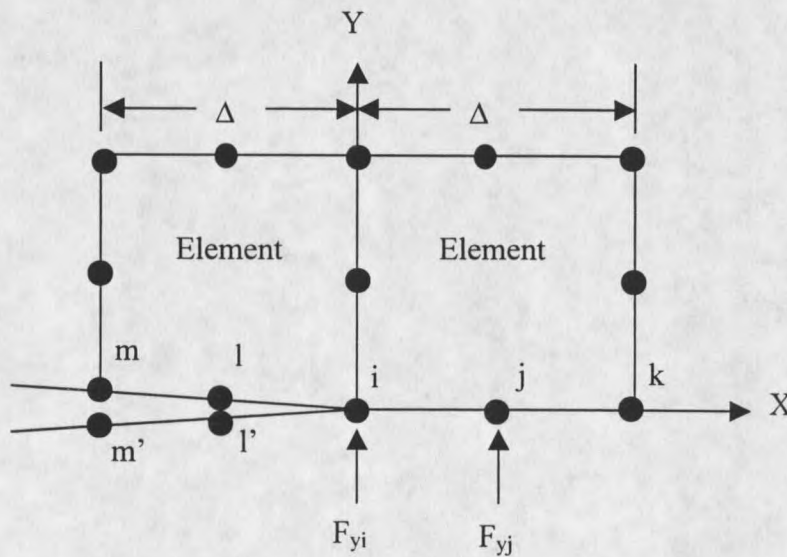


Figure 10. VCCT-1 schematic with 8-node quadrilateral elements.

$$G_I = -1/(2\Delta)[F_{yi}(v_m - v_{m'}) + F_{yj}(v_l - v_{l'})] \quad (5)$$

$$G_{II} = -1/(2\Delta)[F_{xi}(u_m - u_{m'}) + F_{xj}(u_l - u_{l'})] \quad (6)$$

This technique may be used with a variety of element types and does not require the use of a quarter point nodal placement element with a stress singularity at the crack tip. No stresses are used in the calculation and it may be utilized with a relatively coarse mesh. Rybicki and Kanninen [28] found good results for the calculation of stress intensity factors with the VCCT-1 method and constant-strain elements at ratios of crack length to crack extension (a/da) as low as five (5). Martin [3] has reported that when using the VCCT-1 technique, there was no mesh size dependency if the crack was grown within the same material type, but found that if the crack grew at a bimaterial interface, the calculations were mesh size dependent. However, he gave no recommendations for acceptable (a/da) ratios. Values for (a/da) ratios from 50 to 200 have been recommended for general fracture mechanics analysis with FEA [27].

The two step VCCT (VCCT-2) uses two successive FEA runs (Fig. 11) to

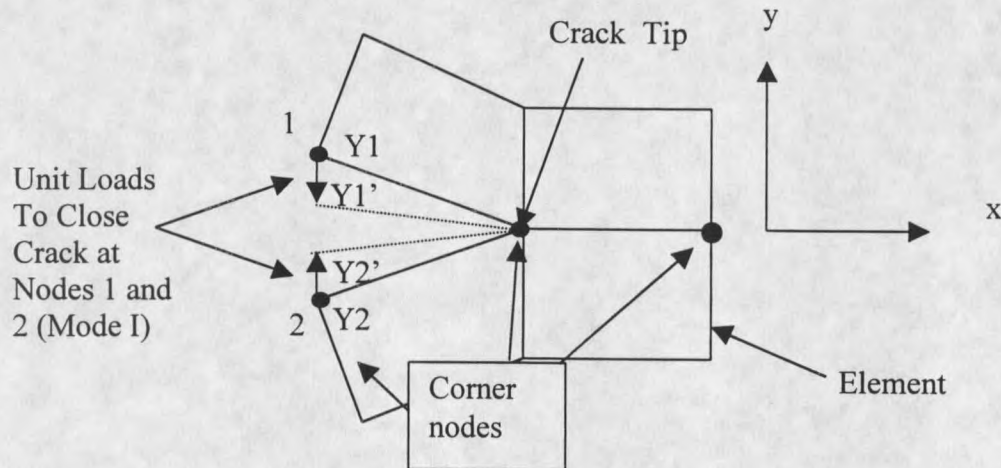


Figure 11. VCCT-2 schematic for Mode I closure.

calculate G values. The first analysis is performed with the specified loading on the structure, while the second analysis uses unit loads at the nodes immediately behind the crack front to close the crack by some amount. The elements at the crack tip are shown in detail in Figure 11. The corresponding formulas to calculate G in Mode I and Mode II are given as Equations (7) and (8), where Y' and X' denote the displacements after the unit loads are applied to close the crack.

$$G_I = \frac{(Y_1 - Y_2)^2}{\frac{(Y_1 - Y_2) - (Y'_1 - Y'_2)}{2(\text{Element width})}} \quad (7)$$

$$G_{II} = \frac{(X_1 - X_2)^2}{\frac{(X_1 - X_2) - (X'_1 - X'_2)}{2(\text{Element width})}} \quad (8)$$

By examining the displacements with the unit loads, one can calculate the force required to completely close the crack by some length (da). In Figure 11, the loads are placed at the corner nodes for an element type without mid-side nodes. The unit loads may be placed at the mid-side nodes if a higher order element is used. This would reduce the length of the crack extension by one half for a given element size and the element width term in the denominator of Equations (7) and (8) would be replaced by one half the element width. This term should more appropriately be labeled the crack closure length (da), depending on the element type used.

Jerram [31] first reported utilizing this technique with constant strain elements. Hellen and Blackburn [32] had errors of up to 20% in predictions for G when using this

technique with higher order elements. This method will be investigated further in Chapter 6, which deals with FEA results from this study.

Mode Interaction and Failure Criteria

The previous developments for experimental and analytical methods can be combined to perform predictive work with fracture mechanics in composite structures. To do so, designers must understand how crack growth interaction occurs when more than one mode of crack extension is present. In the following development, Mode III is not included because it was not observed in the experimental substructure tests.

Many investigators have recently addressed mixed-mode delamination in composite structures. The development of the mixed-mode bending test (MMB) to calculate G values with mixed-mode loading has facilitated this research [17, 26, 33, 34]. The MMB test allows for any mixed percentage of Mode I and/or Mode II growth to be achieved simultaneously, and for the critical G value in each mode at propagation to be calculated. Mixed-mode interaction criteria for predictive work with FEA can then be developed.

As mentioned previously, a crack will advance when G equals G_c in a particular mode. When a mode mix is present, the following general form of interaction has been proposed [26] for combined Mode I and II growth (Eq. 5). The key to the implementation

$$(G_I/G_{Ic})^{m/2} + (G_{II}/G_{IIc})^{n/2} = 1 \quad (5)$$

of Equation (5) has been finding the best exponents m and n to match the experimental behavior for particular material systems. According to Reeder [35], a value of two is

most often used in the literature for both m and n . This makes the overall exponent for each term one, and gives the common and easily implemented “linear interaction criterion”. A linear interaction is pleasing from a theoretical point of view since strain energy release rate is a scalar quantity. A graphical representation of the linear interaction criterion is shown in Figure 12. Russell and Street [26] found good agreement

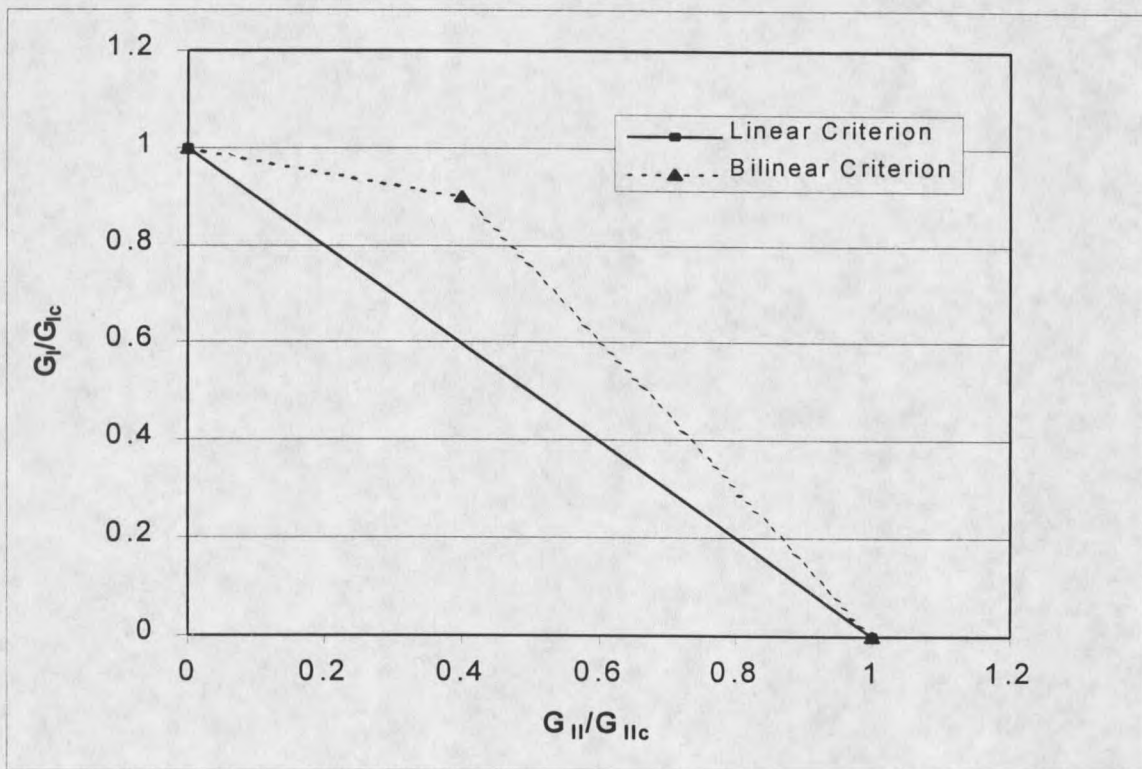


Figure 12. Generalized graphical representation of the linear and bilinear failure criteria.

between predictions and test results for unidirectional graphite/epoxy prepreg samples using the linear interaction criterion. In addition, Alif et al. [17] observed mixed mode behavior in a woven fabric carbon/epoxy laminate that followed a linear relation between G_{Ic} and G_{IIc} . However, Reeder [35] and Konig et al. [33] have found that a bilinear

failure criteria works better for some material systems due to the observed increase in G_{Ic} at certain intermediate mode ratios in the vicinity of $G_I/G_{II} = 1$ [35]. This is shown graphically in Figure 12. In particular, Reeder found the bilinear criterion gave better predictions for carbon/epoxy systems. He also found that systems with tougher thermoplastic matrices followed the linear criterion better and recommended testing of MMB samples to see which criteria a particular material will follow.

The implementation of these developments into predictive work with FEA is fairly straightforward [3]. The first step is the establishment of an accurate material toughness database for the material under consideration. Next, an FEA model of the problem is produced and a technique such as the VCCT-1 method is used to calculate the strain energy release rates at that particular load. Once the G values are found, a suitable interaction criterion may be used to predict delamination growth. The actual load to propagate a delamination may then be calculated from the interaction criterion and the fact that the SERR values increase with the square of the applied load in FEA calculations. Thus, load may be scaled appropriately so that the interaction criterion for crack growth is satisfied. This overall global-local design process with FEA is presented as a flowchart in Figure 13. The procedure for using fracture mechanics to predict delamination propagation loads is presented in more detail for designers and analysts in Appendix A.

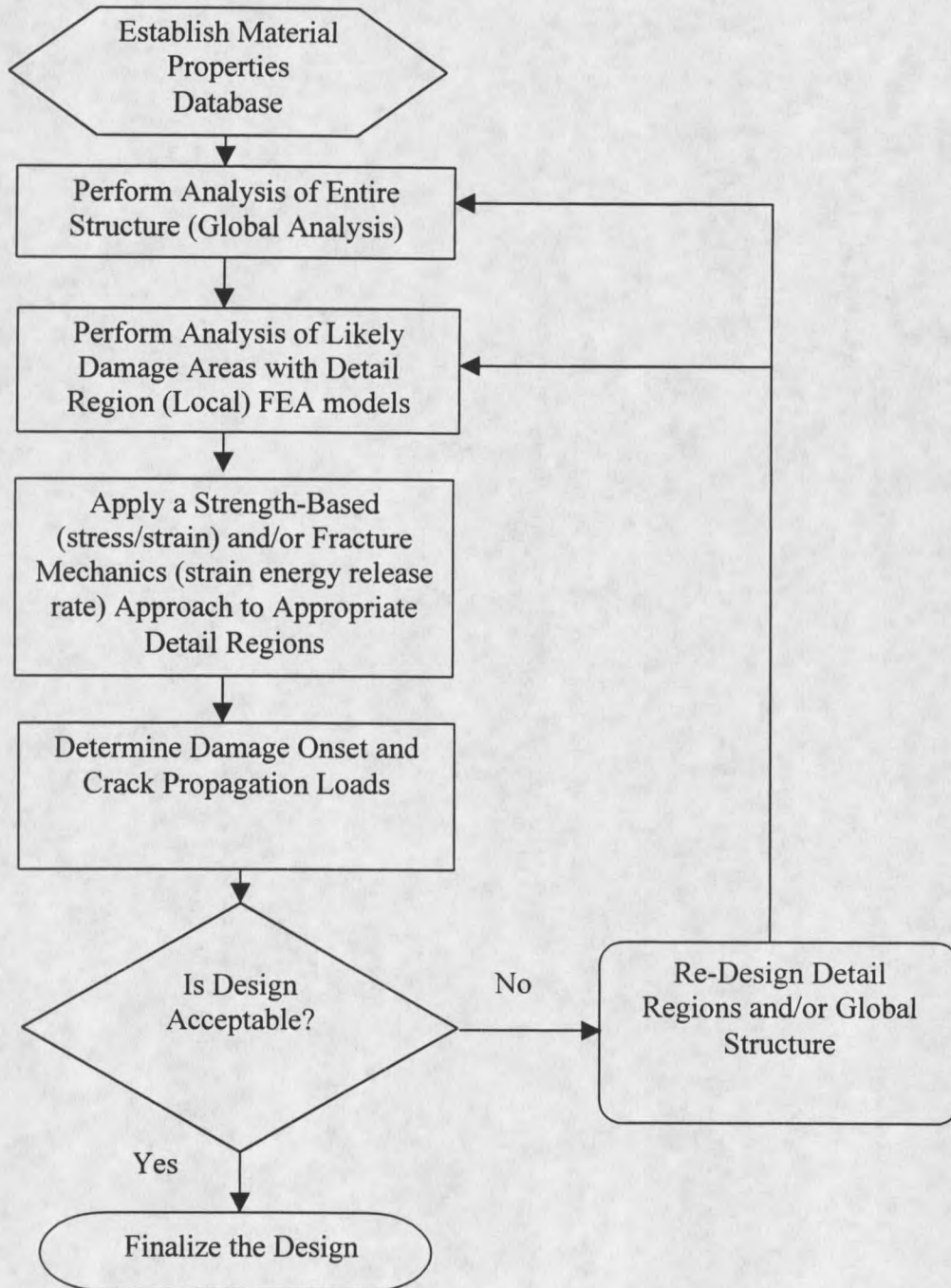


Figure 13. Design flowchart for global-local analysis with FEA.

CHAPTER 3

EXPERIMENTAL METHODS

Materials and Manufacturing

There were two main categories of specimens investigated in this study. The first group was comprised of DCB and ENF specimens as described in Chapter 2. These specimens were used to collect basic delamination data for various fabrics and interface lay-up configurations. The second group consisted of specimens that represented blade substructures in the skin-stiffener detail regions. These specimens were tested using different loading conditions, manufacturing methods, resin materials, geometries, and fabric lay-ups.

All specimens tested were manufactured at MSU-Bozeman using Resin Transfer Molding (RTM). In RTM, dry fabric preform is placed in a mold cavity, and catalyzed resin is then pumped through the cavity space. Once the mold has completely filled, the process stops, and the resin is allowed to cure. The cured composite is removed from the mold cavity after 24 hours, and post-cured at 60⁰ C for two hours to ensure full cross-linking of the thermoset polymer matrix.

A Polyester/E-glass system was used for most of the specimens tested in this investigation. This material system is representative of the low-cost materials used by the wind turbine industry. CoRezyn unsaturated orthophthalic polyester (63-AX-051), made

by Interplastic Corporation, with 2% MEKP (by volume) added as a catalyst, was the primary resin used in this study. In addition, a few specimens were made with polyester/PET (PET P460-06) from Alpha Owens-Corning (AOC), and polyurethane (Polytek Poly 15-D65) matrices for comparative purposes. The reinforcing E-glass fabric was an Owens-Corning (Knytex) stitched D155 fabric for the 0^0 layers in all specimens. The weft unidirectional D155 has an areal weight of 526 g/m^2 . The (+45/-45) fabric used was the stitched DB120; also from Owens-Corning, with an areal weight of 407 g/m^2 .

DCB and ENF Specimens

The DCB and ENF specimens were manufactured as flat plates with a Fluoro-Peel Teflon release film at the mid-plane to serve as the crack initiation film. Three lay-ups were tested. They were $[(0)]_{10}$ at 36 % fiber volume percentage (V_f), $[(0)_2/(45/-45)/(45/-45)/(0)_2]$ at 34 % V_f , and $[(45/-45)]_{10}$ at 26 % V_f . Both specimen types were cut from flat plates with a diamond blade saw to a standard specimen size of 2.54 cm in width, by 17.8 cm in length.

The DCB specimens had 2.54 cm wide stock piano hinges bonded to both faces with Hysol EA 9302.2NA adhesive for the load application points (Fig.7). Specimen and hinge bonding surfaces were sanded with 240 grit sand-paper and wiped clean before adhesive application. In order to get an initiation value for G_{Ic} right from the starter film tip as recommended by ASTM D 5528 [24] the specimens were not pre-cracked. Tests were performed by loading and unloading the specimens so that both the MBT and the Area Method test results could be calculated for each test as outlined in Chapter 2. Crack growth was measured at the end of each test by using a marker dye to penetrate the crack,

clearly showing the crack tip. The crack length was then measured from the load application points and recorded. The crack growth front was generally uniform across the specimen width. In this way, the final crack length for the area method and the initial crack length for the following test were determined. Tests were performed at different crack lengths for each specimen which enabled investigation of R-Curve behavior for Mode I crack growth.

The critical load and displacement for use in the equations in Chapter 2 were determined by the sudden change in slope or the onset of non-linearity in the load-displacement curves (Fig.8) to ensure conservative values for G_{Ic} . These points were selected from the load-displacement curves and entered into the equations as the critical load and displacement values for the MBT method. The area enclosed by the curve was determined by choosing nine key data point sets from the curve and calculating the area with a simple computer program. To validate this calculation, some curves were scanned into a photo-analyzing program at high resolution to calculate the pixels enclosed in the graph. The enclosed area was determined and the two methods were found to agree within 5 percent.

The critical load for the ENF specimens was taken as the onset of non-linearity in the load-displacement curve. In the ENF test, the load increased until a slight non-linearity occurred followed by a large unstable crack advancement (Fig.14). Because of this, only one value of G_{IIc} was obtained for each ENF specimen, and no R-Curve behavior could be investigated.

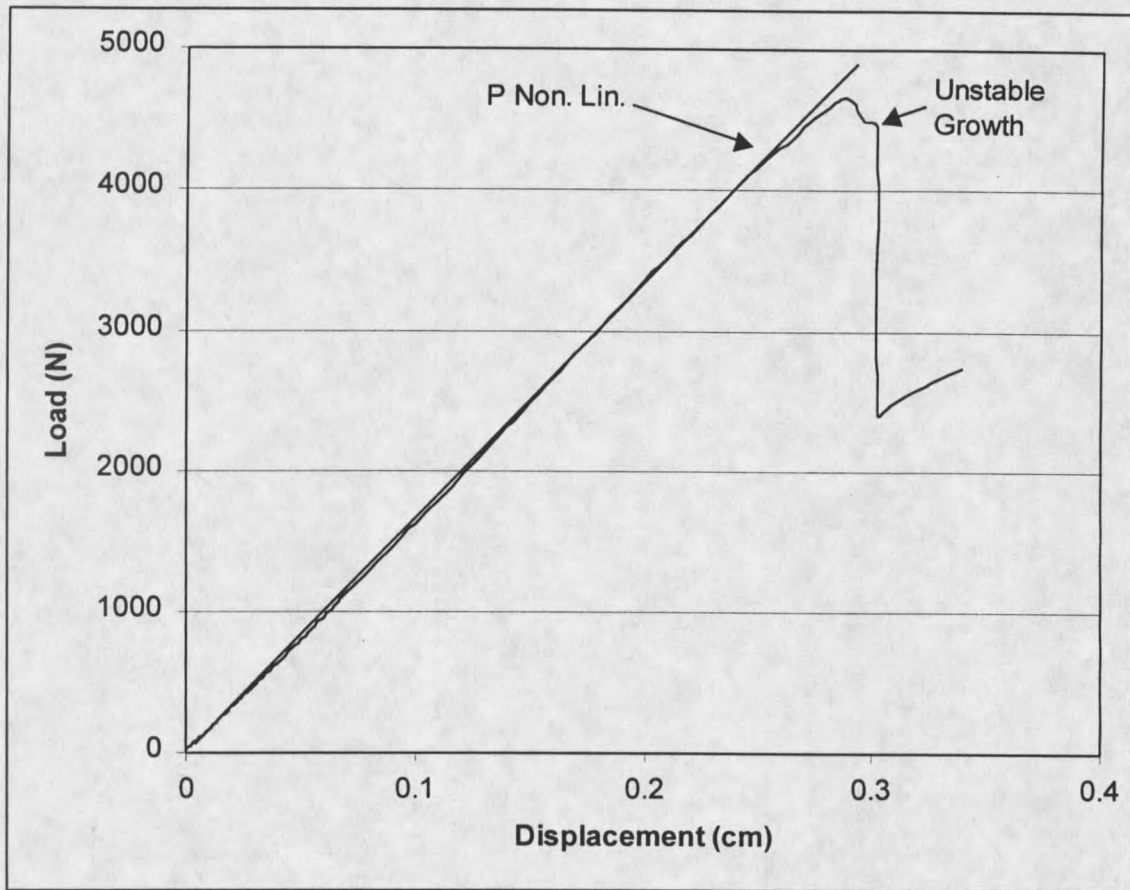


Figure 14. Typical load-displacement curve for ENF test.

Substructure Testing

A variety of tests were performed to investigate the mechanisms and modes of fracture for skin-stiffener intersection detail regions. The test specimens varied in stiffener geometry, materials, delamination interface lay-up, skin and flange stiffness, manufacturing method, and loading cases. A list of the lay-up schedule used for the skin and flange for each specimen type is presented in Table 2. A summary of the test matrix and a description of the various specimen types are presented in Table 3. These tests also provided data for substructure modeling validation with the ANSYS finite element code.

Table 2. Ply orientations and laminate identification codes for substructure tests.

Laminate Configuration*	ID Code
Thin-flanged Specimens	
$[+45/-45/0_2/+45/-45]_2$	S1 (skin)
$[+45/-45/0_2/+45/-45]$	F1 (flange)
Thick-flanged Specimens	
$[+45/-45/0_2/+45/-45]$	S2 (skin)
$[90/0/+45/-45]_s$	S3 (skin)
$[(+45/-45/0_2/+45/-45/0_2/+45/-45)_s/+45/-45/0_2/+45/-45]$	F2 (flange)
$[(90/0_2/+45/-45/0_2/+45/-45)_s/+45/-45/0_2/+45/-45]$	F3 (flange)
$[+45/-45/0_2/+45/-45]_s$	Web (used in all specimens)

*Thick-flanged lay-ups include $[+45/-45/0_2/+45/-45]$, which is half of the web lay-up continued onto the top of the flange cap section.

Two different T-mold configurations were used to produce the skin-stiffener specimens. The geometry and loading for the first batch of specimens, referred to as the "thin-flanged" specimens, is shown in Figure 15. The diagram for the "thick-flanged" specimens is displayed in Figure 16. The different designs were utilized to investigate specimens displaying different failure modes. The thin-flanged specimens were expected to display initial damage at the web-flange fillet region, followed by delamination toward the flange tip. In contrast, the thick-flanged specimens were anticipated to fail at the flange tip area, with a delamination then progressing toward the web centerline. The ability to predict this different failure behavior for different geometries could then be established with the FEA models.

The thin-flanged stiffeners were manufactured two ways. They were either co-cured in the mold with the skin, or secondarily bonded to the skin with an adhesive. The secondary bonded type was molded with a layer of release film at the skin and stiffener

Table 3. T specimen substructure test matrix.

Geometry From Table 2		Manufacturing					
Flange	Skin	Bonding	Matrix Material	Delamination Interface Lay-up	Loading	# Specimens	Motivation
Thin-flanged Stiffeners							
F1	S1	Co-cured	Polyester	(+45/-45)	Tension	11	Baseline pull-off specimens, investigate damage initiation and growth
F1	S1	Co-cured	Polyester	(+45/-45)	Compression	3	Investigate compressive behavior and damage location
F1	S1	Secondary Bonded (0.15 mm bond) (Hysol Epoxy)	Polyester	(+45/-45)	Tension	12	Investigate performance changes with secondary bonding of skin to stiffener
F1	S1	Variable Bond Thickness (Hysol Epoxy)	Polyester	(+45/-45)	Tension	11	Investigate performance changes with variable bond-line thickness
F1	S1	Secondary bonded (Plexus Methacrylate)	Polyester	(+45/-45)	Tension	6	Investigate bonding of commonly used commercial adhesive
F1	S1	Co-cured	Polyester/PET	(+45/-45)	Tension	4	Investigate delamination resistance of different matrix materials
F1	S1	Co-cured	Polyurethane	(+45/-45)	Tension	3	
Thick-flanged Stiffeners							
F2	S2	Co-cured	Polyester	(+45/-45)	Tension	6	Investigate specimens exhibiting flange tip failures, vary the skin stiffness and interface lay-up
F3	S3	Co-cured	Polyester	(0/0)	Tension	3	

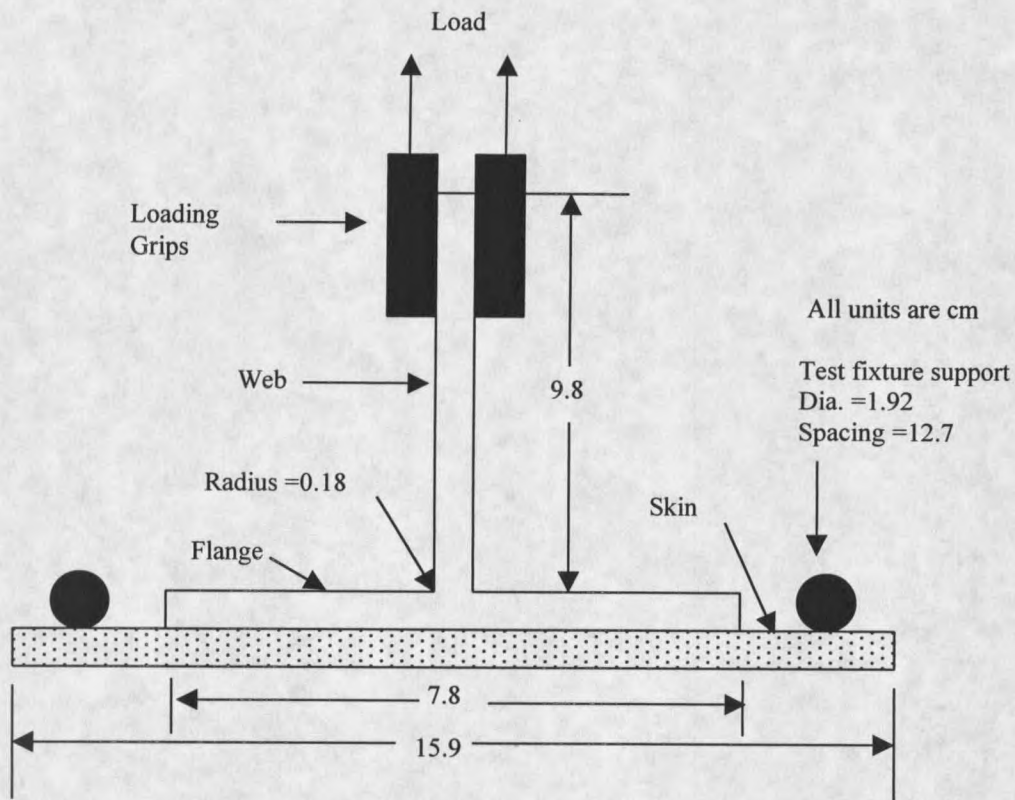


Figure 15. Geometry and loading for thin-flanged stiffener tests.

intersection. The flange and skin cured in the same mold, but did not bond together due to this film layer. To investigate bonding issues, two different adhesives were compared, and the bond-line thickness was varied considerably. The adhesives used were the Hysol EA 9309.2NA and ITW Plexus methacrylate (A0425).

Three different resin systems were compared for relative delamination resistance in static pull-off tests. The resins used were CoRezyn polyester, the polyester/PET blend from Alpha Owens-Corning, and the polyurethane made by Polytek. These resins were expected to have vastly different toughness values allowing investigation of performance changes with different matrix formulations.

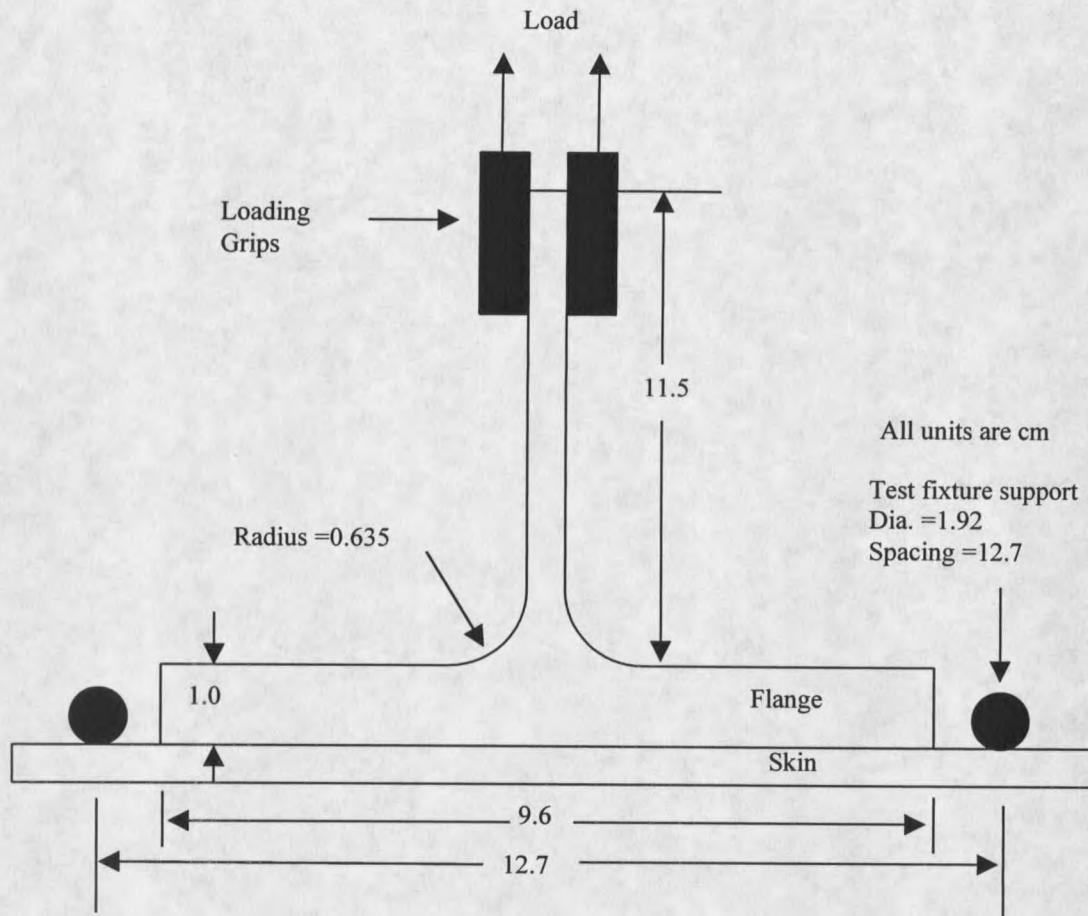


Figure 16. Geometry and loading for thick-flanged stiffener tests.

Flange and skin ply lay-ups were varied to track influences of bending stiffness and delamination interface lay-up on stiffener performance for the thick-flanged specimens. In addition, by varying the interface plies, FEA predictions could be validated more thoroughly, since toughness has been observed to change with delamination ply interface orientation [16].

Two different load cases were applied to the stiffener specimens. They were static tensile pull-off loading, and static compressive loading. These tests were

performed on the simply supported testing apparatus shown in Figure 17. The load was applied to the specimen by gripping the upper 2.5 cm of the web in the hydraulic grips

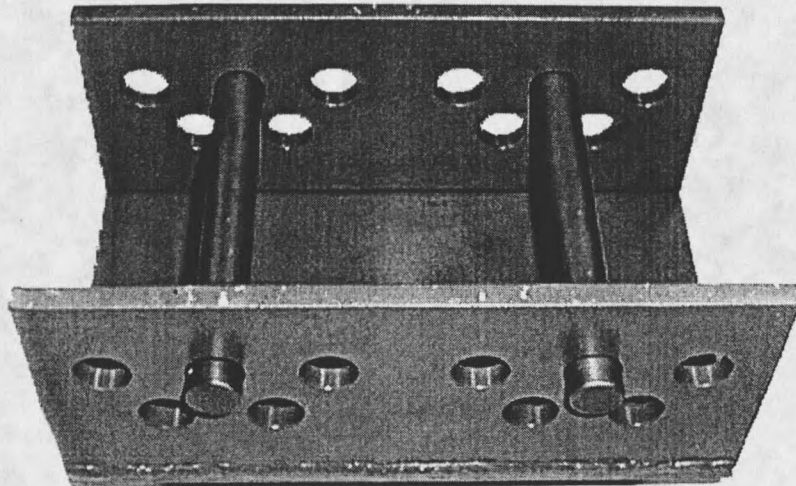


Figure 17. Simply supported test fixture for tensile and compressive stiffener tests.

and reacting the load with the bars in the test fixture (Fig. 17). Support spacing was 12.7 cm for all stiffener tests.

The static pull-off tests were performed in displacement control mode on an Instron 8562 servo-electric testing machine. Data was collected and graphed for load vs. actuator displacement (Fig. 18). In addition, initial fracture load, maximum load, and maximum displacement were manually recorded to verify each plot used in subsequent analysis and to compare specimen performance. Initial damage onset was taken as the point where either the load-displacement curve became non-linear, or the load suddenly dropped by more than 2.6 N/cm. This correlated well with audible and visual damage onset values.

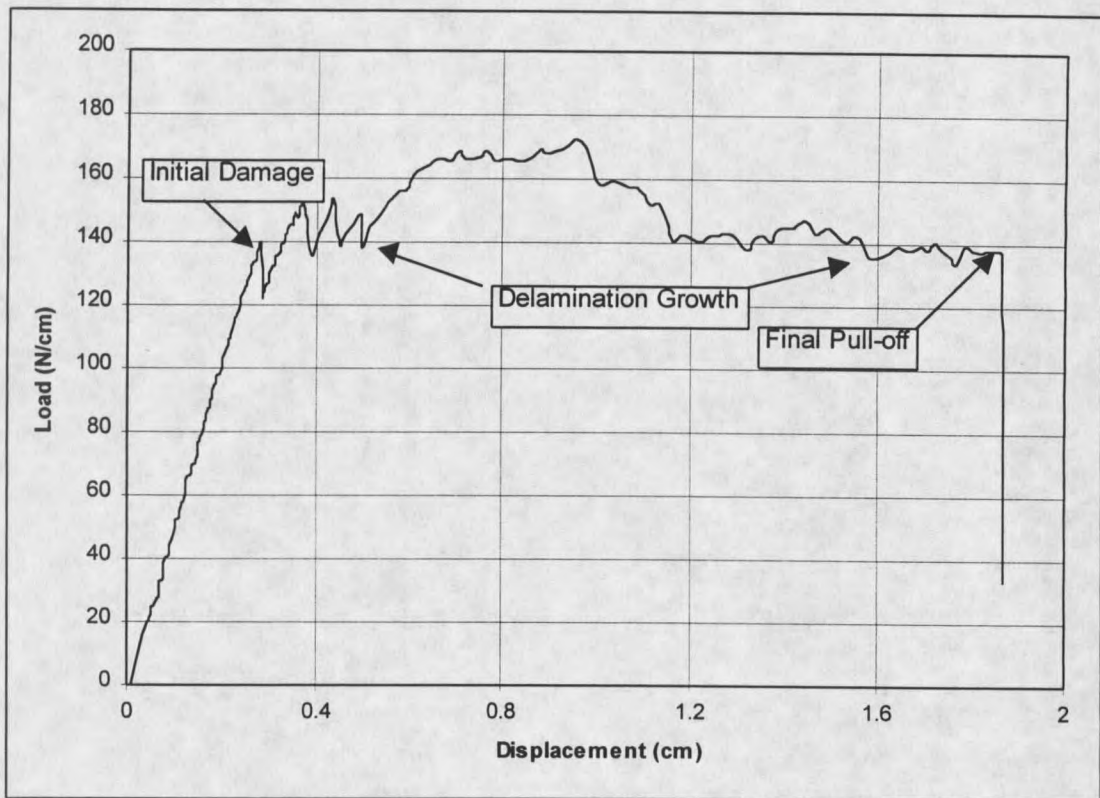


Figure 18. Typical load-displacement curve for thin-flanged stiffener pull-off test.

The static compressive tests were performed in the same testing apparatus, except that the specimen was placed on top of the support bars in the fixture and pushed downward. Initial damage loads, maximum loads, and maximum displacements were recorded from visual and audible observations to compare with the output load-displacement graphs. The onset of non-linearity in the load-displacement curve (Fig. 19) was interpreted as the initial damage load.

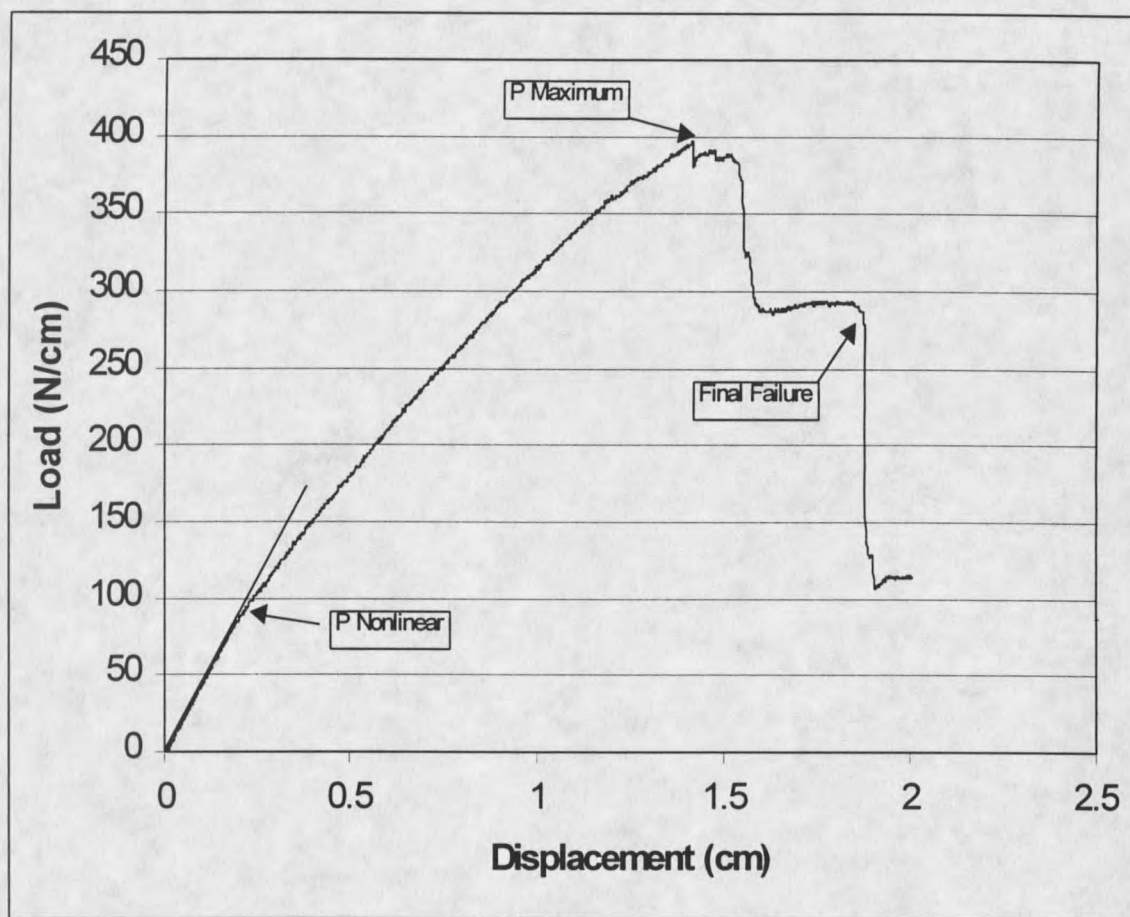


Figure 19. Typical load-displacement curve for compressive thin-flanged stiffener test.

CHAPTER 4

NUMERICAL METHODS

Finite element analysis (FEA) has been established as an indispensable tool for research and design work in the various fields of engineering. It allows structural designers to investigate the effects of parameters such as geometry, material, and loading on design performance. When performed correctly, FEA may drastically reduce the dependence on expensive substructure and full scale experimental testing during the design development process [3].

However, FEA is not a substitute for a thorough understanding of the underlying engineering principles, such as material behavior, failure theories, or fracture mechanics. These principles must be properly applied, and the FEA input and output properly interpreted, to give accurate and meaningful results. In fact, it is commonplace for the first handful of analyses for a design to be incorrect until refinements are made in such areas as mesh sizing, boundary conditions, loading, and inclusion of nonlinear effects. In addition, reliance on FEA results should only come as a result of experience gained by validation with experimental testing. Once benchmark studies have been performed, confidence in the analysis procedures is attained. In this way, FEA reduces the reliance on experimental testing over the long term.

The overall approach of this research follows an experimental/numerical validation scheme. As mentioned in Chapter 1, full-scale (global) blade models are not usually refined enough to predict critical detail region (local) performance. This is a problem, since damage may initiate at these sites. A combined global/local approach (Fig. 13) seems to be the evolving design methodology for skin-stiffened structures [3, 7, 10]. In this approach the loading conditions from the global model are transferred to smaller substructure models that appear to be “hotspots” for stresses. This is performed until adequate detail is incorporated into the models to predict such items as initial damage loads and location, and damage tolerance. This knowledge allows the designer to make necessary changes to the local and/or global structure, and iterate on this procedure until an acceptable design is achieved.

In the current research, testing and analysis focused on the local detail region level as part of an overall project that includes global analysis. Analytical modeling of detail regions through FEA was developed and validated with experimental results. The goals of the analytical modeling were to formulate accurate predictive capability and design methodologies for detail regions with FEA. By combining the experimental and analytical modeling, the objectives of establishing design guidelines and predictive capability for skin-stiffeners could be achieved.

Model Generation

FEA was used to model the two primary experimental specimen types used in this study, namely the double cantilever beam (DCB), and the skin-stiffener substructure (T).

The goals for the FE model of the DCB were to compare the predictions from the model, based on the VCCT techniques, with the experimentally calculated G_{Ic} values. The T specimens were modeled in order to establish predictive ability of blade substructure sections at the detail region level. It was hoped that analysis techniques could be implemented that used basic material strength and fracture data, appropriate FE models, and suitable failure criteria, to predict T specimen test results.

DCB Models

The DCB was modeled with a 2-D plane strain analysis using 8-node quadrilateral elements (plane 82) in the ANSYS 5.3 finite element code (Fig. 20). Half symmetry was used at the specimen thickness mid-plane to simplify the model. The load was applied as a nodal force at the upper left corner node which was restricted to translate in the vertical direction only. The symmetry condition was enforced by restraining all nodes along the mid-plane, up to the crack tip, with zero displacement in the y-direction. The crack length (a) was set by picking a node with appropriate coordinates in the x-direction to create a specified debond length. The mesh sizing was varied to find the mesh sensitivity of the VCCT techniques. This is discussed further in the Analytical Results section of Chapter 6. Typically, the DCB had 4 elements through the half-thickness, with the elements surrounding the crack tip highly refined to capture the stress gradients at the crack tip. Typical material properties [1] used for the D155 and DB120 fabric layers in the FE models are shown in Tables 4 and 5.

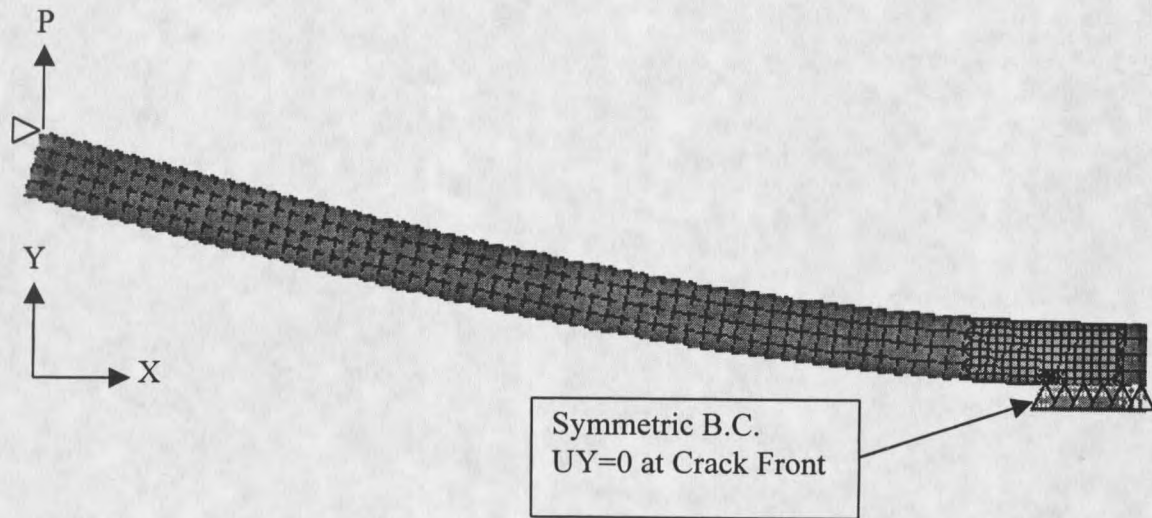


Figure 20. Deformed finite element mesh of DCB specimen with a delamination.

In order to input the properties into ANSYS correctly for the 2-D model, the relations for Poisson's major and minor ratios were implemented. This was necessary to correctly change the material properties from the axes used for material testing, to the various ply orientations in the model. This involved simply changing E_x (E_L) etc. from the material property axes, to the appropriate local direction in each layer of the FE model. When doing this, the major Poisson's ratios (ν_{12} , ν_{23} , ν_{13}) and the minor Poisson's ratios (ν_{21} , ν_{32} , ν_{31}) must be treated correctly. These values are related according to Equation 6 [37], due to compliance symmetry in the constitutive properties.

$$\nu_{ij} / E_i = \nu_{ji} / E_j \quad (6)$$

If these ratios are not properly applied, a built-in material-checking feature in ANSYS will not allow the model to be solved, due to a lack of positive definite properties. If a

Table 4. Elastic Constants and Strengths for Unidirectional Material D155 at a $V_F = 36\%$ [1].

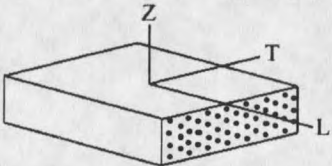
Physical Elastic Constants of Material D155, $V_F = 36\%$			
Property and test plane	Test Values	Average	s.d.
$E_{L,(LT \text{ plane})}$, GPa	28.1, 27.0, 29.8	28.3	1.4
E_L , (LZ plane), GPa	28.0, 28.3, 27.6	28.0	0.4
E_T , (TZ plane), GPa	8.00, 7.31, 7.93	7.75	0.38
E_Z , (ZX plane), GPa	7.10, 7.65, 7.38	7.38	0.28
ν_{LT}	0.329, 0.320, 0.301	0.32	0.01
ν_{LZ}	0.305, 0.338, 0.331	0.33	0.02
ν_{TZ}	0.466, 0.395, 0.449	0.44	0.04
G_{LT} , GPa	3.31, 3.35, 3.23	3.30	0.06
G_{LZ} , GPa	3.03, 2.72, 2.70	2.82	0.19
G_{TZ} , GPa	2.78, 3.12, 1.76	2.55	0.71
Ultimate Strengths of Material D155, $V_F = 36\%$			
Property and test plane	Test Values	Average	s.d.
UTS_L , (LT plane), MPa	891, 814, 883, 838	856	37
UTS_L , (LZ plane), MPa	679, 672, 685, 646	671	17
UTS_T , (TZ plane), MPa	26.6, 36.0, 30.4, 32.9, 29.0	31.0	3.6
UTS_Z , (ZT plane), MPa	21.7, 18.7, 20.4, 18.1	19.7	1.6
UTS_Z , (ZL plane), MPa	19.4, 17.7, 22.3, 17.1, 15.2	18.4	2.7
τ_{LT} , MPa	95.1, 82.1, 78.8	85.3	8.7
τ_{LZ} , MPa	79.6, 77.3, 77.1, 63.2	74.3	7.5
τ_{TZ} , MPa	19.9, 17.6, 12.0	16.5	4.0
*Shear properties listed were determined by notched beam, ASTM D5379			
			

Table 5. Static longitudinal, transverse, and simulated shear properties for D155 and DB120 unidirectional materials [1].

			Longitudinal Direction								Transverse Direction				
			Elastic Constants				Tension		Compression		Shear	Tension		Compression	
Fabric	Lay-up	V _F %	E _L GPa	E _T GPa	v _{LT}	G _{LT} GPa	UTS _L MPa	ε _U %	UCS _L MPa	ε _U %	τ _{TU} MPa	UTS _T MPa	ε _U %	UCS _T MPa	ε _U %
D155	[0] ₆	45	37.0	8.99	0.31	4.10	986	2.83	-746	-2.02	94.2	27.2	0.30	-129	-1.67
DB120*	[0] ₁₆	44	26.5	7.52	0.39	4.12	610	2.49	-551	-2.08	84.9	24.9	0.33	-90.8	-1.21

Notes: E_L - Longitudinal modulus, v_{LT} - Poisson's ratio, G_{LT} and τ_{TU} - Shear modulus and ultimate shear stress from a simulated shear (±45) ASTM D 3518 test. UTS_L - Ultimate longitudinal tensile strength, ε_U - Ultimate tensile strain, UCS_L - Ultimate longitudinal compressive strength, ε_U - Ultimate compressive strain.
Coupons had a 100 mm gage length with a 0.02 mm/s testing velocity. * DB120 fabric was separated into a +45 and a -45 orientation and then rotated to 0 degrees to form a unidirectional material

DCB specimen had different fabric types in the same model, a separate area represented each fabric layer. The orthotropic material properties for the fabric were then attributed to that area before mesh generation to ensure proper lay-up in the model.

Both the VCCT-1 and VCCT-2 techniques were applied to the DCB models to calculate G_{Ic} and determine mesh sensitivity for both methods as presented in Chapter 2.

Substructure Models

FEA models were created for both the thick and thin flange T specimens. They consisted of a 2-D plane strain analysis with 8-node quadrilateral (Plane 82) element types. The plane strain assumption has been used by other investigators to model skin-stringer debonding [3, 8-10, 29]. Half symmetry about the vertical mid-line of the web was used to simplify the models (Figs. 21 and 22) by restricting the nodes along the mid-line to have zero x-displacement. The support from the test fixture bar was modeled as a condition of no y-displacement at a nodal position of $x = 6.35$ cm on the top of the skin. The applied force observed in the experimental results was normalized per unit of specimen width and divided by two to get the load applied to the half-model. This load was applied as a nodal force in the y-direction at the top centerline of the web.

The thick flange models were analyzed to predict initial damage at the flange tip and delamination growth along the skin-flange interface. Along the delamination interface, plies were modeled individually for each of the four plies on either side of the interface. In the localized region of the delamination front, each ply layer had at least four elements through its thickness. In some cases, even more elements were used to

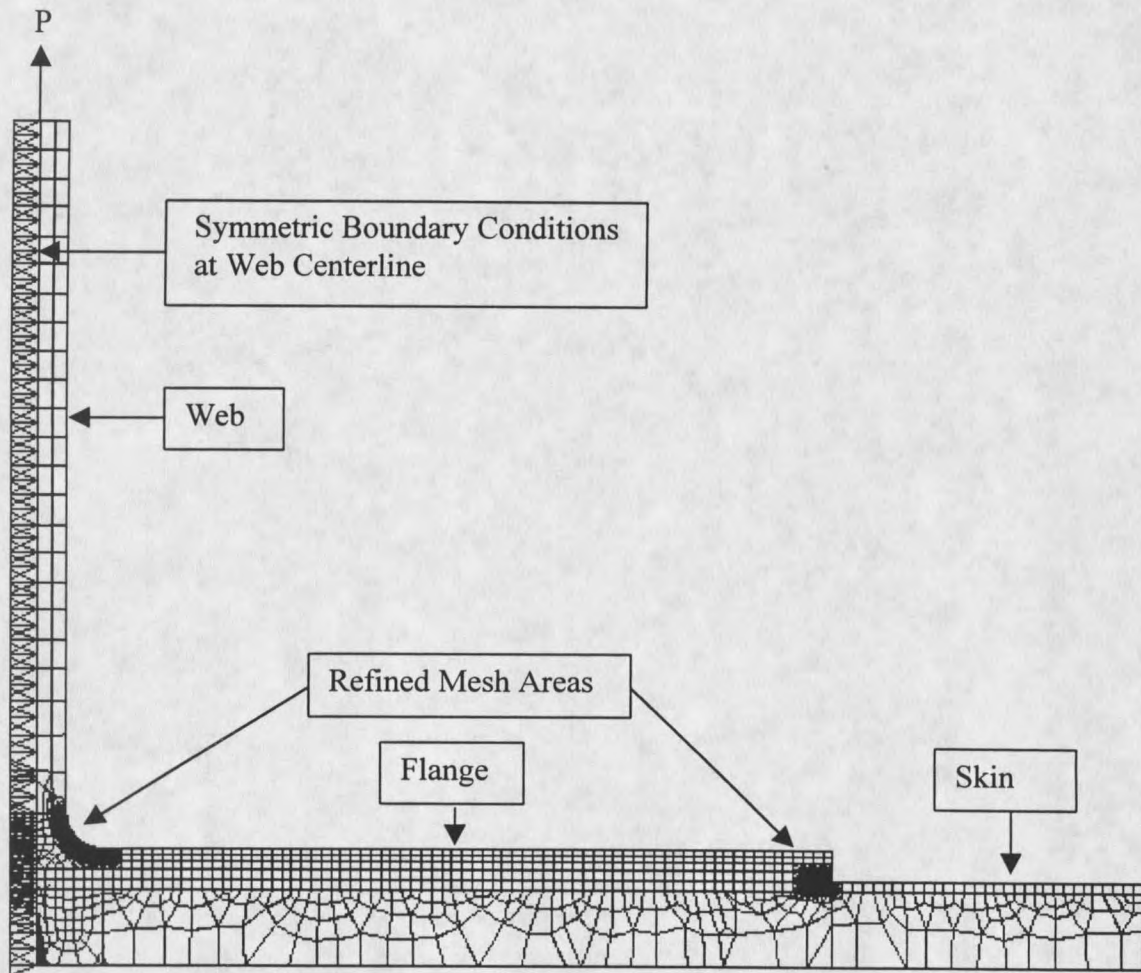


Figure 21. Finite element mesh for thin-flanged stiffener tests.

do mesh size analysis. The flange tip area was highly refined (Fig. 22) to investigate damage onset with very small initial crack lengths.

The thin flange models had the plies modeled individually in the flange section as well as in the top ply of the skin. The flange tip and bend region had highly refined meshes (Fig. 21) for analyzing strain energy release rates and strain values for use in

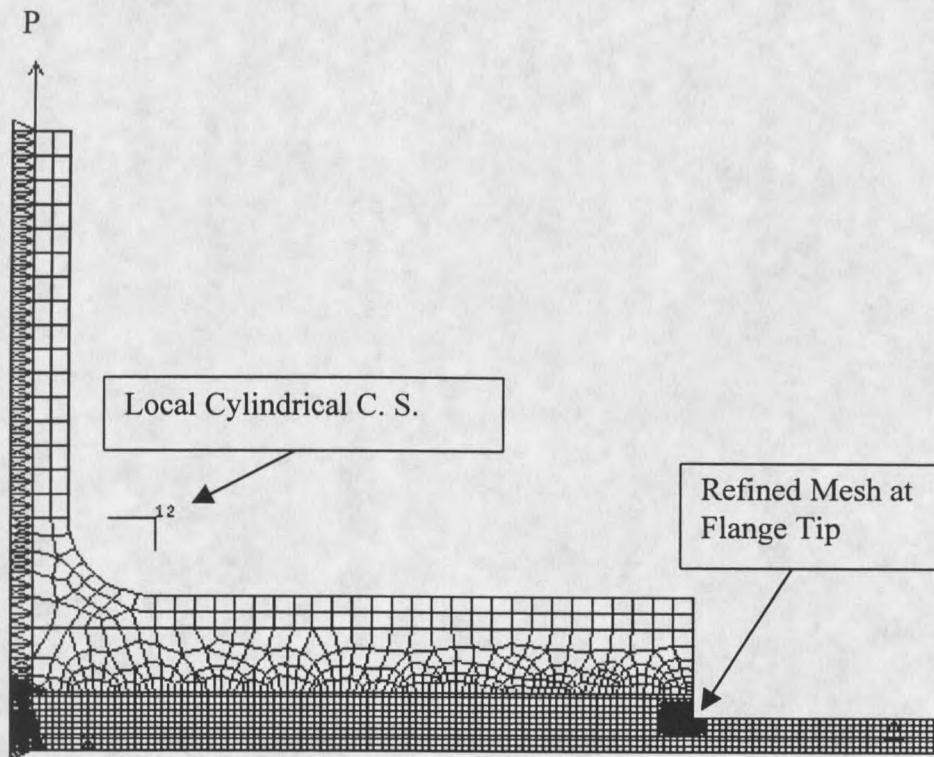


Figure 22. Finite element mesh for thick-flanged stiffener tests.

damage onset predictions.

In both model types, larger areas were created away from the crack interface that utilized smeared composite properties derived from classical laminated plate theory. This made the models more efficient while still capturing key information in the areas of interest. This was permissible since the through-thickness stresses and stress gradients were expected to decrease away from the flange tip and bend region areas as observed by Minguet et al. [8]. The delamination interface was created by modeling the stiffener and flange as separate entities, and then using multi-point constraints at the coincident nodes

to tie the skin-stiffener together. In this way, any length of delamination could be modeled by adding or deleting coupled nodal pairs.

A local cylindrical coordinate system was created at the center of the radius of curvature of the web-flange fillet area for both stiffener types. This was necessary to make the ply material properties follow the curved contour. The element coordinate systems in the bend are defined to match the local system in this area. In order to ensure that the element material properties were properly attributed, an FEA solution with this local system was benchmarked against a closed-form solution for a curved member under flexural loading.

The analysis of the specimens with FEA involved using models without a crack to simulate initial behavior in the undamaged state, and then introducing a delamination to perform fracture mechanics analysis on the debonded configuration. The intact models were checked for regions of high stress gradients or singular zones at the experimentally observed initial damage load to show which areas were prone to initial damage and delamination growth. Next, delaminations were modeled at these areas, and G values were calculated. Using the procedure outlined in Chapter 2 and Appendix A for mixed-mode growth, the load to propagate a delamination at the interface was calculated.

One problem that designers encounter with skin-stiffener intersections is trying to apply strength-based failure criteria in regions where a stress singularity exists, such as at the flange tip region. In this region, the peel stress becomes unbounded at the flange termination, as previously discussed. Moreover, as the element size is refined, the stress keeps increasing with every refinement [3], making standard stress-based analysis

useless. One approach is the “Whitney-Nuismer average stress criterion” [37], which says that fracture will occur when the average stress in a region over some characteristic distance (a_0) reaches the peel strength of the material (σ_0). The formula for the integral average stress used to calculate a_0 is presented in Equation (7).

$$\sigma_0 = \sigma_{a_0} = \frac{1}{a_0} \int_0^{a_0} \sigma_y(x, 0) dx \quad (7)$$

Where σ_0 = the ultimate peel strength of the material.

σ_{a_0} = the average stress over distance a_0

σ_y = the peel stress distribution in the material

The material characteristic distance must be found experimentally for each material system [11, 37].

A method based on fracture mechanics was developed in this study to predict delamination onset loads. This method reduces the crack length to a very small initial value (a_i) and compares the FEA output G values to the interlaminar fracture toughness data. The load calculated to propagate this very small crack is assumed to approach the load to initiate a crack in the structure from the undamaged state. This method was applied to the singularity zone at the flange tips in the stiffener specimens to predict fracture onset.

After successfully using this technique in the present study, it was discovered that Martin [3] had previously used a similar method for predicting fracture initiation with

good results. However, as the crack length approached zero ($a < 0.25$ mm), the FEA results for G_I and G_{II} began to diverge. The results were stable and quite converged, however, at crack lengths between 0.25 mm and 0.4 mm. He concluded that as the crack became very small, the assumption that (a/da) was large was violated, and poor results were obtained.

Martin did not report any proposed range of ratios for (a/da) to use with this method of predicting fracture onset. But, based upon Martin's results and the previous recommendation [27] for (a/da) ratios with FEA of 50 to 200, it appears that this method should provide satisfactory results if the (a/da) ratio is large enough, and the modeled crack length is below 0.4 mm. The trade-off is between making the crack small enough that fracture onset is modeled properly, while maintaining a high enough (a/da) ratio that the assumptions of the crack closure integral are not violated. These parameters are investigated further in the Numerical Results section of Chapter 6.

CHAPTER 5

EXPERIMENTAL RESULTS AND DISCUSSION

This chapter summarizes the results of the experimental test methods for the DCB, ENF, and substructure test specimens. Full results are presented in Appendix B. The DCB and ENF specimens were used to examine interlaminar fracture toughness for basic material property characterization. Results are given for the delamination resistance of common interface lay-ups. The substructure test specimen results are then presented for variations in manufacturing method, matrix material, ply orientation, stiffener geometry, and applied loading.

DCB Specimens

DCB Mode I fracture toughness (G_{Ic}) tests were conducted on specimens varying in delamination interface ply orientation and delamination length. Cracks were propagated between (+45/-45) and (0/0) ply orientations to investigate toughness changes with different lay-ups. In addition, G_{Ic} values calculated with the Area and MBT methods (see Chapter 2) were compared for identical cases.

(+45/-45) Interface

The [(+45/-45)]₁₀ specimens showed both higher values of G_{Ic} and larger discrepancies in values calculated from the Area and MBT methods when compared with

the $[(0)]_{10}$ specimens (Figs. 23 and 24 and Table 6). The horizontal axis (crack extension (a^*)) is the crack length beyond the Teflon starter film insert. The initiation value right from the starter film tip is $a^* = 0$. The increase in G_{Ic} with increasing crack

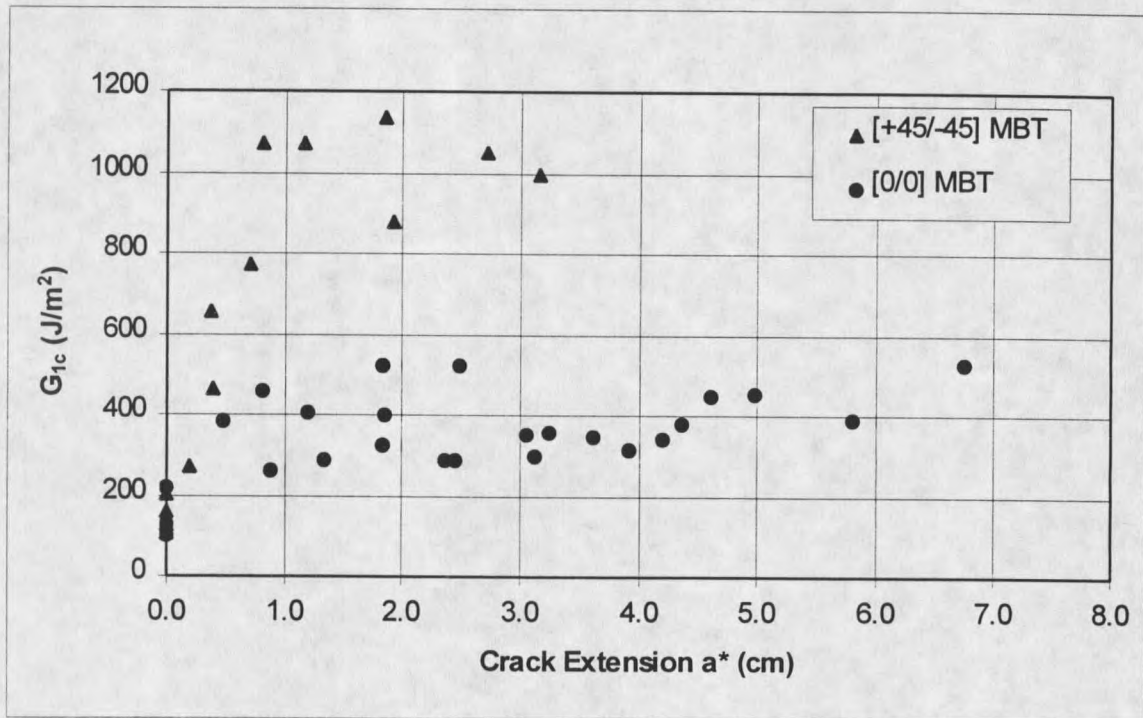


Figure 23. R-curve for (+45/-45) and (0/0) specimens calculated with the MBT method.

extension and the fact that the Area method produced consistently higher values for G_{Ic} is shown in Figure 24. G_{Ic} values for the MBT method increased from an average initiation value (at $a^*=0$) of $140 (\pm 41) \text{ J/m}^2$ to an average value of $1028 (\pm 97) \text{ J/m}^2$ once the crack had grown beyond 1 cm in length. For use in FEA predictive analysis, a linear curve fit was applied to the portion of the MBT R-curve between 0 and 1 cm. For crack lengths greater than 1 cm, a horizontal line equal to the average of the data points in that range (1028 J/m^2) was used.

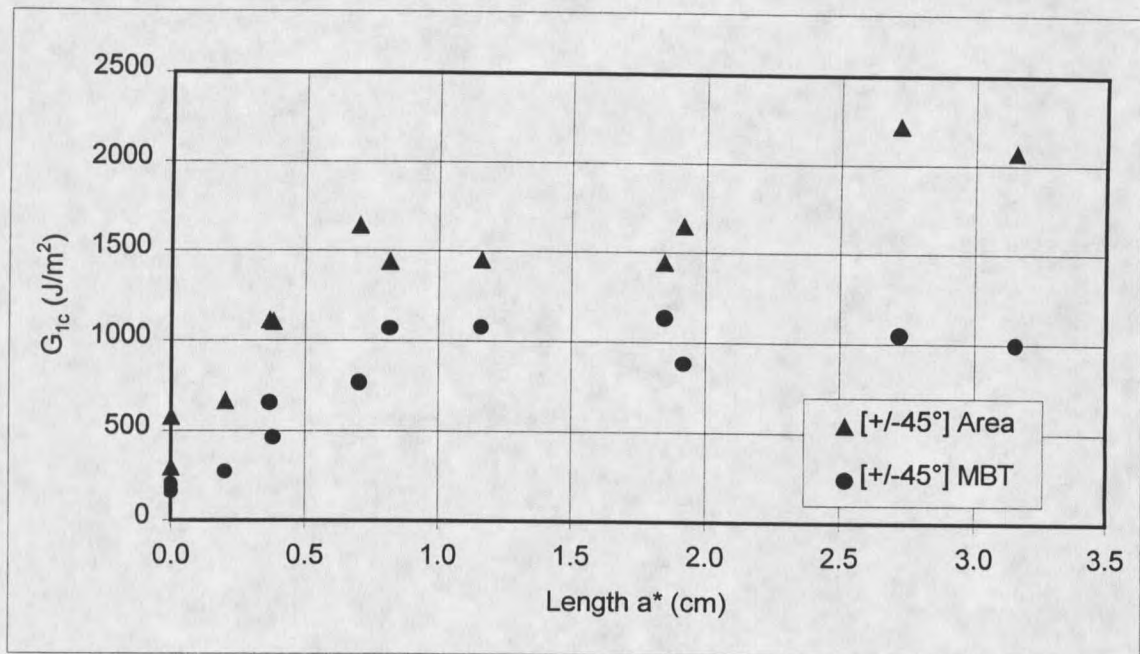


Figure 24. R-curve for (+45/-45) specimens calculated with the Area and MBT methods.

Table 6. DCB test results summary.

DCB Lay-up	# specimens	G _{Ic} (J/m ²) Initiation	Std. Dev.	# data points	G _{Ic} (J/m ²) (a*>1.0 cm)	Std. Dev.	# data points
[(0)] ₁₀	5	138	56	4	379	81	19
[(+45/-45)] ₁₀	2	140	41	5	1028	97	5

For the Area method, G_{Ic} values were $435 (\pm 199) \text{ J/m}^2$ at small crack lengths, roughly 1500 J/m^2 at a crack length of 1 cm, and over 2000 J/m^2 at a length of 3 cm (Fig. 24). It should be noted that the Area method does not give a value for G_{Ic} at initiation from the starter film since the crack is extended some finite amount during the test. However, the MBT method does provide a value for G_{Ic} at initiation from the film ($a^*=0$).

Specimens with a $[(0)_2/(+45/-45)/(+45/-45)/(0)_2]$ lay-up were also tested. These specimens provided good data points for the initiation value from the starter film tip.

However, the crack did not stay at the (+45/-45) interface at the mid-plane during subsequent propagation. Instead, it traveled to the interface between a (0) degree fabric ply and a (+45) degree ply. This behavior is consistent with the lower fracture toughness for a (0/+45) interface lay-up as reported by Scott [16] for an identical polyester/E-glass material. The increase in G_{Ic} with crack length is proposed to occur due to development of fiber bridging, increased tow debonding, and increasing crack path tortuosity. All three factors were observed during the test or upon viewing the post-fracture surfaces for these specimens (Fig. 25).

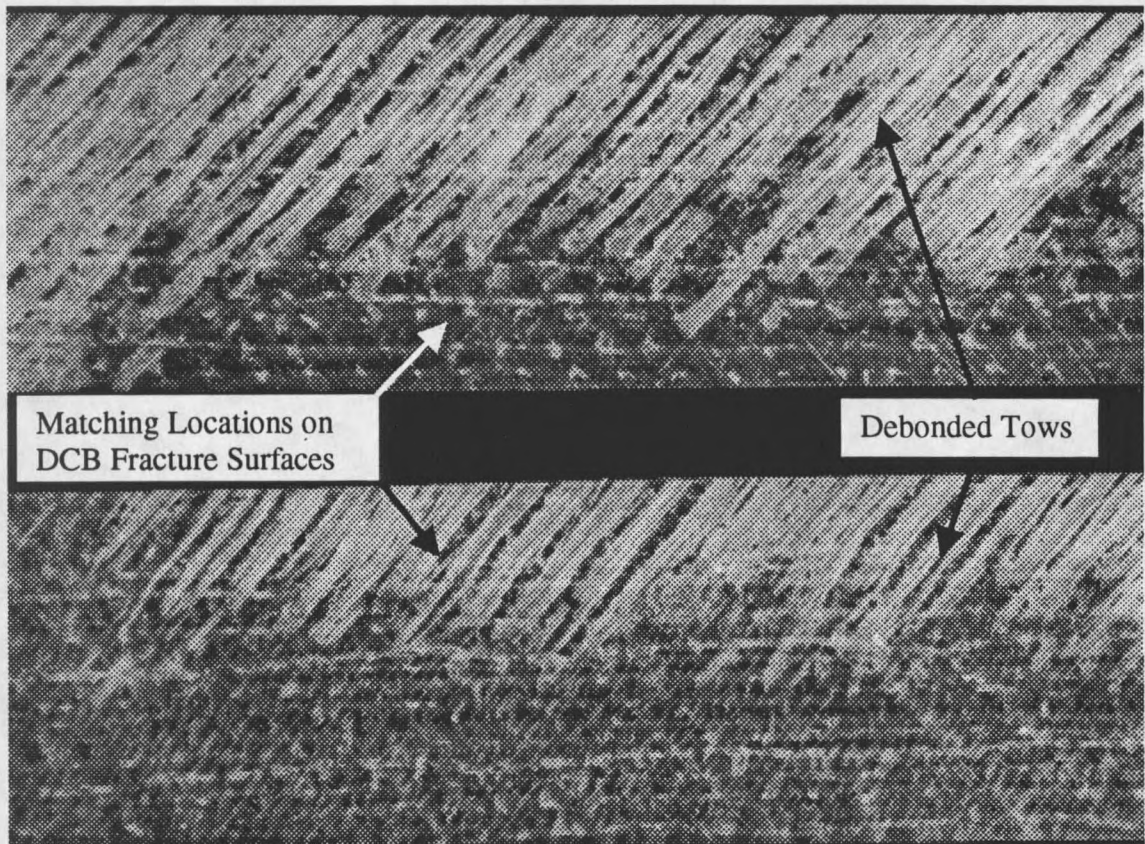


Figure 25. Fracture surface for [(+45/-45)]₁₀ DCB specimen.

Alif et al. [17] observed tow debonding in the fabric layers above and below the crack interface for a woven fabric carbon/epoxy material. They reported that a single tow debond increased G_{Ic} results by 50 J/m^2 . This conclusion was based upon the increase in G_{Ic} for crack lengths corresponding to a single observed tow debond. This tow debonding effectively created a larger fracture process zone, as well as multiple crack paths. The multiple cracks require more energy to drive the delamination. With tow debonding, the crack actually grows simultaneously at the mid-plane fracture surface and the tow-matrix interface one ply thickness away from the mid-plane. This behavior is evident by viewing the $[(+45/-45)]_{10}$ DCB fracture surface (Fig. 25) with the naked eye. Each surface had large regions of debonded tows, which produced a white-colored, heavily delaminated surface. In addition, the debonded surface usually occurred on only one of the fracture surfaces at a particular time (Fig. 25). The crack propagation did not debond the tows on both interface plies at the same point simultaneously.

Fiber bridging has been reported to be a key toughening mechanism in fibrous composites. ASTM standard D 5528 [24] reports that for pre-preg type composites “the principal reason for the observed resistance to delamination [R-curve] is the development of fiber bridging.” It is also believed that the stitching of the DB120 (+45/-45) fabric may increase G_{Ic} during the tow debonding and bridging processes because the stitching acts as through-thickness reinforcement.

The proposed reason for the difference in G_{Ic} values between the Area and MBT methods lies primarily in the tortuous crack path during propagation. Crack path tortuosity was cited by Alif et al. [17] as a factor in the increased values of G_{Ic} for woven

carbon/epoxy DCB specimens. They cited path tortuosity as the explanation for observed R-curve behavior as the convoluted path developed beyond the insert film. This was the only explanation for the toughening mechanism since no bridging was observed in the tightly woven carbon fabric/epoxy specimens. The Area method takes into account the energy dissipated during a crack advance between two points on the mid-plane of the DCB specimen. The crack path is assumed to be straight between these two points. While the area enclosed by the loading/unloading curve is the correct amount of energy dissipated during crack growth, the path is definitely not self-similar (straight) for the (+45/-45) interface specimens. In reality, the crack is much more tortuous, and therefore longer, than the assumed straight path. Thus, dividing by the shorter straight path length will actually produce a higher value for G_{Ic} with the Area method, when compared to the MBT method. The MBT method does not suffer from this problem, since it only uses the initial crack length in the calculation, and not the crack extension during the test.

(0/0) Interface

The values for G_{Ic} from the unidirectional DCB tests were much lower in magnitude and displayed much better agreement between the Area and MBT tests. A graph of G_{Ic} vs. crack extension for the MBT and Area methods is shown in Figure 26 for the 0^0 unidirectional specimens.

The average initiation value for the (0/0) specimens was $138 (\pm 56) \text{ J/m}^2$. This is nearly identical to the result for the (+45/-45) interface, which was $140 (\pm 41)$. The results should be very close since the crack is growing into the matrix-rich region ahead of the insert film [24], and in both cases the matrix material is the same. The increase in

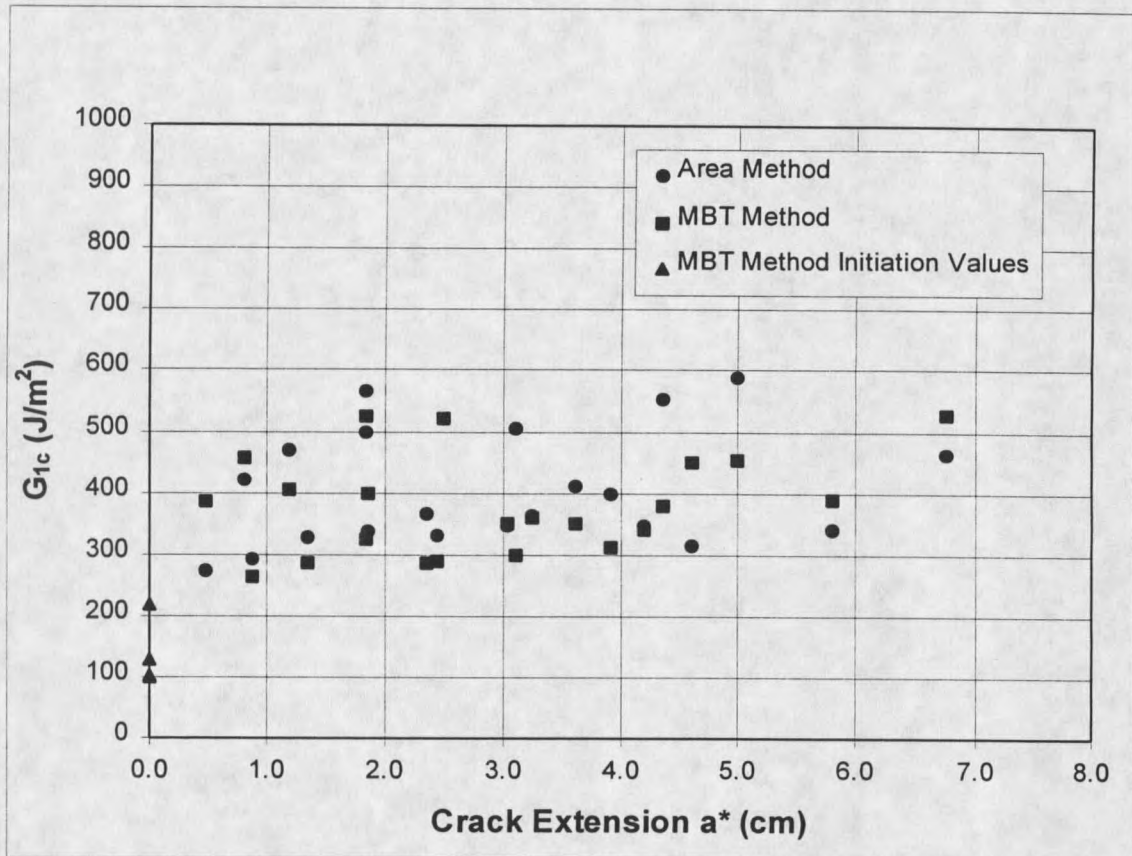


Figure 26. R-curve for (0/0) DCB specimens calculated with the Area and MBT methods.

G_{1c} with crack extension is much lower for the (0) degree specimens, when compared with the (+45/-45) interface (Fig. 23). When the data points (excluding initiation values) for the [(0)]₁₀ specimens were averaged, the Area method mean was 411 (\pm 94) J/m², while the MBT method averaged 379 (\pm 81) J/m². Scott [16] calculated Mode I values of 490 (\pm 30) J/m² for this unidirectional polyester/E-glass material using a compliance method formula.

The lower toughness for the [(0)]₁₀ specimens after crack growth compared with the (+45/-45) coupons is explainable with the following observations. The 0° specimens

exhibited no fiber bridging and the fracture surface was rather clean in appearance (Fig. 27), with very little tow debonding present. The surface topology also followed the

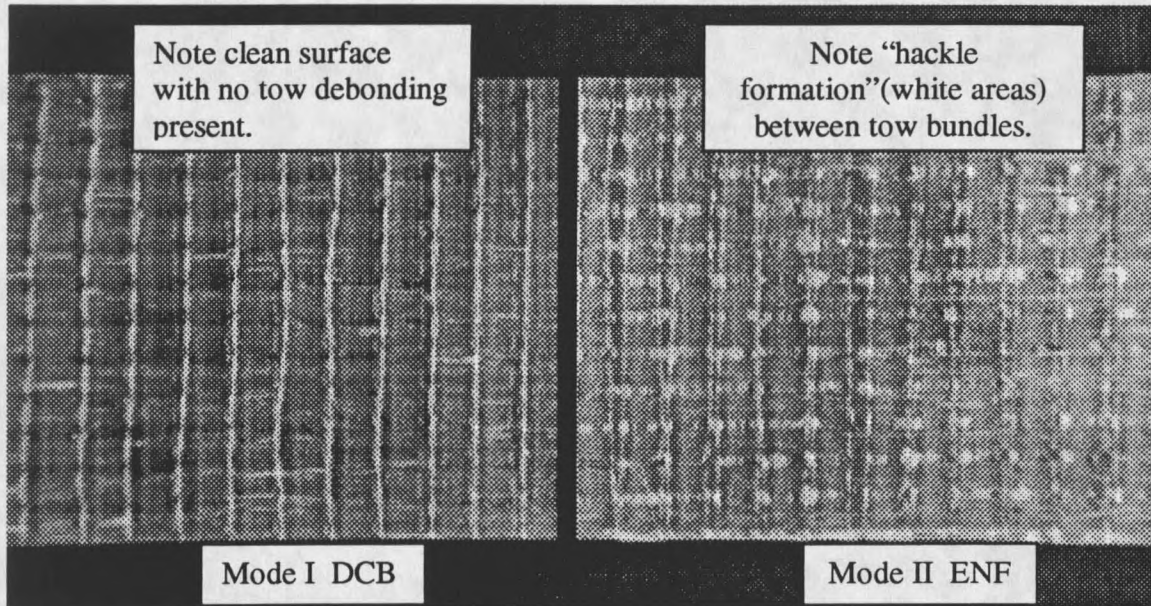


Figure 27. Mode I and II fracture surfaces for $[(0)]_{10}$ DCB and ENF specimens.

fabric surface fairly well. There was an observed waviness in the transverse direction, as the tow bundle surface contours were followed, but the growth was self-similar along the length. This may explain the increase to a relatively stable G_{Ic} soon after initiation. It is possible that as the crack grows from the pure matrix region at the insert film tip into the inter-ply area, the transverse path waviness causes the increase in G_{Ic} values, since there was no fiber bridging or tow debonding present in the specimens. The slight transverse waviness might cause the small increase in the Area method results over the MBT method values. Again, this may be due to the smaller value used for crack extension with the Area method calculation because of the assumed straight crack propagation. These

observations help explain the overall lack of crack growth resistance for the (0/0) interface lay-up and the better agreement between the Area and MBT method results.

The DCB results for the (+45/-45) and (0) degree interfaces indicate that there is a definite toughness change with ply interface orientation. This would indicate that designers and manufacturers should avoid (0/0) interfaces with D155 type fabrics at delamination prone areas. However, it should also be emphasized that the increased toughness for the (+45/-45) interface came only after significant crack growth ($a > 1.0$ cm) had occurred. The initiation values for G_{Ic} were nearly identical for both lay-ups. This means that designers should not rely on this toughening behavior, since significant damage is necessary to achieve it. A better approach would be to design against delamination onset and utilize the G_{Ic} values at initiation for predictive analysis. This will ensure conservative estimates for damage onset loads. In addition, it is not known if the same toughening mechanisms occur during fatigue crack growth for these material systems.

ENF Specimens

The results for the ENF specimens generally showed that Mode II values for G_c were much higher than the Mode I results. This is consistent with results from previous investigators [16, 17, 19, 25, 26, 33]. In addition, there was a dependence on ply orientation as observed in the Mode I tests.

(+45/-45) Interface

The initial ENF tests performed with the $[(+45/-45)]_{10}$ specimens were too compliant for proper testing. The specimens bent until transverse tension failure was noted on the outer +45 layer. This was corrected by bonding unidirectional material on the outside surfaces to increase the bending stiffness of the specimens. This greatly increased the stiffness and allowed the specimens to load up enough to propagate a crack in shear at the mid-plane. It also ensured the accuracy of the analysis procedures that are based upon linear beam theory. Due to the nature of the crack advancement, only one value for G_{IIc} could be determined for each specimen. Once the critical load was reached, the crack grew in an unstable manner for a number of centimeters, creating a loud “snapping” noise due to the large energy release. A typical load vs. displacement curve for an ENF test was shown in Figure 14. The onset of non-linearity was used as the critical load. This ensures the most conservative value for G_{IIc} for later use in predictive analysis.

The results for the ENF tests are shown in Table 7. One can see the relatively

Table 7. ENF test results summary.

ENF Layup	G_{IIc} (J/m^2) Initiation	Std. Dev.	# data points
$[(0)]_{10}$	1293	259	4
$[(+45/-45)]_{10}$	2001	286	4

large toughness value for the (+45/-45) interface of 2001 (± 286) J/m^2 . Scott [14] reported Mode II values for this material with growth along a (+45/0) interface of 2270 (± 530) J/m^2 .

(0/0) Interface.

The unidirectional ENF specimens displayed a much lower Mode II toughness compared to the (+45/-45) specimens. The results, presented in Table 7, show an average value of 1293 (± 259) J/m² for the unidirectional tests. Scott [16] reported Mode II values for this material, with growth along a (0/0) interface, of 1430 (± 350) J/m². "Hackles" [17] were clearly visible to the naked eye on the fracture surface of the Mode II test specimens (Fig. 27) in the resin-rich area between the fiber tows. Bradley [19] reports this hackle formation is due to the formation of many "sigmoidal shaped microcracks" in the matrix region ahead of the crack tip. He also reports that this extended process zone is most likely the reason for the increase in Mode II fracture toughness values over Mode I values in polymer matrix composites.

Thin-Flanged Stiffeners

Tensile Static Loading

Co-Cured vs. Secondarily Bonded. There are two manufacturing methods of interest for producing wind turbine blades. The first is creating the entire blade with RTM in one piece (co-cured). The second is making separate skins and stiffeners, and bonding the pieces together (secondarily bonded). The one-piece approach has the obvious advantage of reducing secondary manufacturing operations, thereby reducing production costs. In addition to cost considerations, it is of interest to investigate the relative structural performance of the two manufacturing methods. In order to analyze structural performance, a series of tests utilizing the thin-flanged T specimens were

performed. This section presents the results of the tests. A description of the specimen geometry and manufacturing was presented in Chapter 3. A typical load-displacement curve was presented in Figure 18.

The first series of tests compared the one-piece T specimens with the thin bond-line (0.15 mm adhesive layer) two-piece specimens. The adhesive used in these tests was the Hysol EA 9309. Upon loading, the stiffeners developed cracks at the web/flange fillet area. The initial damage was visible (Fig. 28) as transverse cracking in the bend surface (+45/-45) layer (1), whitening underneath the surface plies (2), and transverse

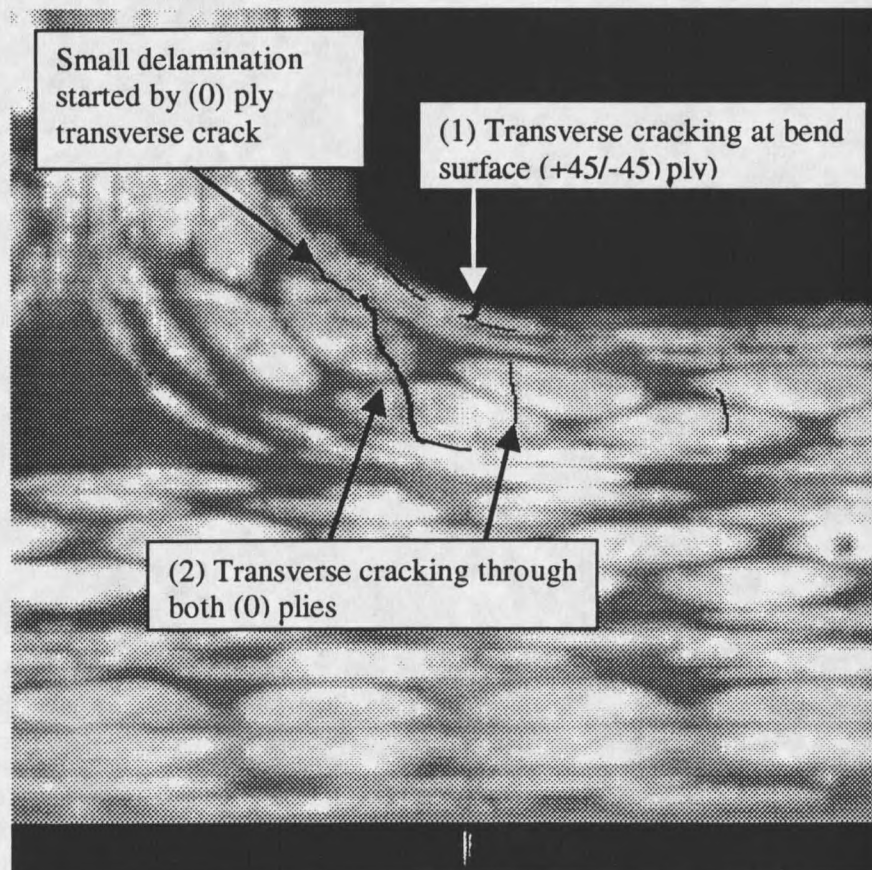


Figure 28. Initial damage at web/flange fillet area in co-cured thin-flanged stiffener specimens.

cracks through both (0) degree plies in the bend (2). Actual cracks in Figures 28 and 29 were traced over with a computer drawing program to enhance visibility in the photographs. Many tests were stopped immediately after initial cracking was audibly detected to discern the failure sequence. A black dye marker was rubbed on the bend surface and specimen edges and wiped off to better observe any crack formation. The dye clearly showed transverse cracking on the bend region surface, as well as transverse cracking in the two (0) degree plies within the bend region (Fig. 28). In addition, the transverse cracks seemed to initiate the slight delaminations between the (0) degree ply and the surface (+45/-45) ply. It was concluded that the transverse cracks happened first because some of the tests exhibited the transverse failure without the small delaminations being present. It is possible that the small delaminations were due to dynamic effects of the fast fracture in the (0) degree plies. Based upon these observations, it was impossible to determine if the surface (+45/-45) crack or the (0) degree transverse crack occurred first.

After initial damage, other cracks formed in the bend region (Fig. 29), followed by the horizontal delamination (3), which formed within the uppermost skin (+45/-45) fabric ply and grew all the way to the flange tip region. A vertical delamination (4) also formed at the web centerline and grew upward toward the loading grips. This damage sequence was the same for all co-cured and thin bond-line specimens.

The results for initial damage and maximum pull-off load (Fig. 18) showed essentially no change between the co-cured and secondary bonded specimens (Table 8). The one-piece specimens had an average initial damage load of 85.5 (\pm 15.3) N/cm,

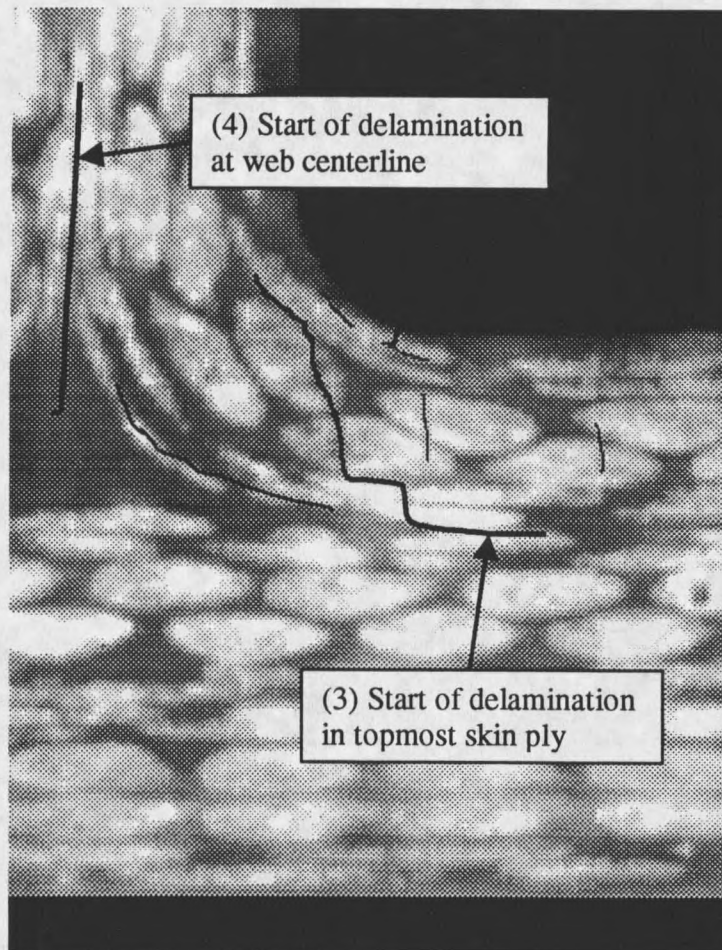


Figure 29. Formation of delaminations at bend region in thin-flanged stiffeners.

while the bonded stiffeners had an average initial damage load of $87.7 (\pm 7.6)$ N/cm. The average maximum loads reached during the tests were $132.7 (\pm 3.9)$ and $132.3 (\pm 9.2)$ N/cm for the one and two-piece specimens, respectively.

A strain gauge was mounted on the bottom skin surface to measure the transverse strain during the pull-off tests. At an applied load of 66.7 N/cm, the strain across the specimen width was 0.00028 cm/cm. Linearly scaling this strain up to the initial damage load of 85.5 N/cm would give a strain at damage of 0.000359 cm/cm or 0.0359 percent.

Table 8. Test results for bonded and co-cured thin-flanged stiffeners.

Thin Flanged Stiffeners					
Specimen Type	Initial Damage Load (N/cm)	Std. Dev.	Maximum Load (N/cm)	Std. Dev.	# data points
Co-cured	85.5	15.3	132.7	3.9	11
Secondary Bonded (0.15 mm adhesive)	87.7	7.6	132.3	9.2	12

This strain is quite low, and while non-zero, it seems to justify a plane strain rather than plane stress assumption for the FEA models.

Some observations about the specimens and the delamination surface help to explain these results. As reported in Chapter 2, increasing the skin bending stiffness has been shown to increase the pull-off load [15]. This is because higher bending stiffness translates into lower out-of-plane deflection, and lower through-thickness stresses and strains in critical areas. In the current tests skin bending stiffness remained constant. In addition, the overall bending stiffness of the specimens does not change appreciably with the addition of such a thin bond-line. It was calculated that the bending stiffness (D_{11} term) for the flange and skin added together only increased from 221.7 N-m to 236.9 N-m with the addition of the 0.15 mm bond-line. Also, the delamination was observed to grow within the topmost skin (+45/-45) ply underneath the adhesive layer. The crack never grew within the adhesive itself. This behavior was also observed by Minguet et al. [15] in bonded stiffener pull-off tests. They concluded that this was reasonable due to the increased toughness of the adhesive compared with the matrix material. This appears to be the case with the polyester/E-glass system as well. The maximum pull-off load occurred once the delamination was beyond the web/flange fillet area and within the top-

most skin ply. Since the delamination was propagating in exactly the same location and material in both specimen types, the result of nearly identical maximum pull-off loads is understandable.

A cross-section of a bonded skin-stiffener detail region from a commercial wind turbine blade is shown in Figure 30. The stiffener is in the form of a C-channel for this

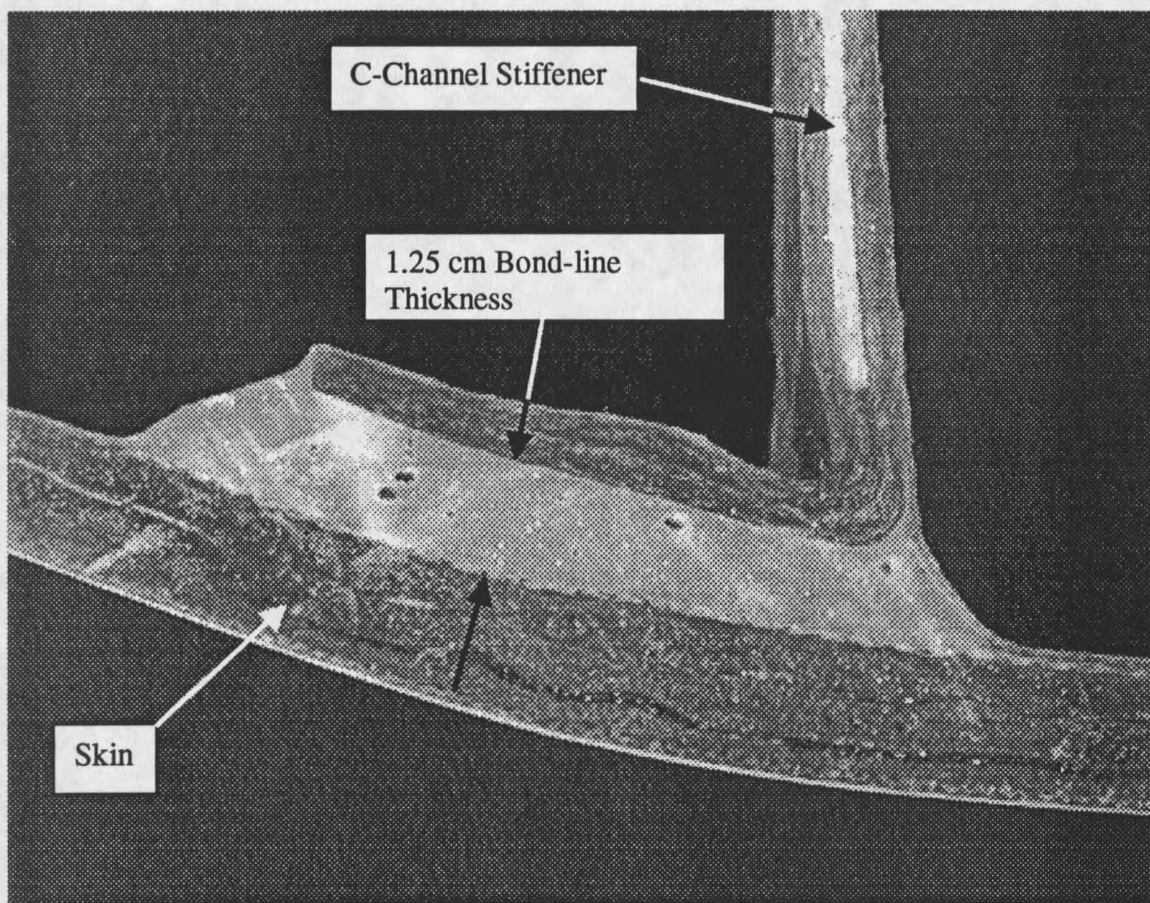


Figure 30. Cross-section of a thick bond-line on a commercial wind turbine blade

blade. This specimen had a measured bond-line thickness greater than 1.25 cm. From this observation, it was clear that not all commercial blades have precision bond-lines

made in a laboratory environment. As a result, the bond-line thickness effects were further explored.

In order to investigate bond-line thickness, specimens were made with an adhesive layer thickness ranging from the previously tested 0.15 mm to greater than 6.0 mm. In addition, a few specimens were bonded with a commercially used methacrylate adhesive (Plexus A025). This adhesive was chosen since it represents an easy to use, caulking-gun applied product that is gaining widespread use in the fiberglass manufacturing industry [36].

The results of the bond-line thickness tests are presented in Figure 31. It is evident from the graph that as bond thickness increases, both initial and maximum loads

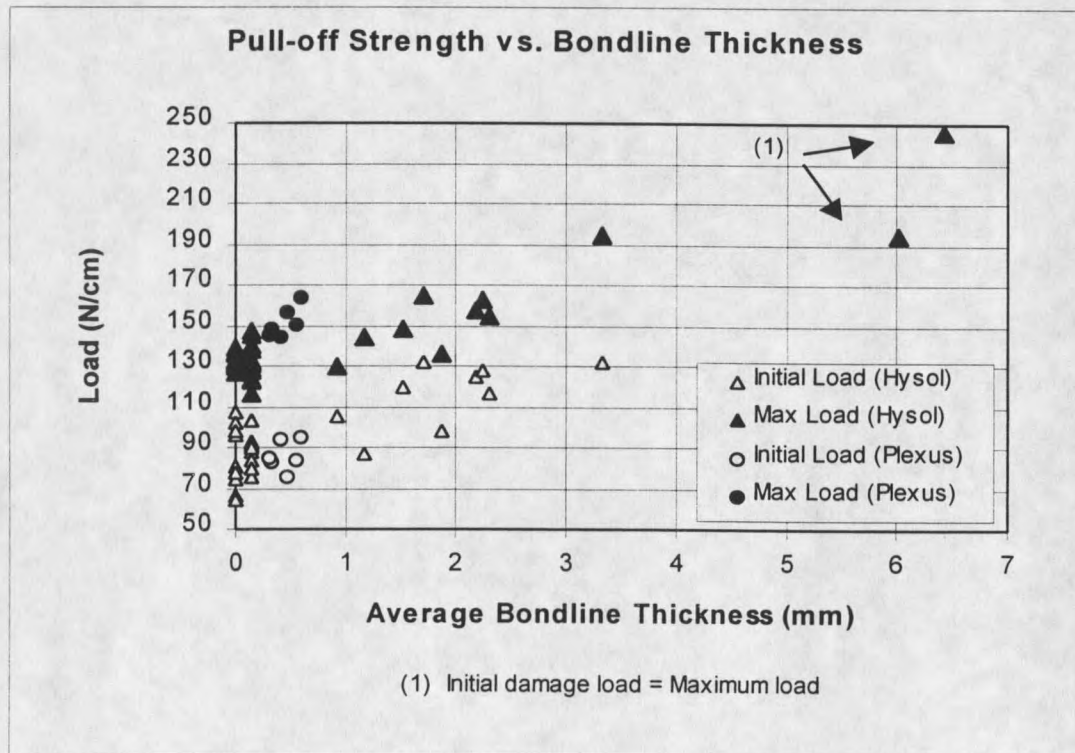


Figure 31. Pull-off strength vs. bond-line thickness for thin-flanged specimens.

increase. This is in agreement with the previous discussion about the influence of bending stiffness on pull-off load. As bond thickness continues to increase, the bond distance separates the skin and flange. As a result, moment of inertia and bending stiffness increase. At a bond thickness greater than 4 mm, a transition in failure location occurred. For the specimens with approximately 6 mm bond thickness, the initial failure location was at the flange tip, rather than the web fillet radius, as in all previous specimens. The transition to a flange tip failure is consistent with the fact that the peel stress at the flange tip increases as the geometric mismatch between the skin and flange increases [5-7, 11]. No damage was observed at the web fillet radius area for the 6 mm bond specimens. The initial damage and maximum loads were coincident for these specimens. These results indicate that little or no stable crack growth would occur for this type of geometry, since the initial damage load was also the maximum load reached.

The results for the Plexus methacrylate indicate that it performs as well as the Hysol in terms of initial damage load, and possibly better for the maximum pull-off load (Fig. 31). The same damage progression was observed in the Plexus specimen group as in the Hysol bonded specimens.

Matrix Materials. Based upon the previous results, it appeared that the brittle polyester matrix was a limiting factor in the delamination resistance of the stiffeners. Therefore, increasing the resin toughness should result in greater delamination resistance for these structures.

Two additional resin formulations were chosen for the specimens based upon their reputation for increased toughness and processability with the RTM method. The

resins selected were a polyester/PET blend (AOC PET P460-06), and polyurethane (Polytek Poly 15-D65). All specimens were manufactured as one-piece skin-stiffeners with a (+45/-45) interface lay-up.

The results for the matrix material comparison tests are presented in Table 9. The

Table 9. Thin-flanged stiffener pull-off tests with different matrix materials.

Thin-Flanged Stiffener Pull-off Tests with Different Matrix Materials					
Matrix Material	Initial Damage Load (N/cm)	Std. Dev.	Maximum Load (N/cm)	Std. Dev.	# data points
Polyester	85.5	15.3	132.7	3.9	11
Polyester/PET	120.3	9.1	165.0	6.0	4
Polyurethane	137.2	15.1	265.0	1.0	3

results show that using tougher resin formulations produces large increases in both initial damage and maximum pull-off loads. The initial damage load increased from 85.5 (\pm 15.3) N/cm for the polyester, to 120.3 (\pm 9.1) N/cm with the polyester/PET, and 137.2 (\pm 15.1) N/cm for the Polytek. The polyester/PET processed very well, with very good flow in the mold cavity, excellent wetout, and no observable voids. The polytek foamed considerably during cure, but also flowed well in the mold cavity during the RTM process. The maximum pull-off loads also increased with the new resin systems. The polyester/PET failed at 165.0 N/cm while the polyurethane reached 265.0 N/cm. The baseline polyester specimens failed at 132.7 N/cm.

The PET specimens displayed the same failure mode as the baseline polyester specimens. The load-displacement graph and a post-fracture photograph of a PET specimen are presented in Figures 32 and 33 respectively. The fracture appeared brittle

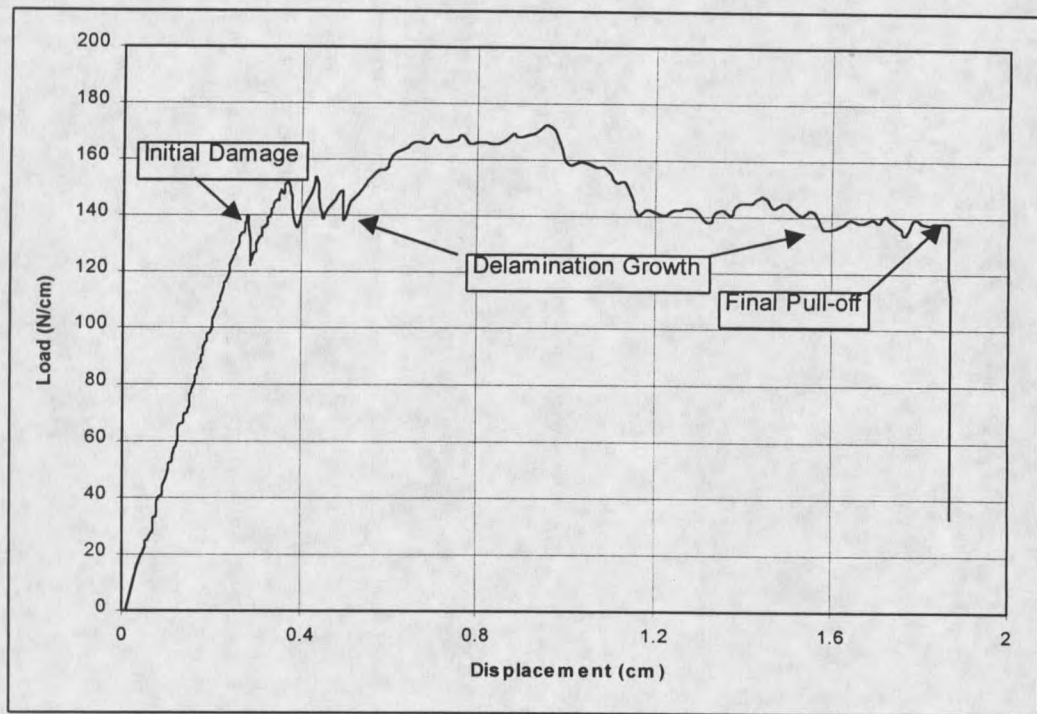


Figure 32. Typical load-displacement curve for polyester/PET stiffener specimen.

in nature with the damage initiating at the fillet radius bend surface, progressing downward to the skin interface, and then delaminating outward to the flange tip. The Polytek did not delaminate, indicating its very high toughness. The initial damage appeared as visible whitening in the bend region. The specimen bent excessively until final failure occurred as compressive fiber failure in the bottom skin ply. The load-displacement curve for a Polytek specimen is shown in Figure 34. Note the non-linear nature of the Polytek curve, which indicates that plastic yielding occurred, compared to the brittle behavior in the polyester and PET load-displacement curves.

Based upon the matrix material test results, it is evident that utilizing tougher resins in delamination-prone areas increases stiffener performance. This is because

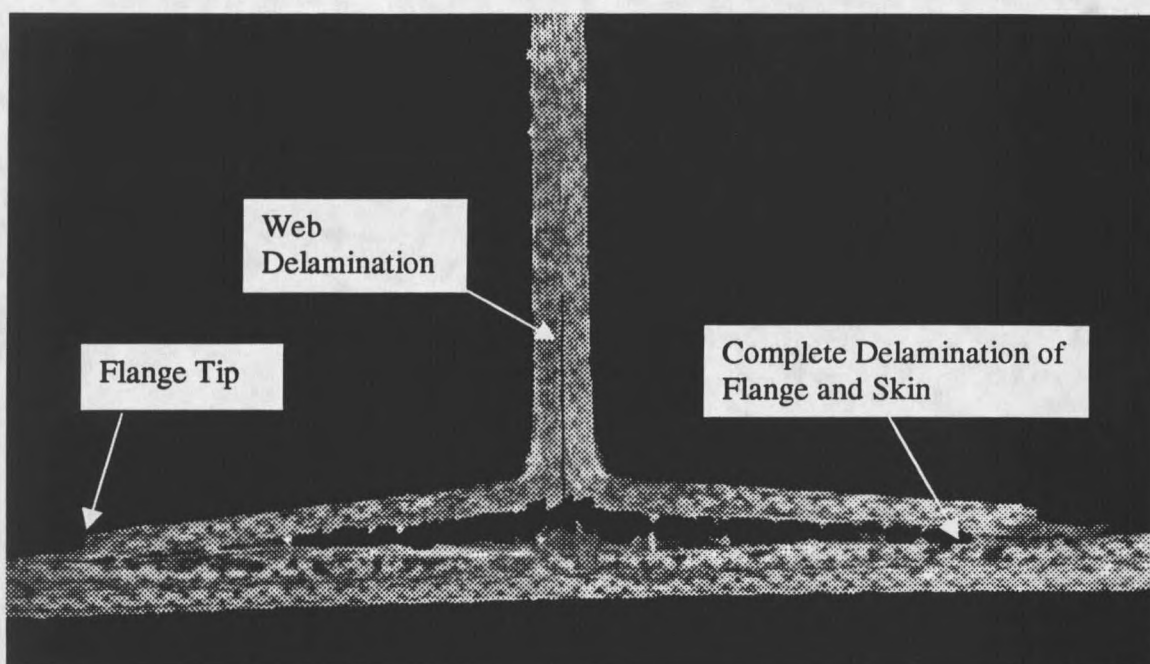


Figure 33. Photograph of polyester/PET stiffener with delaminations.

transverse strength and through-thickness properties in composites are dictated by the matrix material properties. The reinforcing fibers add little or no strength transverse to the fiber direction.

Compressive Static Loading

The thin-flanged specimens were tested in compression using the same test fixture. The load was applied by clamping the web and pushing downward on the specimen. The failure mode was completely different compared with the tensile tests. In this case, the initial failure mode was transverse tension in the bottom (+45/-45) degree skin ply, under the web at the specimen centerline (Fig. 35). Tension failures then progressed upward through the skin to the web/flange transition area. This was followed by final failure of the lower skin surface (+45/-45) degree ply by fiber tension

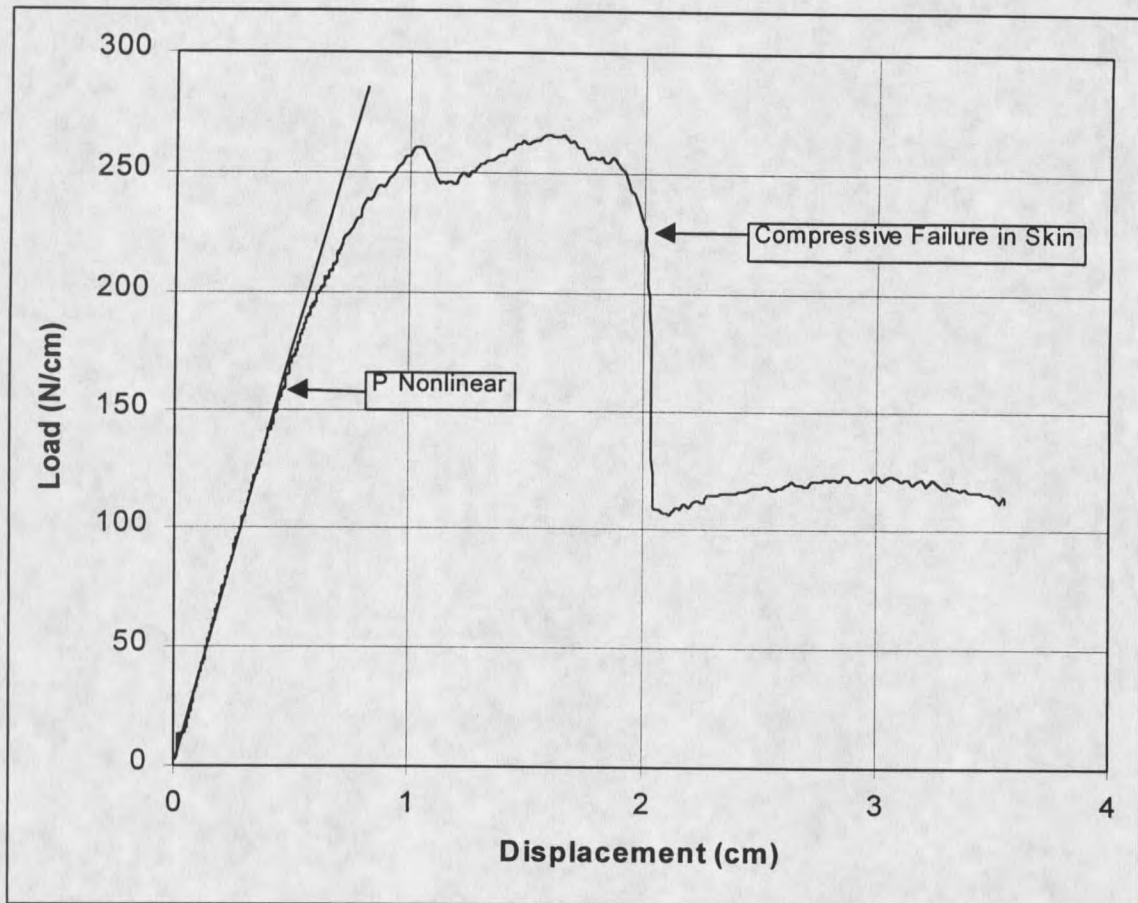


Figure 34. Typical load-displacement curve for polyurethane stiffener specimen.

failure (Fig. 35).

The T stiffener performed well in compression with no delaminations forming during the test. Damage in the web fillet radius area did not occur until after the final catastrophic fiber failure in the lower skin ply. The load at initial damage in the skin was $94.0 (\pm 2.2)$ N/cm. This is slightly higher than the load in the tensile test to form initial damage in the web fillet radius, which was $85.5 (\pm 15.3)$ N/cm. However, the maximum load reached in the compressive test was very high with an average value of $402.0 (\pm 4.2)$

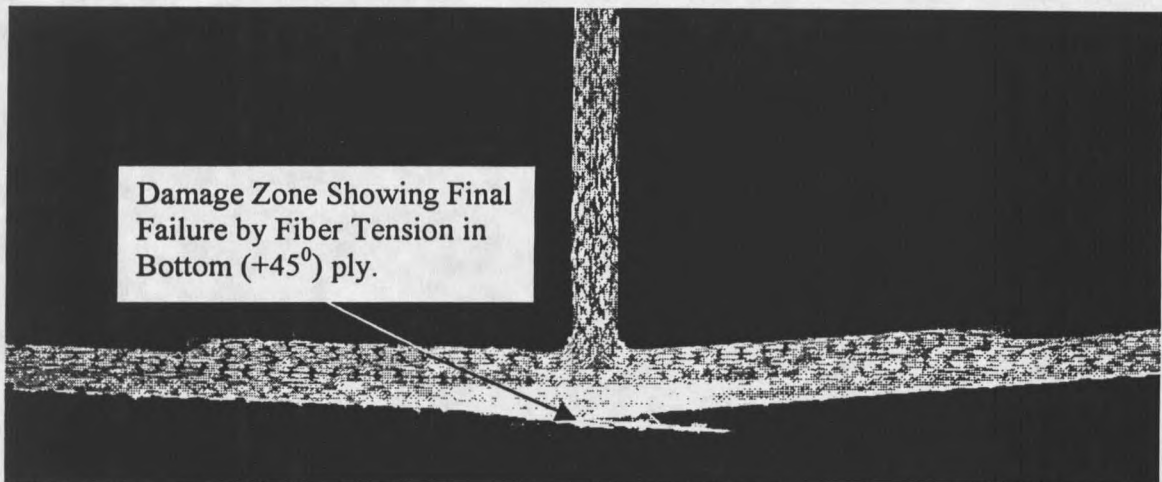


Figure 35. Photograph of thin-flanged stiffener after failure by compressive loading.

N/cm. This is because the final failure was by fiber tension in the bottom skin (+45/-45) ply. This is well above the maximum load for the tensile case, which was 132.7 (± 3.9) N/cm. The much lower maximum loads for the pull-off tests demonstrate the weakness of composite stiffeners during tensile loading and delamination-based failure. Thus, it should be a primary failure mode investigated during the stiffener design process by the stress analyst.

Another loading mode worth investigating is a force applied laterally to the web rather than the vertical loads used in the present study. This loading case may easily occur during localized skin buckling in wind turbine blades. Although the lateral loading case was not tested in the current study it has been performed on large stiffeners used in the ship hull industry by Phillips and Shenoj [38]. They applied a pull-off load to the web at 45 degrees to the vertical axis while restraining the stiffener at the flange area. This loading tended to “open” up one side of the stiffener while closing the other. Phillips and Shenoj reported that initial damage mode was a delamination of the

web/flange transition bend radius plies on the tension side caused by large interlaminar stresses. Based upon these results, and the findings of Kedward et. al [4], who found that increasing the bend radius lowered the interlaminar stresses in curved composite sections, it appears that damage onset should be delayed by utilizing the largest practical bend radius for a given stiffener design.

Thick-flanged Stiffeners

Tensile Static Loading

Co-cured thick-flanged specimens were tested in order to investigate a skin-stiffener configuration that exhibited a flange tip failure. It was believed that this flange configuration would exhibit a singular stress zone at the flange tip. This would aid in the development of analysis techniques for these regions with FEA methods. The stiffener was produced with a very thick-flange, formed by adding additional plies underneath the standard flange of the thin-flange design. Typical geometry and loading for a thick-flanged specimen was shown in Figure 16.

Skin thickness and skin-stiffener interface ply orientation were varied to examine the effect on initial damage load and delamination resistance of the specimens. The motive behind these lay-ups was to have two completely different specimen types for validating the FEA predictions. As was noted in the DCB and ENF result sections of Chapter 5, the toughness of the polyester/E-glass materials changed with variations in interface lay-up. The goals of the testing were to collect accurate data for load at damage

onset, and load vs. delamination length. Once this was established, the ANSYS predictions could be validated.

The configurations for the thin-skinned (T5000 series) and thick-skinned (T5200 series) specimens were previously listed in Table 3. In Table 10, the skin bending stiffness and initial damage loads are listed for both specimen types. The results of the static pull-off

Table 10. Initial damage loads for thick-flanged stiffener tests.

Thick-Flanged Pull-off Tests				
Specimen Type	Skin D_{11} (N-m)	Initial Damage Load (N/cm)	Std. Dev.	# data points
T 5000 Thin Skin	9.36	58.7	5.6	5
T 5200 Thick Skin	71.78	152.7	7.5	3

tests confirmed the trends of increasing initial damage loads with increasing skin bending stiffness. The T5000 specimens had an average initial damage load of 58.7 (\pm 5.6) N/cm, while the stiffer T5200 specimens showed an average initial fracture load of 152.7 (\pm 7.5) N/cm. The flange tip was always the location of fracture onset in both specimens. After initial fracture at the flange tip, the delamination progressed along the skin-stiffener interface plies toward the specimen centerline (Fig. 36). No damage was observed in the web-flange fillet area.

To gather data for load vs. delamination length, the specimens were loaded until the delamination was observed to propagate. The test was stopped, and the crack length on the left, right, front, and back sides of the specimen were measured using the same dye penetrant method used for the DCB tests. After each crack extension, the procedure was

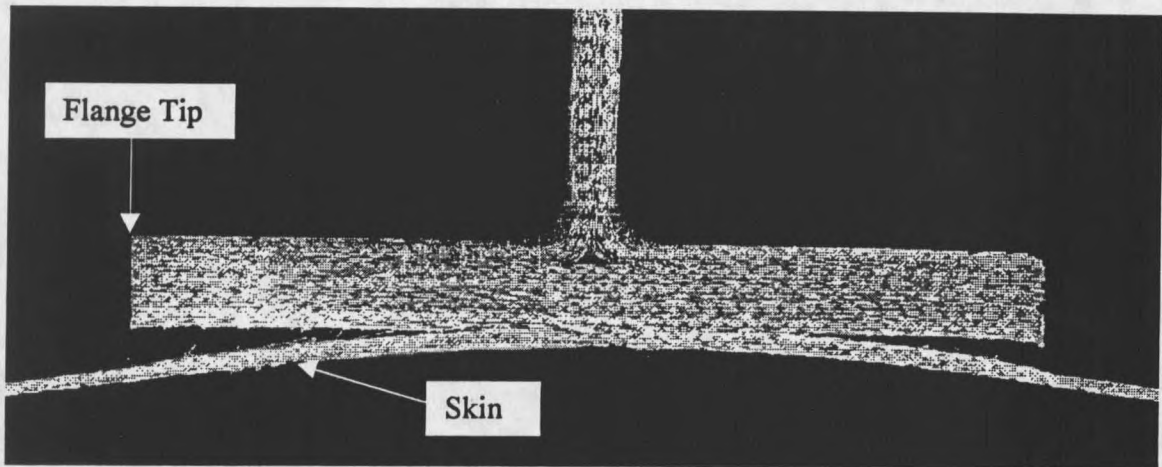


Figure 36. Photograph of flange tip delamination for thick-flanged stiffener specimens.

repeated. This allowed each test to start with a known value for crack length. The ensuing load vs. displacement plot was then used to find the load for propagation at that crack length. These values were later used as test cases for the FEA models.

A problem was encountered in most specimens as the delaminations grew beyond the initial crack onset at the flange tip. In most cases, the crack on one side, left or right, started to dominate, and would propagate farther toward the centerline at the same load case than the other crack. The crack fronts were quite constant across the specimen width on each side, however. The variation in crack lengths will probably make the data beyond initial failure somewhat suspect. However, the initial damage loads are still valid in all cases. This behavior is plausible due to the fact that damage initiation is a statistical quantity, and the materials at each crack tip are not identical. There is a variation in the flaw content, location, and size, which serve as damage initiation sites. Once the crack begins to grow at one location, and propagates into the structure, the strain energy release rate at the longer crack tip should be higher as well. This is due to the longer moment

arm caused by the longer delamination length. This should keep the longer crack propagating more than the short crack.

One way to mitigate this effect might be to force the cracks at the flange tips to be the same length for each test by manually advancing the crack, as by prying the crack open. Due to the differential crack growth in the specimens, and the previous discussion, the longest observed crack length was used in the FEA models at the experimentally observed propagation load.

CHAPTER 6

NUMERICAL RESULTS AND DISCUSSION

The results of numerical modeling performed with the ANSYS 5.3 finite element analysis (FEA) code are presented in this chapter. The analysis techniques and results are discussed with regard to their impact on detail region design. The DCB specimens were modeled to establish predictive ability for strain energy release rates (G) with the VCCT methods and to investigate the effects of modeling parameters such as mesh sizing and crack length to crack closure (a/da) ratio on G calculations. Once established, these techniques were applied to skin-stiffener models to predict damage onset and propagation behavior.

Analysis techniques appropriate for each specimen type were applied to determine predictive capability with FEA. Comparisons of FEA model displacements with experimentally observed values were used to validate basic model performance and stresses and strains were calculated to determine likely sites for damage initiation. A strength-based failure approach was used in areas where stress singularities (Chapter 2) were not present. The load to initiate fracture was determined by multiplying the applied load by the ratio of ultimate strain to applied strain, since stress and strain increase linearly with load for a linearly elastic material. In regions with a singularity, such as the flange tip, a fracture mechanics analysis was required. This involved calculating strain

energy release rate values and the use of the linear interaction criterion (Eq. (5)) for crack growth. The load at damage onset was calculated by multiplying the applied load by a ratio determined from the linear interaction criterion. This ratio is based upon the fact that strain energy release rate increases with the square of the applied loading. This technique is presented in more detail for the benefit of designers and analysts in Appendix A. A flowchart of a global-local design approach incorporating these techniques was provided as Figure 13 of Chapter 2. The FEA predictions for damage initiation load and location were compared with experimental results to validate these design approaches for different specimen configurations.

DCB Modeling

The success of substructure modeling with FEA is heavily dependent upon the implementation of accurate material properties for the polyester/E-glass system. This involves data for elastic constants, strength values, and interlaminar fracture toughness results. The elastic constants and strength values for polyester/E-glass composites have been reasonably well established by Mandell and Samborsky [1]. The DCB and ENF tests, presented in Chapter 5, were performed to establish an accurate database for the interlaminar fracture properties. Different Mode I interlaminar fracture toughness (G_{Ic}) values were observed with variations in ply interface lay-up and different experimental calculation methods. Because of this, the FEA calculations for G had to be compared with the experimental test results to determine which data set would work best with predictive design methods.

The variation in predicted G values with mesh sizing for the VCCT-1 and VCCT-2 methods also had to be established. This was necessary to find the valid range of crack lengths and (a/da) ratios for predicting flange tip damage onset and crack propagation with the VCCT methods. Recall that the terms in the (a/da) ratio with the VCCT method are crack length (a) and crack closure length (da). Once the effects of these parameters on G predictions were understood, the fracture mechanics techniques could be extended to the substructure models for validation on more complex geometries. This approach would allow wind turbine blade designers to analyze detail regions that cannot be approached with a standard strength-based failure criterion.

DCB models were created in ANSYS to investigate mesh sensitivity and correlate ANSYS output with experimental results. Models were created for the [(0)]₁₀ and [(+45/-45)]₁₀ DCB specimens. The [(0)]₁₀ models were used to study mesh sensitivity for the VCCT methods at various crack lengths and (a/da) ratios. The [(+45/-45)]₁₀ DCB models were utilized to correlate FEA output for G values with experimental test results at various crack lengths.

[(+45/-45)]₁₀ DCB Models

In order to perform predictive work with fracture mechanics, confidence is needed in both the experimental fracture toughness data, and the ability to calculate strain energy release rates with the FEA code. The [(+45/-45)]₁₀ DCB test results were compared with FEA predictions because of the pronounced toughness increase with crack growth (R-curve behavior) and the variability in the experimental results with different calculation methods. It was believed that if the R-curve could be adequately reproduced with FEA

for this complicated behavior, it could easily be modeled for the more consistent $[(0)]_{10}$ specimens. Furthermore, comparison of FEA values to experimental data was necessary to determine which of the two experimental calculation method data sets (MBT or Area) should be used with the FEA predictions.

Each FEA run was performed by applying the critical load at propagation for a specified crack length from an actual DCB experimental test. The particular DCB coupon modeled was specimen number 211, cases a through g. Both the VCCT-1 and VCCT-2 methods were used to calculate G_{Ic} for each case. The unit loads for the VCCT-2 methods were placed at the corner and mid-side nodes for comparison, with the other corner node fixed with coincident nodal coupling (multi-point constraints). Mesh size ratios for (a/da) greater than 200 were used in all cases to reduce mesh size effects.

The results are presented in Figure 37 for the MBT calculations and FEA R-curves. It is apparent that the FEA results follow the same trend of increasing G with increasing crack length. The FEA values are in the same general range as the MBT experimental values. A consistent difference between the VCCT methods is evident from Figure 37. The VCCT-2 method with mid-side node loading and fixed corner nodes always predicts the highest value for G_{Ic} . It was consistently 17 percent higher than the VCCT-1 method, and 28 percent higher than the VCCT-2 method with corner node loading. It also predicted G values well above the experimental data over the entire range. These initial results imply that the mid-side loading approach may not provide accurate results.

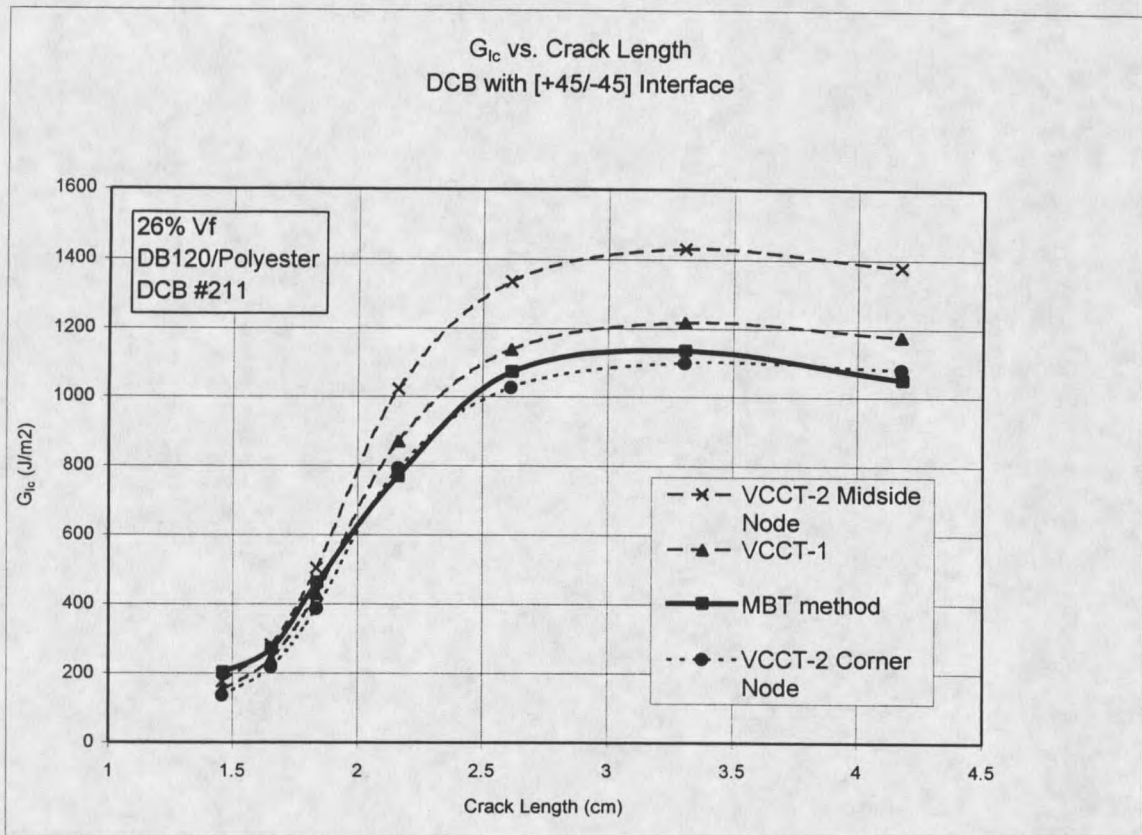


Figure 37. FEA G_{Ic} calculations vs. MBT data for $[(+45/-45)]_{10}$ DCB specimen.

The VCCT-1 and VCCT-2 with corner loading are in much better agreement with the MBT data. The VCCT-1 results are slightly above the MBT values, while the VCCT-2 data with corner loading are just below them. If these trends continue, it means that the VCCT-1 method will be more conservative for use in predictive analysis since higher predicted G values will translate into a lower calculated damage onset or propagation load with the linear interaction criterion. This behavior is explained in detail in Appendix A, which outlines procedures and formulas for crack growth and damage initiation prediction with fracture mechanics.

It was believed that the use of the VCCT-2 corner node method would result in an underestimate for G due to the load placement at the corner nodes combined with the displacement functions (quadratic) for the higher order elements (eight-node quadrilateral) used in this model. The results from the VCCT-2 technique with corner node loading confirmed this suspicion. The low calculation for G happened because the appropriate closure loads at the corner nodes did not completely close the crack at the mid-side nodes. More energy input was still required for complete crack closure at the mid-side nodes and an underestimate for G was the result. This problem could be fixed by forcing the mid-side node to lie on a straight line between the corner nodes, as some FEA programs allow, or by using an element type that assumes a linear displacement along the element boundary.

The high predictions for G from the VCCT-2 mid-side node loading method may also be caused by the quadratic displacement functions for the 8-node quadrilateral element type (Plane 82). The quadratic displacement curve must pass through the nodes on the element boundaries. When the mid-side nodes are brought together to close the crack, the half sections of the elements that form the crack closure length have to overlap slightly due to the quadratic displacement curve that connects these nodes. This means that the crack is closed too much and an overestimate for G will be the result.

It appears that the VCCT-1 technique is the preferred method for predictive fracture mechanics analyses based upon these initial results. This will be investigated further by comparing the results for the $[(0)]_{10}$ DCB tests and analyzing the mesh sensitivity of these techniques.

The MBT data points shown in Figure 37 were for the MBT method. If the Area method results were plotted, they would be nearly twice as large as the MBT values over the entire range, as discussed in Chapter 5. Using the Area method G_I values with FEA would result in large overpredictions for calculated delamination onset loads. The MBT results should be the experimental values used in conjunction with FEA for predictive work based upon the correlation with the FEA results.

[(0)]₁₀ DCB Models

The [(0)]₁₀ DCB models were used to study the effects of mesh refinement and to further investigate variations in the VCCT methods. In order to establish the correlation of the various methods to experimental test data, three actual test results were modeled for the [(0)]₁₀ DCB specimens. The experimental critical load and crack length were used, and the MBT G_I values were directly compared to the calculations of the three methods. The results for the three test cases are presented in Figure 38. The VCCT-1 method produces the best results for all three cases. The G_I values predicted with this method were 2 to 5 percent below the experimental MBT data. This compares favorably to the VCCT-2 mid-side node method, which overestimated G_I from 15 to 18 percent, and the corner node method, which underestimated G_I by 22 percent.

Two different mesh sensitivity studies were performed—one for intermediate to high (a/da) ratios, and another for very low ratios. To study the intermediate ratio case with (a/da) ranging from 62 to 1006, DCB 503 b was modeled. The loading and crack length were constant at 27.7 N/cm of width and 4.138 cm, respectively, while the mesh surrounding the crack tip was successively refined. A plot of the mesh refinement around

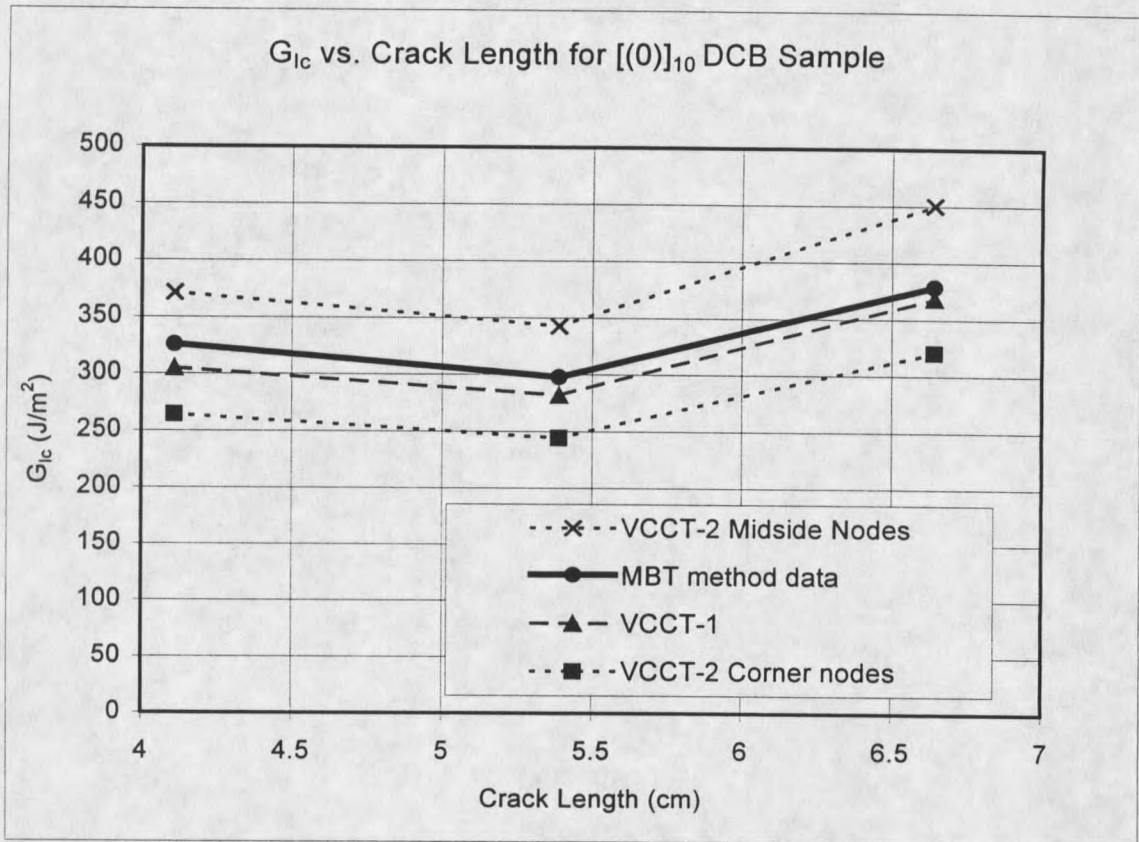


Figure 38. FEA G_{Ic} calculations vs. MBT data for $[(0)]_{10}$ DCB specimen.

the crack tip is shown in Figure 39. The results for the VCCT-1 and VCCT-2 corner loading methods are presented in Figure 40. The VCCT-2 mid-side node method was not calculated due to its consistent overestimation for G at high (a/da) ratios which was discovered in the $[(+45/-45)]_{10}$ models. The VCCT-1 method was quite independent of crack length (Fig. 40), while the VCCT-2 values decreased and stabilized with increasing (a/da) ratio. The VCCT-1 method produced higher G values than the VCCT-2 corner method over the entire range as previously noted. After the results for each method stabilized, at $(a/da) = 1000$, the VCCT-2 value was 14.4 percent lower than the VCCT-1

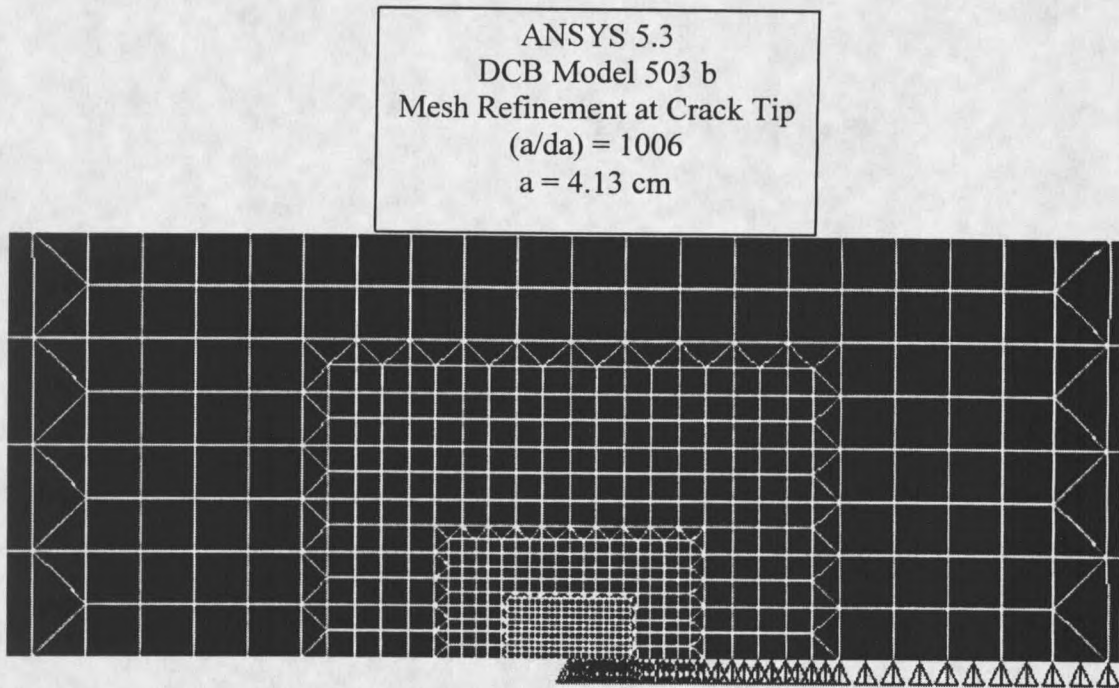


Figure 39. Mesh refinement at crack tip for DCB 503 b.

method. In Figure 41 the results are plotted as the percent change in the values for each method, normalized with the value for each method at $(a/da) = 1000$. This result shows that the VCCT-1 results changed by 1 percent or less over the displayed (a/da) range, which is excellent. The VCCT-2 method displayed differences of up to 9 percent at the lower ratios. These results indicate that the VCCT-1 technique is far less sensitive to mesh size variations and is the better method for fracture mechanics analysis with FEA.

A small crack length was investigated with the same DCB model to establish predictive trends at low (a/da) ratios for the VCCT-1 and VCCT-2 mid-side node methods. The mid-side node method was included in this study to determine its mesh sensitivity and to observe whether or not it continued to produce high estimates for G at lower (a/da) ratios. The crack length was constant at 0.328 cm, and a load of 35.0 N/cm

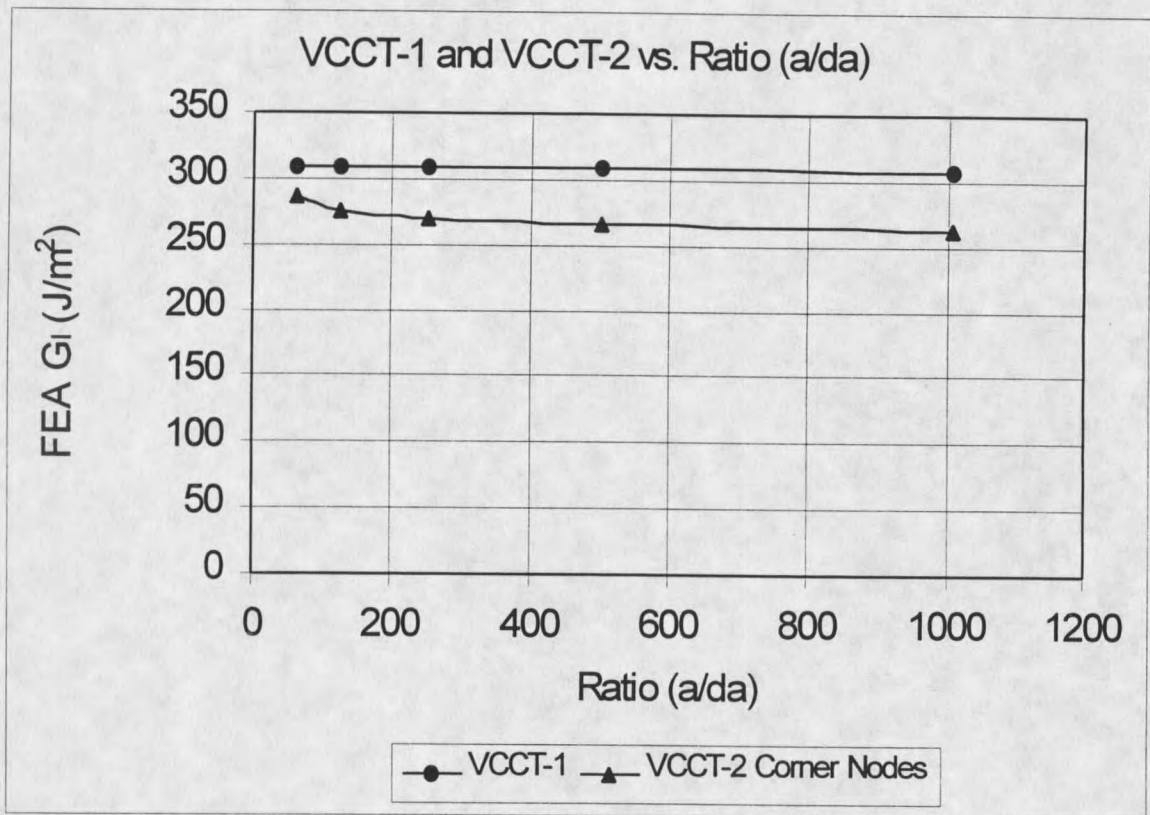


Figure 40. Mesh sensitivity for VCCT-1 and VCCT-2 corner node methods.

was applied to the DCB in each case. Ratios of (a/E_w) (where E_w is element width) from 5 to 1280 were investigated through successive mesh refinements at the crack tip. The ratio is presented as (a/E_w) , instead of (a/da) , because the (a/da) ratio for the VCCT-2 mid-side node method is actually twice the (a/da) ratio for the VCCT-1 method for identical models. This is due to the fact that the crack closure is one half the element width for the mid-side node closure approach. Presenting the results in terms of (a/E_w) provides a more equal comparison of the data with regard to element size and overall model complexity.

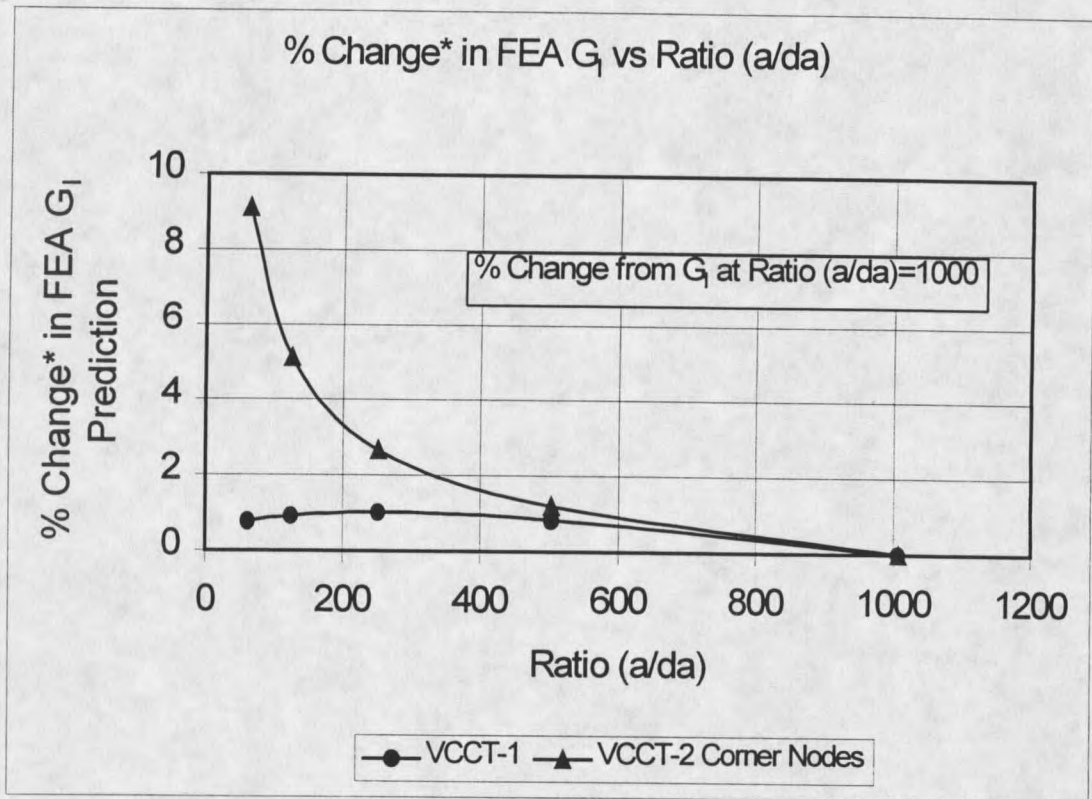


Figure 41. Percent change in FEA G_I calculation vs. ratio (a/da).

The predicted G_I values for both methods decrease as the (a/Ew) ratio gets smaller (Fig. 42). The VCCT-2 mid-side method continues to predict much higher values for G_I . At an (a/Ew) ratio of 80 and beyond, it is over 22 percent higher than the VCCT-1 method. Furthermore, it appears to be more mesh sensitive than the VCCT-1 method at (a/Ew) ratios below 80. The VCCT-2 mid-side method seems to be stable at ratios greater than 80, while the VCCT-1 method is quite stable down to an (a/Ew) ratio of 20.

A more insightful presentation of this data is shown in Figure 43 where the results are plotted as the percent reduction in G_I from the stabilized value for each method at (a/Ew) = 1280. The G_I value for the VCCT-1 is fairly mesh insensitive, even at very low

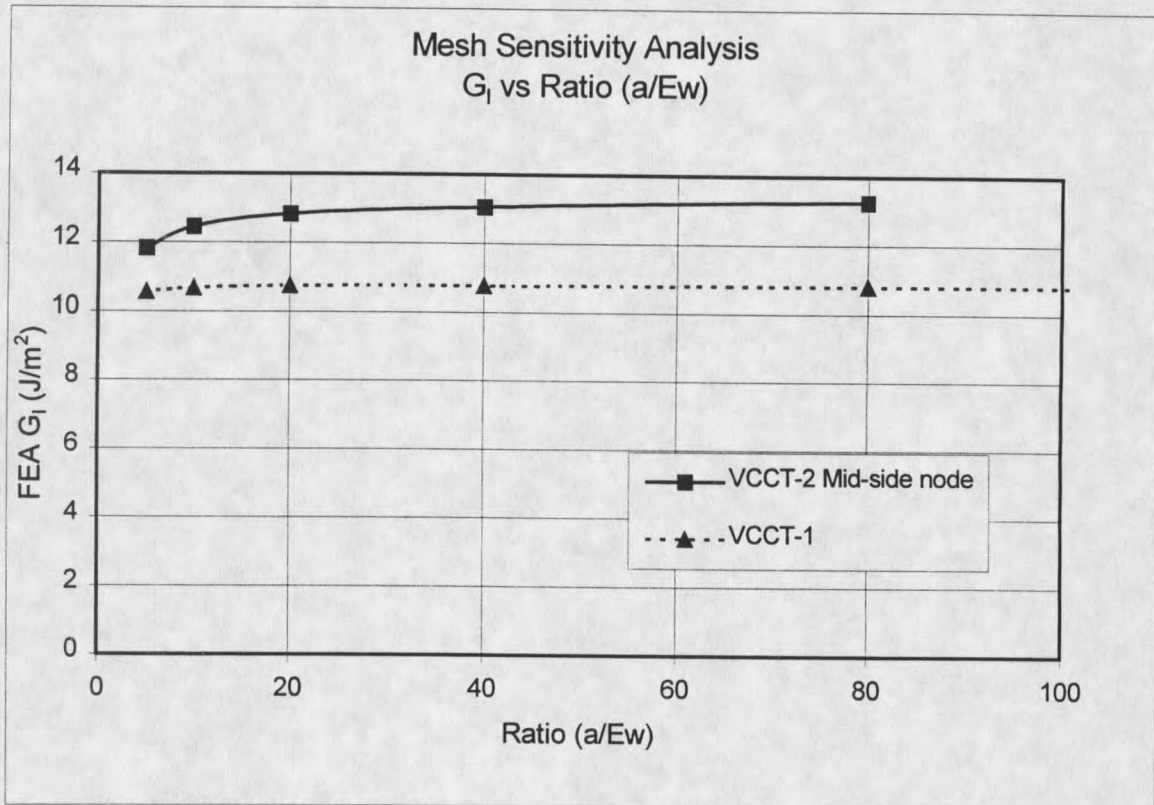


Figure 42. Mesh sensitivity analysis for VCCT-1 and VCCT-2 mid-side node methods at low (a/da) ratios.

(a/Ew) ratios. Recall that (a/da) ratios for FEA analysis from 50 to 200 have been recommended in the literature [27]. For the VCCT-1 method, at (a/Ew) = 40, there is only a 0.5 percent reduction in G_I , while at (a/Ew) = 20, a 0.75 percent reduction exists. Even at (a/Ew) = 5 the predicted G_I value differs from the stabilized value by only -2.4 percent. The VCCT-2 mid-side node method shows a greater variation in G_I with changes in the (a/Ew) ratio (Fig. 43). The percent reduction from the stabilized value ((a/Ew) = 1280) is over 2 percent at (a/Ew) = 80, and is nearly 6 percent at (a/Ew) = 20. This indicates that the VCCT-2 method should not be used with low (a/Ew) ratios due to the variation in G value with mesh sizing.

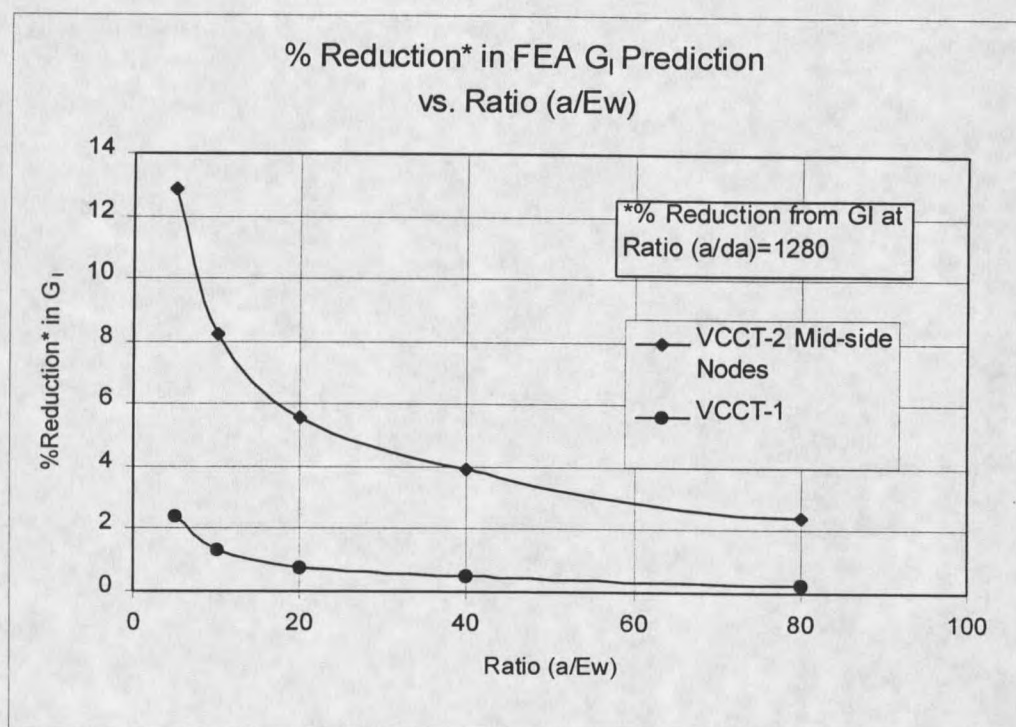


Figure 43. Percent reduction in FEA G_I calculations vs. ratio (a/Ew).

The results for the VCCT-1 technique are encouraging for the designer since they indicate that minimal error is introduced by utilizing coarse meshes in the FEA models with this method. This allows fracture mechanics estimates to be performed with coarsely meshed models which solve much more quickly than highly refined models and still provide good predictive results. Based upon these results, it appears that the VCCT-1 method will provide relatively converged results for ratios of (a/Ew) greater than 20 with 8-node quadrilateral elements.

The results of the DCB modeling have shown that the VCCT-1 method is the preferred tool for predicting G values with FEA. The VCCT-1 has good mesh size stability and only requires one FEA analysis to calculate G for all modes of crack growth.

In contrast, the VCCT-2 method needs an initial analysis to load the structure, and one additional run for each mode of crack extension. This means that for a structure with Mode I and II loading, the VCCT-1 method will be at least three times faster than the VCCT-2 methods. This fact further increases the utility of the VCCT-1 approach for designers. The VCCT-1 method values also match the experimental data better than the VCCT-2 techniques.

The results for the MBT calculation method correlate with the FEA results much better than the Area method results. This is because the FEA and MBT methods use the same force and crack length values while the Area method includes actual energy dissipated which is not obtainable with the FEA and MBT methods. Using the MBT material fracture data with the VCCT-1 method should make accurate predictions of wind turbine blade damage possible. This type of approach will be vital for the improved design of detail regions such as flange termination areas. This should reduce the design oversights that have plagued skin-stiffened structures in the past.

Thin-flanged Stiffeners

Co-Cured Specimens

Tensile Loading. The one-piece thin-flanged stiffeners were modeled in ANSYS as described in Chapter 4. The goals of the stiffener model were to predict displacements, and initial damage load and location. The two prime areas of interest for damage onset were the web/flange fillet radius area and the flange tip region. These areas have typically served as damage initiation sites in pull-off tests [5, 6, 9, 15]. The

damage initiated at the bend region (Fig. 28) in every test case performed in this study. The verification of the slope of the load/displacement behavior for the FEA model showed good agreement with the average experimental slope. The FEA value differed from the experimental average by only -2.4 percent.

The first site investigated for damage was the bend region. Experimental observations (Fig. 28) of initial damage showed transverse cracks in the surface (+45/-45) ply and the (0) plies beneath them. These cracks seemed to form at roughly the same load since both cracks were present after initial damage detection. The strain in the plies at the bend was calculated at the experimentally observed damage initiation load of 85.45 N/cm. Since this was a 2-D analysis, the strain components in the FEA global axes were applied as laminate loads in a composite analysis program to get fiber longitudinal and transverse stresses and strains for comparison with material strength data. The strength data for the D155 and DB120 materials [1] presented in Tables 2 and 3 of Chapter 4 were used to predict damage. The maximum in-plane strain in the bend region was in the (+45) degree surface ply. The strain components had to be viewed in a local cylindrical coordinate system for the bend region rather than the global system. This local system was necessary to properly align the material properties as they curved from the web to the flange area (Fig. 21). Typical strain contour plots in the bend region are presented in Figures 44 and 45. In the bend region local coordinate system the X direction is the radial (R or through-thickness) direction, the Y direction is following the curved region (θ or tangential), and the Z coordinate is out of the page. There was no Z strain component since this was a plane strain analysis. The maximum in-plane tangential

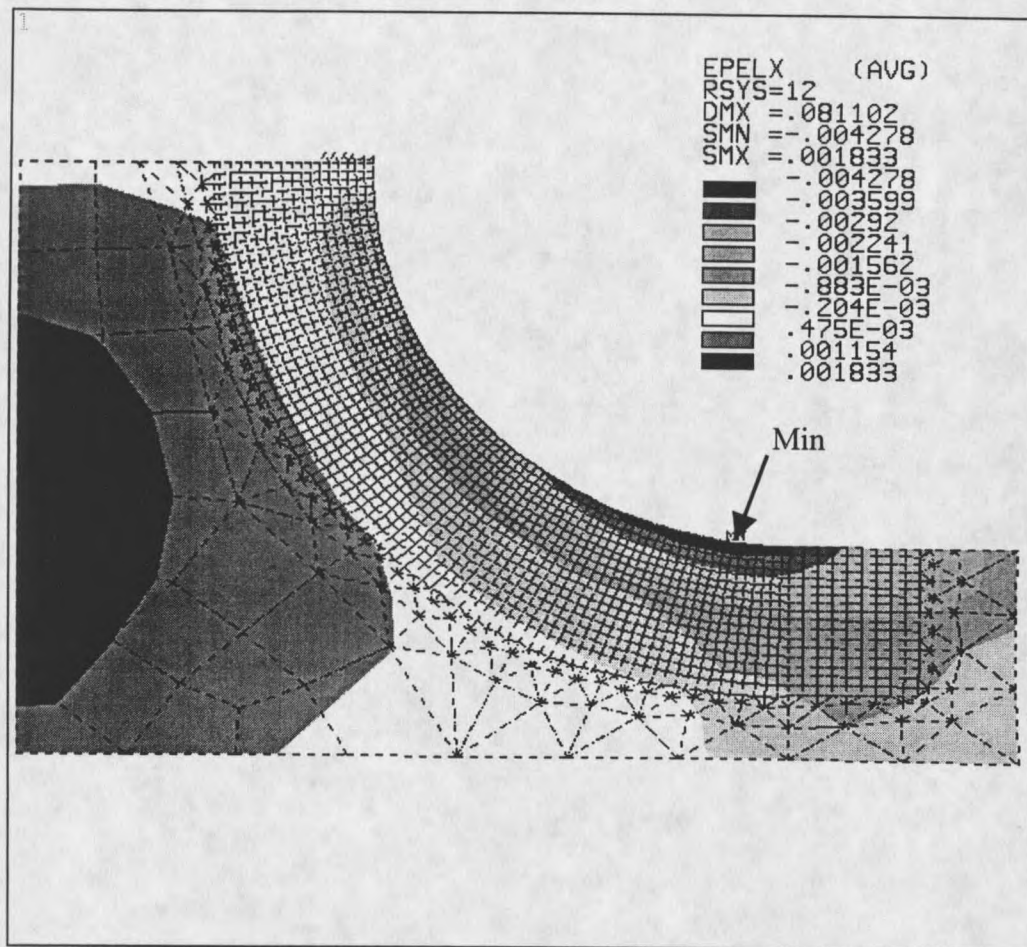


Figure 44. Radial strain plot in the bend region for thin-flanged stiffener model.

strain at the bend was 0.00599 within the (+45) degree surface ply. The (0) degree ply directly beneath the surface (+45/-45) fabric had a tangential strain of 0.00364. The radial (through-thickness) and shear strains in these plies were not high enough to cause damage. The radial stress component in the surface (+45) ply was -0.004278, with an allowable compressive strain for this material of -0.0121. The maximum radial strain observed was 0.00183 at the web centerline, which is below the ultimate transverse strain

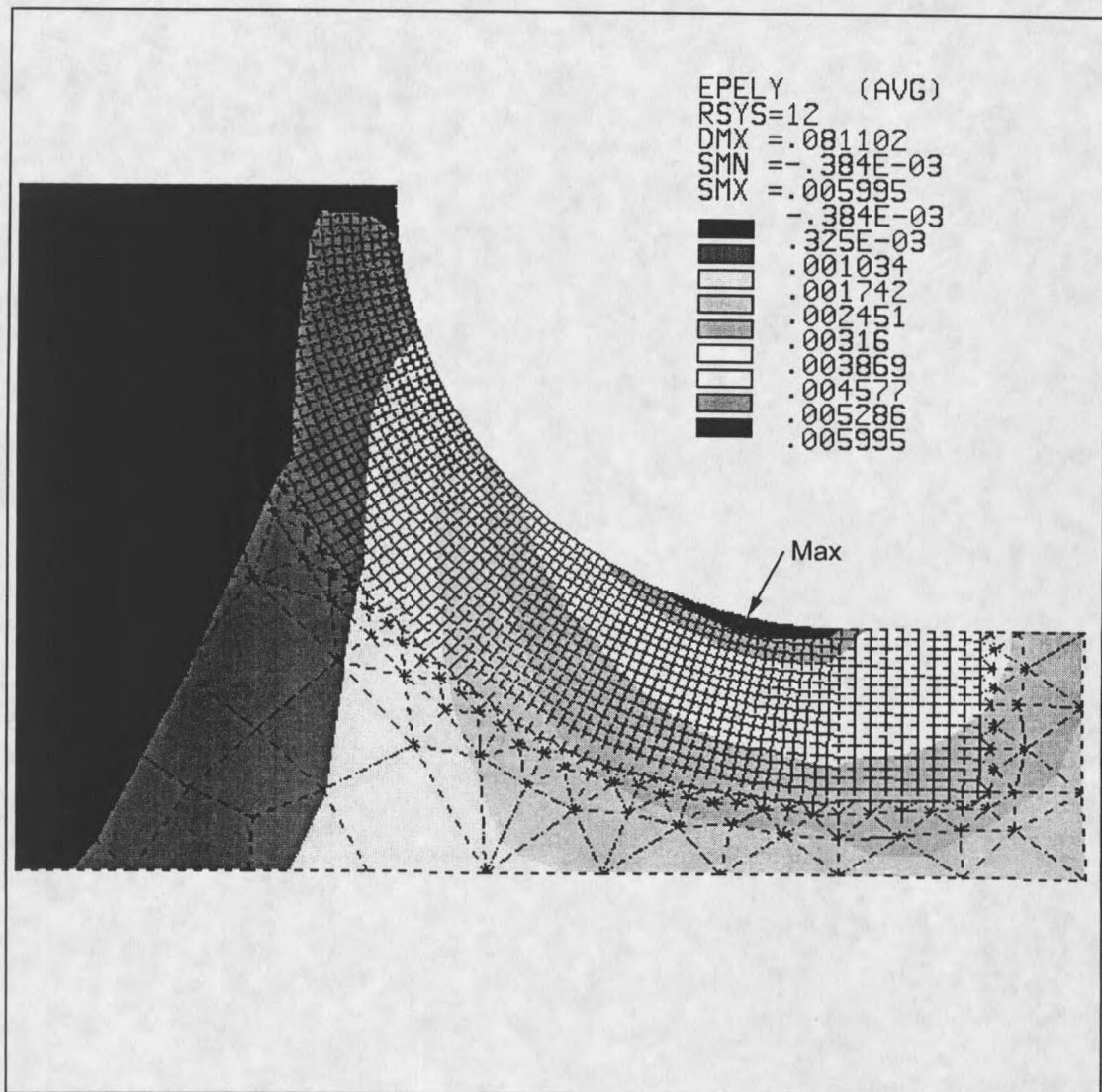


Figure 45. Tangential strain plot in the bend region for thin-flanged stiffener model.

value in tension of 0.003 for this material. The maximum observed XY shear strain was 0.001, while the ultimate transverse shear strain allowable is 0.0206.

The appropriate strains were applied to the (+45) and (0) plies with a laminate analysis program. Failure was determined by applying both the maximum strain and the quadratic (Tsai-Wu) failure criteria. The results are presented in Table 11. The maximum

Table 11. Failure prediction in the bend region for thin-flanged stiffener specimens.

Fracture Loads for Thin Flanged Co-cured Stiffeners			
Fracture Location	Experimental Fracture Load (N/cm)	Maximum Strain Criterion Prediction (N/cm)	Quadratic Criterion Prediction (N/cm)
(+45°) Bend Surface Ply	85.45	93.99	70.92
(0°) Bend Region Ply	85.45	93.14	92.29

strain criterion predicts that fracture will occur when the strain in any direction equals the ultimate strain allowable in that direction. The quadratic criterion is based upon an interaction of the various stress states in the laminate [39] and will generally predict lower fracture loads than the simpler maximum strain criterion. The quadratic failure criterion will not directly predict the failure mode as will the strain criterion. The maximum strain criterion predicted fracture in the (+45) surface ply at 93.99 N/cm, or 10 percent above the experimental average load. The quadratic criterion predicted damage onset at 70.92 N/cm, or 17 percent below the experimental average. Thus, the strength-based predictions bound the experimental average value. The failure mechanism in the bend surface (+45) ply was predicted as transverse tension failure with the maximum strain criterion. This appeared to be the damage mode in the specimens during the tests as reported in Chapter 5.

Martin and Jackson [40] reported that damage prediction in curved composite regions is difficult and should be approached with caution. They referenced Hart-Smith [41] who found that strengths derived from flat tension specimens might not be the same as the in-situ strength of bend region material in composite structures. This may

contribute to the difference between the damage load predictions and experimental values in the bend region.

Experimental observations showed that a transverse crack formed in the (0) degree plies in the bend at the same time the crack in the (+45/-45) surface plies formed. Tests were stopped immediately after initial damage was detected and both cracks were present. The strains were analyzed in the (0) plies to see if they were at the failure point as well. When the (0) degree ply strain was input into laminate analysis, the predicted damage load was 93.14 N/cm with the maximum strain criterion. This is 9 percent higher than the experimental average. The quadratic criterion predicted 92.29 N/cm, or 8 percent above the experimental average. These load values are nearly identical to the prediction for the (+45/-45) surface ply fracture with the maximum strain criterion. Therefore, it is not surprising that both cracks seemed to form simultaneously during the experimental testing.

The next area analyzed for initial damage was the flange tip termination. This region does not lend itself to a strength-based prediction due to the existence of a singularity in the peel stress, described in detail in Chapter 2. To circumvent this problem, a fracture mechanics approach was utilized to predict initial fracture load (Appendix A). This method assumes that immediately after damage onset there will be a crack of finite width in the structure. Furthermore, it assumes that the load to propagate this very small crack is the same as the fracture onset load without the crack present. Values for G_I and G_{II} can be calculated by modeling a very small crack at the likely damage location and then applying a load case and a VCCT prediction method. The

values for G are then used with an appropriate mode interaction criterion to predict crack propagation load. The linear interaction criterion (Chapter 2) was used in the following analysis.

The first step is to verify the existence of the singularity to make sure this technique is warranted. At the experimental damage onset load, the peel stress at the flange tip was calculated to be 260 Mpa. This is thirteen times greater than the peel strength of a typical E-glass/polyester composite and yet the flange tip showed no damage during the tests. In addition, the maximum peel stress value in FEA was increasing with every mesh refinement. There was clearly a need to analyze the flange tip with a fracture mechanics approach due to the flange tip peel stress singularity.

A 0.155 mm long crack was modeled at the interface between the skin and flange at the flange tip. The elements were refined to give an (a/d_a) ratio of 20. This was based upon the results from the DCB analyses that showed good predictive ability for G_I and G_{II} even at this low (a/d_a) ratio. The VCCT-1 method was applied to calculate G in Modes I and II. The output value for G_I was 25.8 J/m^2 while G_{II} was 14.67 J/m^2 . A fracture load of 195.38 N/cm is predicted using the linear interaction criterion and the initiation values for G_{Ic} and G_{IIc} of 140.4 J/m^2 and 2001.0 J/m^2 . This is much higher than the observed load to cause damage at the bend region of 85.45 N/cm and is well above the maximum load of 132.7 N/cm reached in the pull-off tests.

This analysis showed that damage would not initiate at the flange tip for pull-off loading with the thin-flanged stiffeners. This was known a priori from experimental testing. However, this type of analysis will be essential for predictive design work for

skin-stiffener detail regions with different geometries. If a fracture mechanics approach were not applied to the flange tip, large errors in the damage onset load predictions would occur. In this case, a stress-based analysis would have incorrectly predicted both the damage initiation load and the location within the structure. This example illustrates the importance of applying fracture mechanics to perform damage onset predictions in regions of very high stress gradients. It is essential that designers recognize situations where strength-based approaches are invalid. This should prevent the failures that have resulted from such detail region design oversights.

Compressive Loading. The same skin-stiffener model was used to predict behavior for the compressive loading case. As described in Chapter 5, the compressive loading did not cause damage in the T stiffener bend region, or at the skin-stiffener interface. Instead, the initial damage was transverse tension cracking in the (+45/-45) ply on the bottom of the skin at 94.0 N/cm. The damage progressed upward through the skin until final fiber tension failure in the bottom skin (+45/45) ply.

The FEA model displacement was calculated to be 8.0 percent lower than the experimental average deflection at the experimental damage load. The maximum in-plane strain at this load condition was 0.0435 in the bottom (+45/-45) ply. This strain state was analyzed with a laminate analysis program and the maximum strain and quadratic failure criteria. A transverse tensile failure mode was predicted by the maximum strain criterion, but it overestimated the damage onset load by 38 percent (Table 12). However, the quadratic criterion estimate was very close to the experimental

Table 12. Damage load predictions for thin-flanged stiffener specimens.

Damage Load for Compressive Thin Flanged Stiffener Tests		
Experimental Average Load (N/cm)	Maximum Strain Criterion Prediction (N/cm)	Quadratic Criterion Prediction (N/cm)
94.0	129.7	96.8

average damage load. It predicted a damage load of 96.8 N/cm which is 3 percent above the experimental value.

The differences in the damage load predictions may be due to errors in the FEA model, material property strength variations, or assumptions about the experimental test behavior. The compressive predictions were performed with a model that was initially generated to analyze the tensile pull-off mode of loading. The model did not have all of the plies in the lower skin section modeled individually. Instead, it used smeared composite properties for the bottom ply layers to simplify the model. This may cause some error in the calculated stress state in the bottom (+45) ply which was the area of initial cracking in the test specimens. However, the smeared modulus in the bending direction was quite close to the modulus of a (+45/-45) ply. For this reason, the FEA model was considered adequate for the compressive loading case. The variation in transverse strength data could also contribute to errors in damage load predictions. In addition, it is possible that small errors were introduced with the plane strain assumption in the FEA model. The actual test specimens were not in a perfect plane strain condition as discussed in the Experimental Results section of Chapter 5.

Thick-flanged Stiffeners

Thick Skin with (0/0) Interface

The thick-flanged skin-stiffeners were co-cured in two configurations. One utilized a thick skin with a (0/0) interface (T 5200 series) while another had a thin skin and a (+45/-45) interface (T 5000 series). The thick-flanged stiffeners were tested in a tensile pull-off mode. The results for initial damage onset and maximum loads were presented in Table 10 of Chapter 5.

The thick-flanged stiffeners were modeled in ANSYS as described in the Substructure Modeling section of Chapter 4. The FEA models were used to predict displacements, damage onset, and crack propagation behavior.

The FEA results for the T 5200 stiffeners are presented in Table 13. The FEA

Table 13. Experimental vs. FEA results at average experimental damage onset load.

Experimental vs FEA Results at Average Experimental Damage Onset Load			
Specimen Type	Experimental Displacement (cm)*	FEA Displacement (cm)	% Difference in Predicted Displacement
T 5000 [45/-45] Interface	0.1086 ± 0.0144	0.1034	-4.8
T 5200 [0/0] Interface	0.0623 ± 0.0038	0.0615	-1.3

* ± One standard deviation.

model yielded a good prediction for displacement at damage onset load when compared with the experimental average. The FEA displacement was 0.0615 cm, or 1.3 percent less than the experimental average. This indicates that the FEA geometry and material properties were modeled very well.

The next step was to predict the damage onset at the flange tip region. Both the VCCT-1 and VCCT-2 corner node loading techniques were employed to predict strain energy release rates. The same method used for the flange tip analysis of the thin-flange specimens was utilized for the T 5200 specimens. The existence of the stress singularity at the flange tip was verified by observing large increases in peel stress at the flange tip with successive mesh refinements. The peel stress at the experimentally observed fracture onset load was 260.6 MPa after the final mesh refinement. This was well above the peel strength for polyester/E-glass of 24.9 MPa. This verified that a point stress strength-based approach would not work and that a fracture mechanics solution was necessary at the flange tip.

A crack length sensitivity study was conducted at the flange tip for small crack lengths and low (a/da) ratios for the VCCT-1 technique. The results of this study (Figure 46) show that the G values are fairly stable down to a crack length of 0.0389 mm which is an (a/da) ratio of five (5). It should be noted that both the crack length and the (a/da) ratio are changing in Figure 46 with (da) constant at 0.00778 mm. In addition, much of the decrease in G with decreasing crack length is probably due to the low (a/da) ratio and not the change in modeled crack length.

Two different initial crack sizes and corresponding (a/da) ratios were modeled to predict initial damage at the flange tip. The first crack had an (a/da) ratio of 26.0 and a length of 0.201 mm. The second crack was slightly smaller with an (a/da) ratio of 20.0 and a length of 0.156 mm. The results for the initial damage load predictions at the flange tip for the T 5200 specimens are presented in Table 14. The VCCT-1 method with the

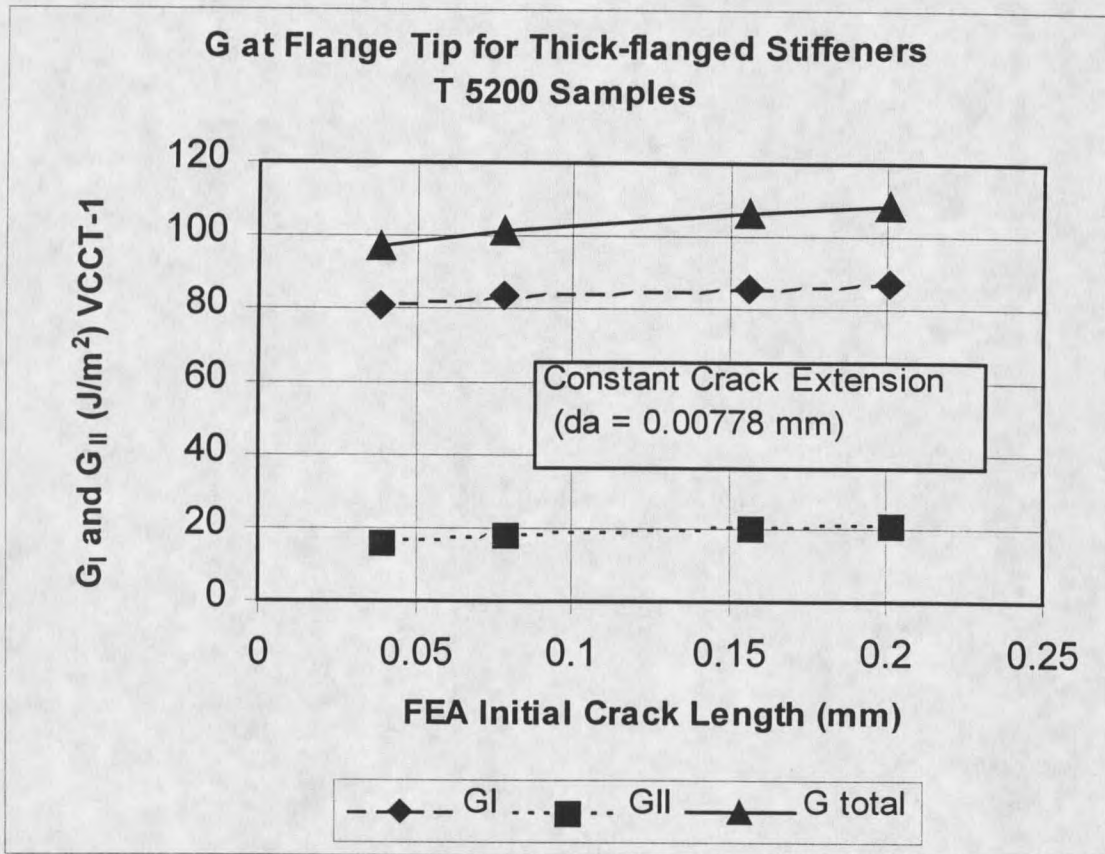


Figure 46. G_I and G_{II} at flange tip vs. ratio (a/da).

Table 14. Initial damage load predictions at flange tip using VCCT-1 method.

Specimen Type	Ratio (a/da)	FEA Crack Length ($a = \text{mm}$)	Experimental Fracture Onset (N/cm)*	VCCT-1 Prediction (N/cm) [@]	% Difference in Predicted Fracture Load
T 5000 [45/-45] Interface	5.0	0.26	58.69 ± 5.64	52.0 ± 7.0 -8.2	-11.4
T 5200 [0/0] Interface	26.0	0.201	152.70 ± 7.53	141.4 ± 25.9 -32.4	-7.4
T 5200 [0/0] Interface	20.0	0.156	152.70 ± 7.53	142.3 ± 26.1 -32.5	-6.8

* \pm One standard deviation.

@ Predicted using average G_{Ic} and G_{IIc} with \pm values calculated using \pm (respectively) one standard deviation for G_{Ic} and G_{IIc} .

0.201 mm crack model predicted an initial damage load at the flange tip of 141.4 N/cm, while the 0.156 mm crack prediction was 142.3 N/cm. The experimental average damage load was 152.7 N/cm. Since the FEA predictions are dependent on the interlaminar fracture toughness values, it is worth investigating the predicted damage loads using ± 1 standard deviation for G_{Ic} and G_{IIc} . The change in predicting the fracture onset load with the 0.210 mm crack was +25.9 and -32.4 N/cm, and the 0.156 mm crack model was +26.1 and -32.5 N/cm. The experimental average damage load falls well within this predicted range.

The damage prediction results for the T 5200 specimens from FEA are plotted against the average experimental results in Figure 47. The results from the load vs.

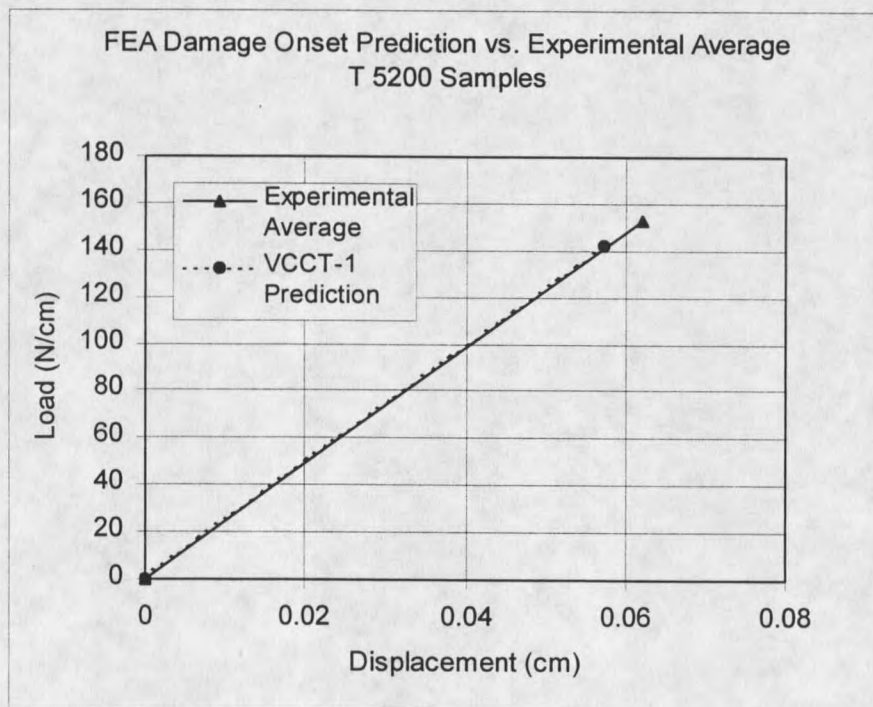


Figure 47. Experimental and predicted load-displacement curves to damage onset for T 5200 specimens.

displacement curve show the good agreement between the predictions and the experimental results. The slopes of the curves are nearly identical, and the fracture onset point predicted by FEA is just below the experimental average, as previously discussed.

The VCCT-2 technique was also used with the same model for the 0.201 mm initial crack. The predicted fracture load [Table 15] with this method was 151.9 N/cm,

Table 15. Initial damage load predictions at flange tip using VCCT-2 method.

Specimen Type	Ratio (a/da)	FEA Crack Length (a = mm)	Experimental Fracture Onset (N/cm)*	VCCT-2 Prediction (N/cm) [@]	% Difference in Predicted Fracture Load
T 5000 [45/-45] Interface	5.0	0.26	58.69 ± 5.64	55.3 +7.5 -8.7	-5.8
T 5200 [0/0] Interface	26.0	0.201	152.70 ± 7.53	151.9 +27.7 -34.8	-0.5
T 5200 [0/0] Interface	20.0	0.156	152.70 ± 7.53	NA	NA

* ± One standard deviation.

@ Predicted using average G_{Ic} and G_{IIc} with ± values calculated using ± (respectively) one standard deviation for G_{Ic} and G_{IIc} .

NA Not Available, no FEA performed for this case.

which is only a - 0.5 percent difference from the experimental average fracture load.

However, based upon the results from mesh sensitivity studies, the VCCT-2 technique is not recommended, especially at such low (a/da) ratios. The good predictive results in this case are probably due to the variance in material fracture toughness data. These results show that the VCCT-1 method is always more conservative than the VCCT-2 corner node method in predicting damage load because it predicts higher G values for a given loading case. To reiterate, the VCCT-1 method is preferred for calculating G values with

FEA due to its stability with respect to mesh sizing and its consistently higher calculated values for G , compared to the VCCT-2 corner node method. The better agreement between the experimental results and the VCCT-2 predictions in the present case should not be used as an endorsement of this technique.

Once damage has initiated at the flange tip, the delamination grows at the skin-flange interface toward the web. This growth was modeled with FEA by releasing coupled nodal sets to achieve the desired crack length. The crack length was chosen as the longest crack in the experimental specimens at a given propagation load. This was due to the observation that once a crack started at the left or right flange, the longest crack would propagate first in subsequent tests.

The results for delamination growth predictions are displayed in Figure 48.

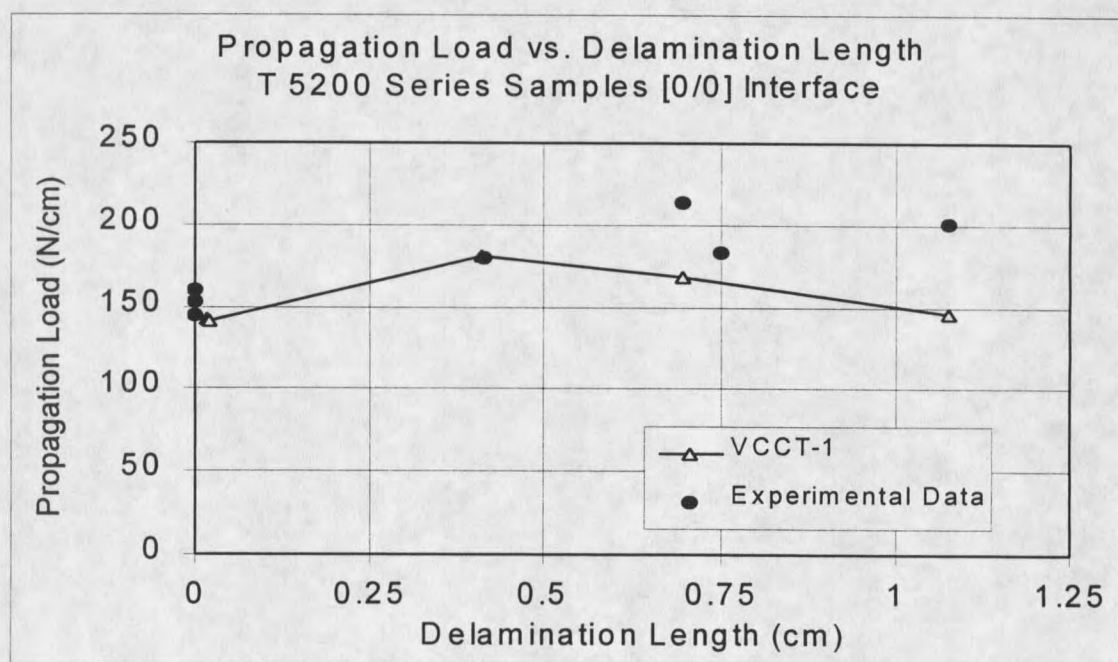


Figure 48. Predicted propagation load vs. delamination length for T 5200 specimens.

Individual data points from experimental tests are plotted along with the FEA predictions for those delamination lengths. The G_{Ic} values used in the linear interaction criterion varied with crack length. The values used were the average values taken from the MBT R-curve data presented in the DCB Specimens section of Chapter 5. The predictions in Figure 48 are for the VCCT-1 method only. The predicted load for propagation at a crack length of 0.4 cm is identical to the experimentally measured propagation load. Beyond 0.4 cm, the predictions are lower than the experimental results. This may be due to the different crack lengths at the right and left flange tips during the experimental tests. This behavior was observed to be more prevalent at longer delamination lengths. The material at the delamination interface may also be tougher in the stiffeners than the DCB test results. This would result in low estimates for crack propagation loads.

Thin Skin with (+45/-45) Interface

The same type of testing and analysis was applied to the thin-skinned (T 5000 series) specimens. These specimens were tested to investigate the influence of skin bending stiffness and validate the predictive ability for crack growth at a (+45/-45) interface.

The FEA displacement prediction [Table 13] at the experimental damage onset load was 0.1034 cm, while the experimental average was 0.1086 cm. This shows that the FEA model is approximately 4.8 percent more compliant than the average stiffness for the experimental specimens.

The prediction for the damage onset load with the VCCT-1 method was presented in Table 14. The predicted value of 51.95 N/cm was 11.5 percent lower than the

experimental average of 58.69 N/cm. However, if +1 standard deviation were used for G_{Ic} and G_{IIc} , the predicted damage load was 58.97 N/cm. The VCCT-2 method once again predicted lower G values and a higher fracture load [Table 15]. The 2-step method predicted damage onset at 55.3 N/cm, which was below the experimental average by 5.8 percent.

The previous results are presented in graphical form in Figure 49, which is a

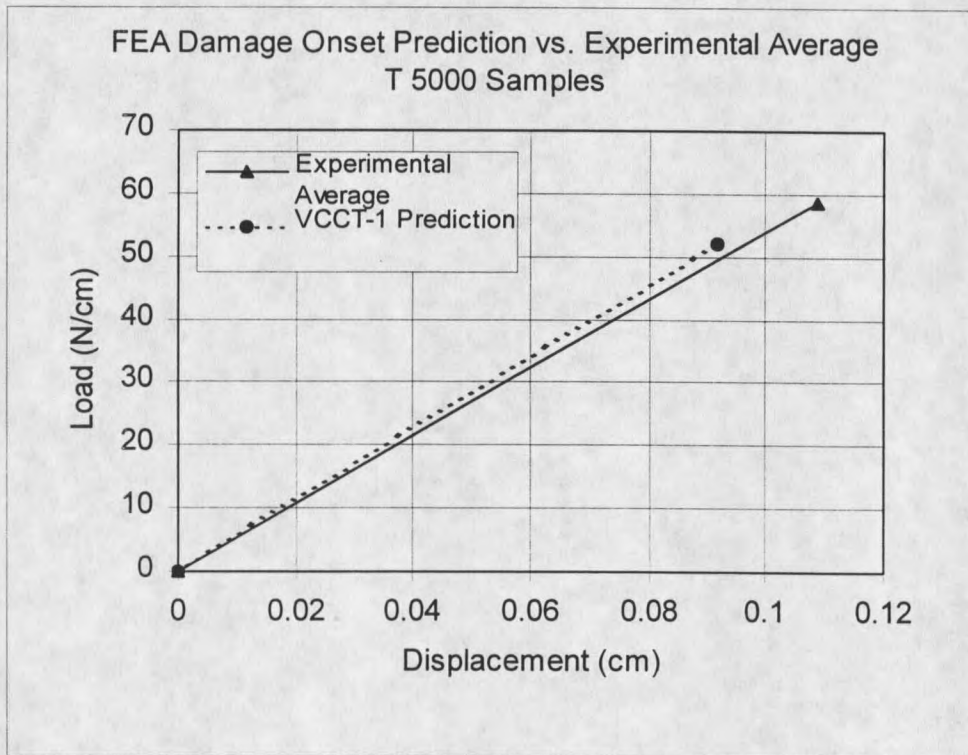


Figure 49. Experimental and predicted load-displacement curves to damage onset for T 5000 specimens.

comparison of the FEA and experimental load vs. displacement curves up to initial damage. As mentioned in the preceding paragraph, the FE model predicts slightly less displacement and lower load at fracture onset than was observed experimentally.

The (a/da) ratio used for the T 5000 predictions was only 5.0, with an initial crack length of 0.26 mm. These parameters may be slightly outside of the desired range for damage onset modeling as determined from the DCB mesh sensitivity studies. This was the smallest mesh sizing that could be accomplished for this model, however. The ply layers at the interface were different thickness in the skin and the flange. This caused problems during the mesh refinement process. As the element sizes were reduced by a factor of 2, 4, 8, etc., the element widths were no longer identical on both sides of the interface. This means that the corner and mid-side nodes were no longer coincident and that the VCCT method could not be used. This problem may be avoided by forcing the elements on both sides of the interface to have the exact same width and thickness during the modeling process. If this condition is enforced, then mesh refinements will produce elements of identical size with coincident nodes. These coincident nodes are then coupled together as nodal pairs with identical degree of freedom values to define the crack length.

A prediction of delamination growth beyond initial damage was performed by combining the FEA model with the material toughness values from the (+45/-45) DCB R-curve results in Figure 24 of Chapter 5. G_{Ic} values on the R-curve were assumed to follow a linearly increasing relation from 140 J/m² at 0 cm to 1028 J/m² at 1.0 cm of crack extension, and then be constant at 1028 J/m², for longer lengths. The predictions for crack growth loads (Fig. 50) are consistently lower than the experimental values. This may be due to errors in material toughness data or lack of symmetric crack growth in the T specimens. The load predictions appear to be about 20 percent lower than the

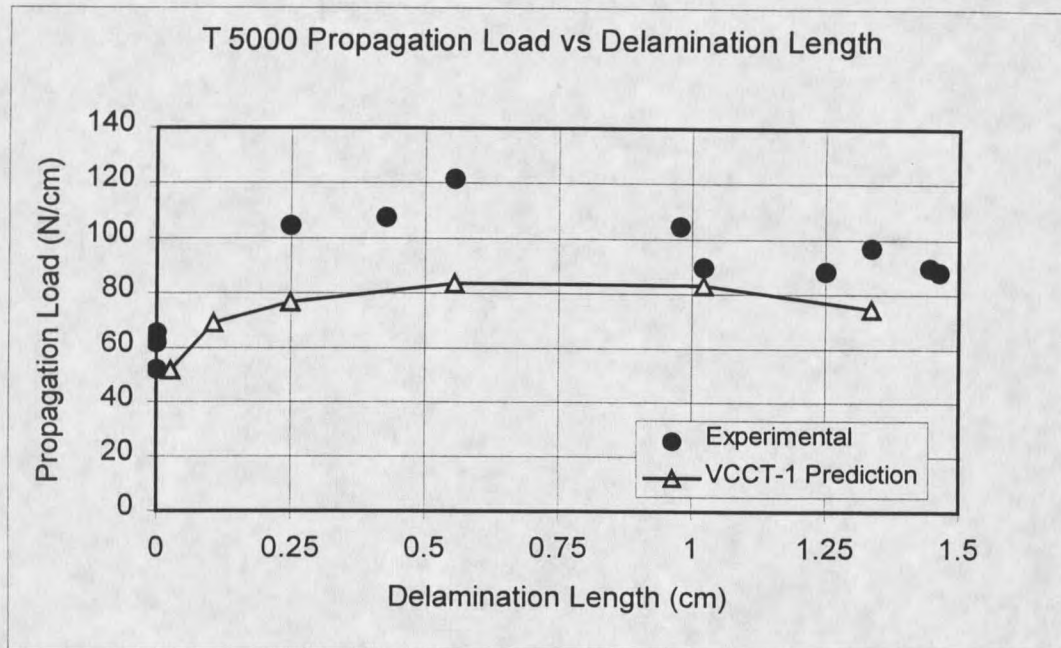


Figure 50. Predicted propagation load vs. delamination length for T 5000 specimens experimental results below 0.8 cm, and get slightly better around 1 cm. The predictions for G_{Ic} would be extremely low if the R-curve toughening behavior were not taken into account. In fact, based upon Figure 50, it seems that the material in the T 5000 specimens is actually tougher than the values used from the DCB R-curve.

The Whitney/Nuismer average stress criterion [37] was used to calculate a characteristic distance for the T 5000 thick-flanged specimens. This technique was described in Chapter 4, Numerical Methods. A curve fit (Fig. 51) was applied to the peel stress distribution at the flange tip. One can see the very high value for the peel stress at the flange tip ($x=0$) in Figure 51. The curve fit was then entered into the average stress criterion integral (Eq. (7)) to calculate the characteristic distance, a_0 . For this material system, a_0 was calculated to be 0.0619 cm. This is approximately the thickness of a D155

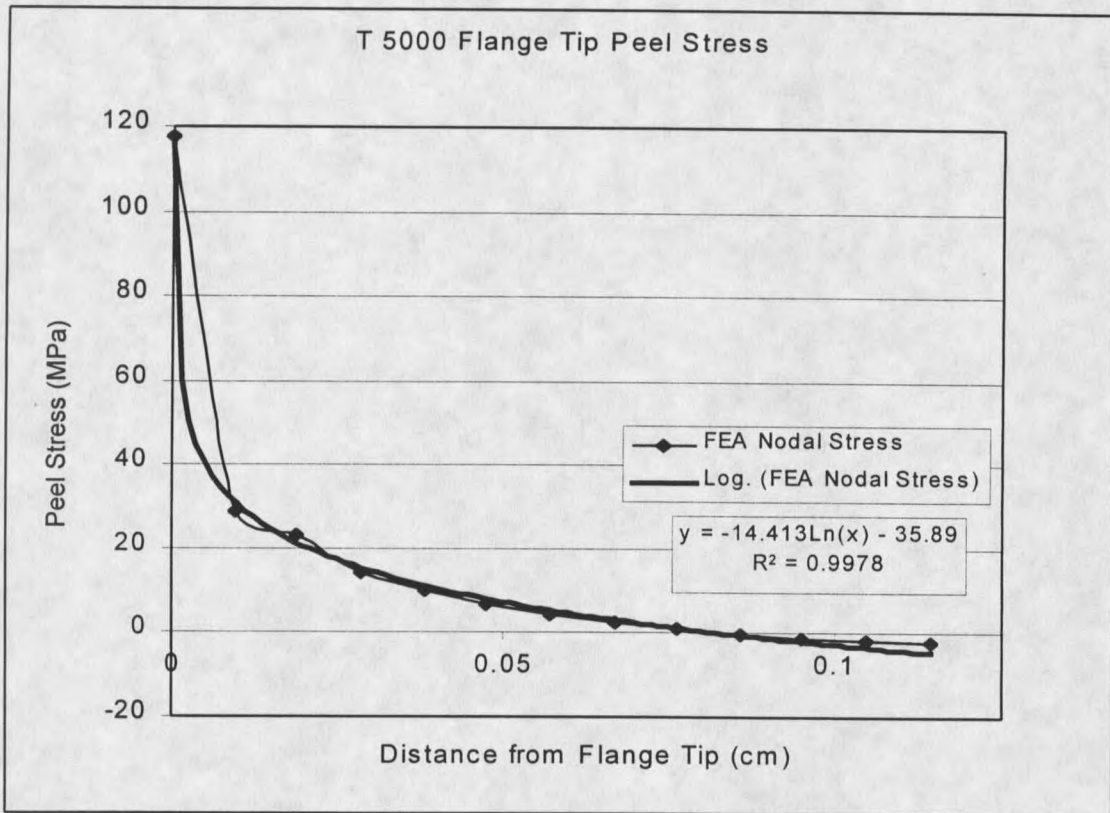


Figure 51. Flange tip peel stress curve fit for use in Whitney-Nuismer failure criterion.

ply layer in a typical laminate. The characteristic distance could be used in design work by finding the stress distribution near a singularity with FEA and using Equation (7). According to the average stress criterion, the material will fail when the average stress over the characteristic distance, a_0 , reaches the strength of the material in the direction under consideration. The average stress criterion has an advantage over a similar criterion called the “point stress criterion” because it uses the integral average of the stress distribution over this region. The point stress criterion states that fracture will occur when the stress at a point, some distance ahead of the discontinuity, reaches the strength of the material. The problem with this criterion is that it may result in large

errors since a small error in the characteristic distance will result in a large error in the predicted stress at that point. This is due to the very steep stress gradient in this area as evidenced by Figure 51. The characteristic distance for the average stress criterion was calculated for the polyester/E-glass material to add to the materials database at MSU but was not used for predictive work in this study.

In this chapter the results of different techniques for analyzing skin-stiffener intersections have been presented. Combinations of strength-based approaches and fracture mechanics predictions were shown to provide good results for determination of damage initiation loads and locations. The strength-based approach was used to analyze damage onset in areas without high stress gradients. The fracture mechanics method was applied to areas of very high stress gradients such as the flange termination area. These methods can also be applied to three-dimensional analyses with the use of appropriate formulas for G with different element types like composite layered shell elements. In addition, these methods may be used with different load cases and geometries such as ply drops, bonded joints, or any region that exhibits very high stress gradients or singular stress fields. The predictive results also showed the need for accurate material strengths and interlaminar fracture toughness data to determine fracture onset loads.

CHAPTER 7

SUMMARY AND RECOMMENDATIONS

A brief summary of the experimental and numerical results is presented in this chapter. Recommendations for stiffener design and analysis methods are presented based upon these results and additional data gathered from previous investigators.

Experimental Summary

DCB and ENF Testing

- Mode I and II fracture toughness changed with variation in fabric ply interface orientation (i.e. (+45/-45) interface was tougher than (0/0) interface).
- G_{Ic} values calculated with the Area method were higher than values calculated with the Modified Beam Theory (MBT) method due to the tortuous crack path topology. This difference was much more pronounced for the (+45/-45) interface specimens than for the (0/0) interface specimens.
- The (+45/-45) interface double cantilever beam (DCB) specimens showed very large toughness increases with crack extension (R-curve behavior). This was due to extensive fiber bridging, tow debonding, and the tortuous crack path.
- The (0/0) interface DCB specimens showed little increase in toughness with crack extension due to the absence of fiber bridging and tow debonding and the relatively smooth fracture surface.
- Fracture toughness values for Mode II growth from end notched flexure (ENF) testing were approximately 9 times greater than Mode I initiation values for the (0/0) interface and 14 times greater than Mode I initiation values for the (+45/-45) interface.

Stiffener Testing

- Damage initiated in the web/flange transition bend region for the thin-flanged stiffeners under pull-off loading. These cracks grew until they had formed delaminations at the flange/skin interface and web centerline. Delamination continued toward the flange tip and upward in the web until final pull-off failure.
- Bonded stiffeners with thin bond lines (0.15 mm) showed essentially no difference in strength compared to the one-piece RTM stiffeners. This is because the crack grew preferentially in the polyester matrix and not in the tougher adhesive layer. In addition, the skin bending stiffness was the same for both specimen types.
- Initial damage and maximum pull-off loads increased with increasing bond-line thickness between the flange and the skin in the thin-flanged stiffeners.
- As the bond-line thickness increased in the thin-flanged specimens the failure mode changed. The initial damage occurred at the flange tip for the thicker bond-line specimens instead of the web/flange bend region. This is due to the increasing peel stress at the flange tip caused by increasing the geometric discontinuity between the flange and skin
- Stiffeners manufactured with tougher resin systems showed large increases in pull-off loads since delamination resistance is dominated by matrix material strength.
- Thick-flanged stiffeners always failed at the flange tip area due to the geometric and stiffness discontinuity in this region.
- Increasing the skin bending stiffness (D_{11}) of the thick-flanged specimens produced large increases in the initial damage onset loads at the flange tip area.
- Compressively loaded stiffeners performed relatively well. No damage was incurred at the web/flange bend region or the flange tip. Instead, the initial damage mode was transverse tension failure in the bottom skin ply.

Stiffener Design Recommendations

- Use the MBT method to calculate G_{Ic} values experimentally. This ensures more conservative results than the Area method.
- Utilize dissimilar fabric ply orientations at delamination prone interfaces in composite skin-stiffener intersections. For example, placing (+45/-45) degree plies together is better than a (0/0) interface. However, interface plies oriented at 90 degrees to the

primary strain should be avoided due to their propensity to form transverse cracks, which may initiate delaminations.

- Toughened matrix materials should be used in all areas that will encounter significant interlaminar stresses.
- Thin flanges should be used whenever possible to increase delamination onset loads. This minimizes the geometric mismatch between the skin and flange at the flange tip. The stiffness of the flange laminate in the loading direction should also be minimized. This lowers the stiffness discontinuity between the skin and the flange. In particular, ratios of flange to skin thickness from 0.5 to 1.5 should be avoided [11].
- The stiffener flange tip should always be tapered by at least 45 degrees. It should never be manufactured with a 90 degree block edge. Tapering reduces the geometric discontinuity at the flange tip, which lowers the interlaminar peel and shear stresses in this region [9, 15].
- In areas where the skin may encounter bending loads, use a higher bending stiffness laminate in the loading direction to keep out-of-plane deflections to a minimum. This will increase delamination onset loads at the skin-stiffener interface.
- Add through-thickness reinforcement (stitching) to the composite in sections that will experience high peel stresses. The entire flange-skin interface and the web just above the web/flange transition are primary areas of concern. Although not tested in this study, previous data indicated that through-thickness reinforcement provided increased pull-off loads and damage tolerance [20, 21]. However, stitching may slightly weaken the in-plane strength properties.
- Use the largest practical web/flange transition radius to lower the stress concentration in the bend region [22]. This radius will be dictated by the overall stiffener size and manufacturing issues.

Numerical Modeling Summary

- The VCCT-1 (one-step) method gave better predictions for strain energy release rate (G) values than both the corner and mid-side loading VCCT-2 (two-step) methods. VCCT-1 method predictions typically agreed with the MBT experimental results to within ten percent.
- The VCCT-1 method had less mesh sensitivity than both VCCT-2 methods. VCCT-1 G predictions were relatively stable down to very low (a/d_a) ratios. At an (a/d_a) ratio

of 20 there was only a 0.75 percent reduction in the prediction for G compared to the prediction at $(a/da) = 1280$.

- The VCCT-1 method was at least three times faster than the VCCT-2 methods for cracks loaded in Modes I and II. The VCCT-1 method needed only one solution to calculate G values for all modes. The VCCT-2 methods required one run to load the structure and another solution for each mode of loading.
- A point stress strength-based approach predicted damage onset to within approximately 17 % in the bend region surface ply and to within 9 % in the bend region 0^0 plies. The quadratic failure criterion was more conservative in predicting damage onset loads.
- A fracture mechanics analysis was necessary for predicting damage onset in areas with a stress singularity, such as the flange tip. Utilizing a point stress strength-based method in these areas would result in large errors for damage onset predictions.
- The fracture mechanics method for predicting initial damage at the flange tip provided good results when using an initial crack size (a_i) of less than 0.2 mm, and an (a/da) ratio of greater than 20. These parameters were used with the VCCT-1 method, 8-node quadrilateral elements, and the linear interaction criterion for crack growth.
- When the average value for G_{Ic} and G_{IIc} plus one standard deviation was used in predictive analysis, the experimental average damage load fell within the predicted range from FEA. This underscores the need for accurate material properties for use with FEA predictions.

Numerical Modeling Recommendations

- Use a standard strength-based approach to calculate damage onset in regions that do not contain stress singularities or very high stress gradients.
- Use a fracture mechanics approach to predict initial damage in areas with stress singularities such as the flange tip. Initial crack length should be kept below 0.2 mm and the ratio of crack length to crack extension (a/da) should be greater than 20 for accurate results.
- To calculate G values use the VCCT-1 method. For VCCT-1 formulas for additional element types see references [12, 13, 30].

- Use G_{Ic} values that have been experimentally determined using the modified beam theory (MBT) method rather than the Area method.
- The linear interaction criterion for crack growth (Appendix A) should be used to predict crack propagation when Mode I and Mode II loading are present.
- Always use G_{Ic} values at initiation from the starter film tip for predictions of damage onset. This ensures conservative predictions for damage loads. In addition, toughening (R-curve behavior) does not occur until significant crack growth has occurred, and may not occur at all during fatigue crack growth. Analysts should be very cautious to use G_{Ic} values greater than the initiation values in any type of crack growth analysis.
- Obtain the most accurate data for material strengths and interlaminar fracture toughness for the material system under consideration. This is essential since all predictions are ultimately based upon material properties.
- Validate the FEA results with experimental testing whenever possible.

Future Work

- Skin-stiffener specimens should be tested under fatigue loading. This is important to determine if the failure modes and locations are similar to the static cases. Fatigue loading of DCB specimens could also be performed to develop fatigue crack growth rate curves. These could be used in conjunction with FEA to establish predictive ability for delamination growth in skin-stiffeners subject to fatigue loading. Fatigue loading of DCB specimens should show whether or not the same toughening mechanisms (bridging, tow debonding, and path effects) are present during fatigue crack growth that were observed in static loading.
- Multi-axial testing of stiffeners could be investigated to better simulate the complex loading involved during wind-turbine blade operation. Stiffeners could be simultaneously loaded with a tensile stress in the skin and a pull-off load applied to the web, or any variety of combinations.
- The fracture mechanics technique that was developed to perform damage onset predictions at the flange tip should be validated on a wider variety of geometries and loading conditions. In addition, it could be applied to different structural configurations that exhibit high stress gradients (Fig. 2).
- Due to the large influence of matrix material strength on delamination resistance, tough, low-cost, RTM compatible resin systems should be researched further.

REFERENCES CITED

1. Mandell, J.F., Samborsky, D.D., "DOE/MSU Composite Material Fatigue Database: Test Methods, Materials, and Analysis," *Sandia National Laboratories Contractor Report, SAND97-3002*. December 1997.
2. Knight, N.F., Jr., Starnes, J.H., Jr., "Postbuckling Behavior of Selected Curved Stiffened Graphite-Epoxy Panels Loaded in Compression," *Proceedings of the 26th AIAA/ASME/ASCE/AHS Structures, Structural Dynamics, and Materials conference*, AIAA, New York, April 1985.
3. Martin, R.H., "Local Fracture Mechanics Analysis of Stringer Pull-off and Delamination in a Post-Buckled Compression Panel," *Applied Composite Materials*, Vol. 3, 1996, pp. 249-264.
4. Kedward, K.T., Wilson, R.S., McLean, S.K., "Flexure of simply Curved Composite Shapes," *Composites*, Vol. 20, No. 6, November 1989, pp. 527-536.
5. Hyer, M.W., Cohen, D., "Calculation of Stresses and Forces Between the Skin and Stiffener in Composite Panels," *Proceedings of the 28th AIAA/ASME/ASCE/AHS Structures, Structural Dynamics, and Materials conference*, AIAA, Washington, DC, April 1987.
6. Hyer, M.W., Cohen, D., "Calculation of Stresses and Forces Between the Skin and Stiffener in Composite Panels," *AIAA Journal*, Vol. 26, No. 7, 1988, pp. 852-858.
7. Cohen, D., Hyer, M.W., "Influence of Geometric Nonlinearities on Skin-Stiffener Interface Stresses," *29th AIAA/ASME/ASCE/AHS Structures, Structural Dynamics, and Materials Conference, Paper 88-2217*, Williamsburg, VA, April 18-20, 1988, pp. 1055-1061.
8. Minguet, P.J., O'Brien, T.K., "Analysis of Composite Skin/Stringer bond Failure Using a Strain Energy Release Rate Approach," *Proceedings of ICCM-10*, Whistler, B.C., Canada, August 1995.
9. Minguet, P.J., O'Brien, T.K., "Analysis of Test Methods for Characterizing Skin/Stringer Debonding Failures in Reinforced Composite Panels," *Proceedings of the 12th ASTM Symposium on Composite Materials: Testing and Design*, Montreal, May 1994, pp. 105-124.
10. Minguet, P.J., "Analysis of the Strength of the Interface between Frame and Skin in a Bonded Composite Fuselage Panel," *38th AIAA/ASME/ASCE/AHS/ASC Structures, Structural dynamics, and Materials Conference and Exhibit and AIAA/ASME/AHS Adaptive Structures Forum*, "Part 4 1997, pp. 2783-2790.

11. Kassapoglou, C., "Stress Determination at Skin-Stiffener Interfaces of Composite Stiffened Panels Under Generalized Loading," *Journal of Reinforced Plastics and Composites*, Vol. 13, June 1994, pp. 555-572.
12. Wang, J.T., Raju, I.S., Sleight, D.W., "Composite Skin-Stiffener Debond Analyses Using Fracture Mechanics Approach with Shell Elements," *Composites Engineering*, Vol. 5, No. 3, 1995, pp. 277-296.
13. Raju, I.S., Sistla, R., Krishnamurthy, T., "Fracture Mechanics Analyses for Skin-Stiffener Debonding," *Engineering Fracture Mechanics*, Vol. 54, No. 3, 1996, pp. 371-385.
14. Carlsson, L.A., Gillespie, J.W. Jr., "Chapter 4, Mode-II Interlaminar Fracture of Composites," *Application of Fracture Mechanics to Composite Materials*, K. Friedrich, Ed., 1989, pp. 113- 155.
15. Minguet, P.J., Fedro, M.J., O'Brien, T.K., Martin, R.H., Ilcewics, L.B., "Development of Structural Test Simulating Pressure Pillowing Effects in a Bonded Skin/Stringer/Frame Configuration," *Proceedings of the Fourth NASA/DoD Advanced Composites Technology Conference*, Salt Lake City, Utah, June 1993, pp. 863-880.
16. Scott, M.E., "Effects of Ply Drops on the Fatigue Resistance of Composite Materials and Structures," *Master's Thesis in Chemical Engineering, Montana State University-Bozeman*, August 1997.
17. Alif, N., Carlsson, L.A., Gillespie, J.W., "Mode I, Mode II, and Mixed Mode Interlaminar Fracture of Woven Fabric Carbon/Epoxy," *Composite Materials: Testing and Design, Thirteenth Volume*, ASTM STP 1242, S.J. Hooper, Ed., American Society for Testing and Materials, 1997, pp. 82-106.
18. Davies, P., Benzeggagh, M.L., "Chapter 3, Interlaminar Mode-I Fracture Testing," *Application of Fracture Mechanics to Composite Materials*, K. Friedrich, Ed., 1989, pp. 81-112.
19. Bradley, W.L., "Chapter 5, Relationship of Matrix Toughness to Interlaminar Fracture Toughness," *Application of Fracture Mechanics to Composite Materials*, K. Friedrich, Ed., 1989, pp. 159-187.
20. Freitas, G., Fusco, T., Campbell, T., Harris, J. Rosenberg, S., "Z-Fiber Technology and Products for Enhancing Composite Design," Aztex, Inc., Waltham, MA., 1996 pp. 1-8.

21. Mignery, L.A., Tan, T.M., Sun, C.T., "The Use of Stitching to Suppress Delamination in Laminated Composites," *Delamination and Debonding*, ASTM STP 876, W. S. Johnson, Ed., American Society for Testing and Materials, Philadelphia, 1985, pp. 371-385.
22. Holmberg, J.A., Berglund, L.A., "Manufacturing and Performance of RTM U-Beams," *Composites Part A*, Vol. 28A, 1997, pp. 513-521.
23. Broek, D., "Elementary Engineering Fracture Mechanics," 4th Edition, Kluwer Academic Publishers, 1986.
24. "Standard Test Method for Mode I Interlaminar Fracture Toughness of Unidirectional Fiber-Reinforced Polymer Matrix Composites, D 5528 - 94a", *1997 Annual Book of ASTM Standards*, Vol. 15.03, 1997, pp.271-279.
25. Cairns, D.S., "Static and Dynamic Mode II Strain Energy Release Rates in Toughened Thermosetting Composite Laminates," *ASTM Journal of Composites Technology and Research*, Vol. 14, No. 1, Spring 1992, pp. 37-42.
26. Russell, A.J., Street, K.N., "Moisture and Temperature Effects on the Mixed -Mode Delamination Fracture of Unidirectional Graphite/Epoxy," *Delamination and Debonding of Materials*, ASTM STP 876, W. S. Johnson, Ed., American Society for Testing and Materials, Philadelphia, 1985, pp. 349-370.
27. "Volume I, Procedures, Chapter 3 Structural Analysis, Section 3.9 Fracture Mechanics," *ANSYS User's Manual*, pp. 3-163.
28. Rybicki, E.F., Kanninen, M.F., "A Finite Element Calculation of Stress Intensity Factors by a Modified Crack Closure Integral," *Engineering Fracture Mechanics*, Vol. 9, 1977, pp. 931-938.
29. Wang, J.T., Raju, I.S., "Strain Energy Release Rate Formulae for Skin-Stiffener Debond Modeled with Plate Elements," *Engineering Fracture Mechanics*, Vol. 54, No. 2, 1996, pp. 211-228.
30. Raju, I.S., "Simple Formulas for Strain-Energy Release Rates with Higher Order and Singular Finite Elements," *NASA Contractor Report 178186*, December 1986.
31. Jerram, K., Discussion on Stress Intensity Factors for a Part-Circular Surface Flow, by F. W. Smith and M. J. Alavi, Discussion 11-62, 1st International Conference on Pressure Vessel Technology, Delft, Netherlands, 29 Sept. - 2 Oct. 1969, PVPD of ASME Discussion 11-62, p.160.

32. Hellen, T.K., Blackburn, W.S., "The Calculation of Stress Intensity Factors in Two and Three-Dimensions Using Finite Elements," *Second National Congress on Pressure Vessels and Piping*, June 23-27, 1975, San Francisco, California.
33. Konig, M., Kruger, R., Kussmaul, K., Von Alberti, M., Gadke, M., "Characterizing Static and Fatigue Interlaminar Fracture Behavior of a First Generation Graphite/Epoxy Composite," *13th Composite Materials: Testing and Design, Thirteenth Volume*, ASTM STP 1242, S.J. Hooper, Ed., American Society for Testing and Materials, 1997, pp. 60-81.
34. Reeder, J.R., Crews, J.H. Jr., "Mixed Mode Bending Method for Delamination Testing," *ALAA Journal*, 1990, pp. 1270-1276.
35. Reeder, J.R., "A Bilinear Failure Criterion for Mixed-Mode Delamination," *Composite Materials: Testing and Design (Eleventh Volume)*, ASTM STP 1206, E. T. Camponeschi, Jr., Ed., American Society for Testing and Materials, Philadelphia, 1993, pp. 303-322.
36. Hedley, C., President, Headwaters Composites Co., Personal Interviews, June 1997.
37. Agarwal, B.D., Broutman, L.J., *Analysis and Performance of Fiber Composites*, 2nd Ed., John Wiley & Sons, 1990, pp. 271-277.
38. Phillips, H.J., Sheno, R.A., "Damage Tolerance of Laminated Tee Joints in FRP Structures," *Composites Part A*, Vol. 29A, Elsevier Science Limited, 1998, pp. 465-478.
39. Hyer, M.W., *Stress Analysis of Fiber-Reinforced Composite Materials*, WCB/McGraw-Hill, 1998, pp. 387-399.
40. Martin, R.H., Jackson, W.C., "Damage Prediction in Cross-Plied Curved Composite Laminates," *Composite Materials: Fatigue and Fracture, Fourth Volume*, ASTM STP 1156, W. W. Stinchcomb and N. e. Ashbaugh, EDS., American society for Testing and Materials, Philadelphia, 1993, pp. 105-126
41. Hart-Smith, L.J., "Some Observation About Test Specimens and Structural Analysis for Fibrous Composites," *Composite Materials: Testing and Design (Ninth Volume)*, ASTM STP 1059, S. P. Garbo, Ed., American Society for Testing and Materials, Philadelphia, 1990, pp. 86-120.

APPENDIX A

Mixed-Mode Failure Calculation

Mixed-Mode Failure Calculation

1. Build the finite element model containing a crack and apply the load case to the structure. To predict delamination onset at the flange tip, the crack should be less than or equal to 0.2 mm in length, with an (a/da) ratio greater than 20.
2. Apply the VCCT-1 method at the flange tip to calculate G in Modes I and II. A diagram for the VCCT-1 method was presented in Figure 10 of Chapter 2. The equations for the 8-node quadrilateral element type were presented as Equations 5 and 6 of Chapter 2. The quantities for displacements and forces in Equations 5 and 6 are the nodal displacements and forces from the nodes as shown in Figure 10.
3. Place the calculated values for G in Modes I and II into the linear interaction criterion and calculate the ratio R .
4. Determine the fracture onset load by scaling the applied load on the FEA model in ANSYS by the square root of the inverse of the ratio R (see example problem).
5. Verify the FEA input quantities for applied load, crack length, element width, boundary conditions, etc. and interpret the results.

Example Problem

Prediction of Delamination Onset Load for Thick-Flanged Stiffener with (0/0) Interface T 5200 Series Sample with 8-node quadrilateral elements.

Experimental Data		FEA Data	
$G_{Ic} := 138.0$	G_{Ic} and G_{IIc} for (0/0) interface D155 fabric from experimental test data	$a := 0.20$	(a) is FEA crack length (mm)
$G_{IIc} := 1293.0$	G_{Ic} & G_{IIc} given in J/m^2	$P_{\text{applied}} := 113.828$	N/cm applied to ANSYS model
		$G_I := 87.2$	G in Modes I and II calculated from FEA with VCCT-1 method formulas (J/m^2)
		$G_{II} := 21.2$	

$$R := \frac{G_I}{G_{Ic}} + \frac{G_{II}}{G_{IIc}}$$

Linear mixed-mode interaction criterion, if $R \geq 1$, fracture occurs.

$$R = 0.648$$

R is the calculated ratio.

$$P_{\text{fracture}} := \left(\frac{1}{R}\right)^{.5} \cdot (P_{\text{applied}})$$

This scales the applied load by a factor to calculate the fracture onset load.

at a delam length of $a = 0.2$ mm

and P applied of $P_{\text{applied}} = 113.828$ N/cm

$$P_{\text{fracture}} = 141.37 \text{ N/cm}$$

This is the predicted fracture load
for the current configuration.

APPENDIX B

Test Results

[[0]]₁₀ DCB Samples

Sample #	Crack length (in)	Crack extension from starter film tip (in)	Crack extension from starter film tip (cm)	Area method G_{Ic} (J/m ²)	Modified Beam Theory G_{Ic} (J/m ²)
DCB 502a	1.288	0.347	0.881	315	263
502b	1.905	0.964	2.449	342	288
502c	2.368	1.427	3.625	463	349
502d	2.756	1.815	4.610	500	450
502e	3.226	2.285	5.804	505	388
502f	3.597	2.656	6.746	553	528
Average				446.3333	377.6667
Std dev				96.03263	99.94932
503b	1.618	0.724	1.839	293	326
503c	2.122	1.228	3.119	330	298
503d	2.614	1.72	4.369	411	379
Average				344.6667	334.3333
Std dev				60.35175	41.13798
DCB 504a	1.202	0.32	0.813	420	458
504b	1.615	0.733	1.862	339	398
504c	2.082	1.2	3.048	348	350
504d	2.539	1.657	4.209	348	340
Average				363.75	386.5
Std dev				37.73924	53.97222
DCB 505b	0.791	0.5305	1.347	328.7	286
505c	1.19	0.9295	2.361	365.9	286
505d	1.538	1.2775	3.245	362.5	359.9
505e	1.806	1.5455	3.926	399.5	312.5
505f	2.224	1.9635	4.987	587.9	452.3
Average				408.9	339.34
Std dev				103.1544	69.98816
DCB 506a	0.455	0.1875	0.476	274.7	384.7
506b	0.737	0.4695	1.193	469.8	405.6
506c	0.994	0.7265	1.845	565.7	524.7
506d	1.249	0.9815	2.493	521.1	520.8
Average				457.825	458.95
Std dev				128.2171	74.17944

[(+45/-45)]₁₀ DCB Samples

Sample #	Crack length (in)	Crack extension from starter tip (in)	Crack extension from starter film tip (cm)	Area method G _{1c} (J/m ²)	Modified Beam Theory G _{1c} (J/m ²)
----------	-------------------	---------------------------------------	--	---	--

[(+/-45)]₁₀

DCB 210a	0.555	0	0.000	575.941	160.1
210b	0.698	0.144	0.366	1107	656.5
210c	0.875	0.321	0.815	1440	1070
210d	1.309	0.755	1.918	1650	879.4

Average
Std dev

1193.235 **691.5**
468.3359 **392.5046**

[(+/-45)]₁₀

DCB 211a	0.575	0	0.000	293.8	202.8
211b	0.653	0.079	0.201	664.9	272.6
211c	0.724	0.15	0.381	1100	462.8
211d	0.851	0.277	0.704	1641.2	770.9
211e	1.031	0.457	1.161	1448.4	1073.8
211f	1.301	0.727	1.847	1442.4	1136.8
211g	1.645	1.071	2.720	2218.7	1051.4
211h	1.816	1.242	3.155	2069.9	998.8

Average
Std dev

1359.913 **746.2375**
657.1092 **381.2292**

Initiation from starter film

(0/0) interface

Sample #	G _{1c} (J/m ²) from MBT method	crack extension (cm)
----------	---	----------------------

511a	219.8	0
515a	129.7	0
516a	102.7	0
517a	99.1	0

mean 137.825
stdev 56.3303

(45/-45) interface

Sample #	G _{1c} (J/m ²) from MBT method	crack extension (cm)
----------	---	----------------------

303a	106	0
306a	127.2	0
403a	106	0
210a	160.1	0
211a	202.8	0

mean 140.42
stdev 41.30015

ENF test statistics

(0/0) degree interface

Sample # G_{IIC} (J/m²)

502	1170
504	1265
507	1073
508	1663

mean	1292.75
Std. Dev.	259

(+45/-45) interface

Sample # G_{IIC} (J/m²)

202	1786
203	1745
204	2343
205	2130

mean	2001
Std. Dev.	286

T Pulloff Test Summary

Specimen Type	Initial Damage Load(N/cm)*		Maximum Load(N/cm)		# samples tested
	Mean	Std. Dev.	Mean	Std. Dev.	
1 piece	85.5	15.3	132.7	3.9	11
2 piece (0.15 mm bondline)	87.7	7.6	132.3	9.2	12
Polyester/PET resin	120.3	9.1	165	6	4
Polyurethane resin	137.2	15.1	265	1	3

*Initial damage load for the Polyurethane and Polyester/PET samples was taken as the nonlinearity point on the load-displacement curve.

T Pulloff summary 2300 and 2400

Polyester/PET resin

English units				SI units		
sample #	P N.L.	Pinitial lb/in	Pmax lb/in	PNL N/cm	Pinit N/cm	Pmax N/cm
2301	69.51	69.51	89.98		121.7245	157.5713
2302	70.4	79.27	94.04		123.2831	164.6811
2303	61.35	80.52	94.41		107.4349	165.329
2304	73.6	79.912	98.35		128.8868	172.2287
mean	68.715	77.303	94.195		120.3323	164.9525
std dev	5.214649	5.220342	3.420551		9.131789	5.990004

Polyurethane samples

	P non lin lb/in	Pinitial	Pmax	P N.L.	Pinit N/cm	Pmax
2405	80	148.17	151.6		140.0945	265.4791
2406	86	151.6	151.6		150.6016	265.4791
2407	69	150.7	150.7		120.8315	263.903
mean	78.33333	150.1567	151.3		137.1759	264.9537
std dev	8.621678	1.778379	0.519615		15.09812	0.90994

T pull-off Summary

Thin-flanged stiffeners

ID#	description	English units		SI units	
		P init lb/in	P max lb/in	P init N/cm	P max N/cm
301	bonded 2 piece	52.35	72.9	91.67433	127.6611
302	0.15mm bond	59	73.37	103.3197	128.4842
303		53.04	70.15	92.88265	122.8454
304		50.46	70.51	88.3646	123.4758
505		52.78	66.84	92.42734	117.0489
1701	bonded 2 piece	47.8	84	83.70646	147.0992
1702	0.15 mm bond	51.9	83.1	90.8863	145.5231
1703		51.6	79.2	90.36094	138.6935
1704		47.6	80.2	83.35622	140.4447
1705		43.4	76.1	76.00126	133.2649
1706		45.3	75.6	79.3285	132.3893
1707		45.7	74.8	80.02898	130.9883
mean		50.0775	75.56417	87.69477	132.3265
std dev		4.312161	5.277876	7.551374	9.242516

ID#	description	English units		SI units	
		P init lb/in	P max lb/in	P init N/cm	P max N/cm
401	one piece	42.68	72.74	74.74041	127.3809
402	std layup	37.94	74.12	66.43981	129.7975
403		36.74	72.74	64.33839	127.3809
404		42.71	74.9	74.79294	131.1635
1601		56.01	76	98.08365	133.0898
1602		61.5	78	107.6976	136.5921
1603		55	76.2	96.31496	133.44
1604		58.2	75.5	101.9187	132.2142
1605		45.9	78.5	80.37921	137.4677
1606		44.2	75.5	77.4022	132.2142
1607		55.9	79.6	97.89102	139.394
				0	0
mean		48.79818	75.8	85.45445	132.7395
std dev		8.706203	2.220577	15.24614	3.888632

Average slope of the load-displacement curves is 616.38 lb/in/in or 424.958 N/cm/cm

T Pulloff Summary**Plexus Bonded T Samples**

Sample #	Bond		P non. Lin. N/cm	P max. N/cm
	Thickness cm			
1801	0.04064		93.86325	144.2972
1802	0.03302		83.21607	148.1148
1803	0.029845		85.01979	145.6807
1804	0.04699		75.47586	157.1334
805	0.059		94.75	164.2
806	0.055		83.6	150.75

T compression summary

Sample ID#	P initial Lb/in	P max lb/in	Pinitial N/cm	Pmax N/cm
2101	52.3	230.5	91.58677	403.6472
2102	54.7	231.3	95.78961	405.0482
2103	54.06	226.8	94.66885	397.1679
mean	53.68667	229.5333	94.01508	401.9544
std dev	1.242793	2.400694	2.176355	4.204051

T 5000 series statistics

ID #	Disp NL in.	P NL lb/in	slope p/delta lb/in/in	P NL N/cm
5002	0.0396	35.426	894.596	62.03801
5003	0.04586	35.718	778.8487	62.54936
5004	0.05232	37.492	716.5902	65.65599
5005	0.04181	29.799	712.7242	52.18401
5006	0.036	29.869	829.6944	52.30659
mean	0.043118	33.6608		58.94679
std dev	0.006264	3.581806		6.272459

id	crack cm	N/cm p propagation
5002	0	62.03801
5003	0	62.54936
5004	0	65.65599
5005	0	52.18401
5006	0	52.30659
5003 a	1.02108	90.01168
b	1.44526	90.01168
c	1.46304	88.29375
d	2.08661	74.56434
5004 a	1.24968	88.71579
5005 a	0.42672	107.8914
5006 a	0.24892	104.8443
b	0.55499	121.796
c	0.97663	104.8443
d	1.33477	97.21612

T 5200 results

ID #	a in.	a cm	P lb/in	P N/cm	Disp (in)	Disp (cm)	
5204a		0	0	87.17	152.6505	0.02419	0.061443
5205a		0	0	91.5	160.2331	0.02614	0.066396
5206a		0	0	82.9	145.1729	0.0232	0.058928
5205b	0.1625	0.41275	103	180.3717	0.03166	0.080416	
c	0.274	0.69596	122.16	213.9243	0.04378	0.111201	
5204b	0.296	0.75184	104.9	183.6989	0.03697	0.093904	
c	0.424	1.07696	114.7	200.8605	0.04498	0.114249	

ID #	a in.	a cm	P lb/in	P N/cm	Disp (in)	Disp (cm)	
5204a		0	0	87.17	152.6505	0.02419	0.061443
5205a		0	0	91.5	160.2331	0.02614	0.066396
5206a		0	0	82.9	145.1729	0.0232	0.058928
mean				152.6855	0.02451	0.062255	
std dev				7.53014	0.001496	0.0038	

MONTANA STATE UNIVERSITY LIBRARIES



3 1762 10277666 1